DESIGN AND OPTIMISATION OF SINGLE-LAYERED ON-METAL TAG ANTENNAS FOR ULTRA-HIGH-FREQUENCY RADIO FREQUENCY IDENTIFICATION

MUTHUKANNAN MURUGESH

DOCTOR OF PHILOSOPHY (ENGINEERING)

LEE KONG CHIAN FACULTY OF ENGINEERING AND SCIENCE
UNIVERSITI TUNKU ABDUL RAHMAN
JULY 2023

DESIGN AND OPTIMISATION OF SINGLE-LAYERED ON-METAL TAG ANTENNAS FOR ULTRA-HIGH-FREQUENCY RADIO FREQUENCY IDENTIFICATION

By

MUTHUKANNAN MURUGESH

A thesis submitted to the Department of Electrical and Electronic Engineering,
Lee Kong Chian Faculty of Engineering and Science,
Universiti Tunku Abdul Rahman,
in partial fulfillment of the requirements for the degree of
Doctor of Philosophy (Engineering)
July 2023

ABSTRACT

DESIGN AND OPTIMISATION OF SINGLE-LAYERED ON-METAL TAG ANTENNAS FOR ULTRA-HIGH-FREQUENCY RADIO FREQUENCY IDENTIFICATION

MUTHUKANNAN MURUGESH

In this thesis, four compact single-layered planar antennas are proposed for designing four novel flexible UHF RFID tags that can be used for different on-metal applications. The first two tag antennas can generate directional read patterns above the metal plate. When being placed on metal, the other two tag antennas can be read in all directions in the azimuth plane. The initial pair of antennas are compact UHF tag antennas designed for on-metal applications. Each antenna features a square ring that is loaded with two distributed inductors, which enable miniaturization of the antenna's size. The incorporation of these distributed inductors enhances the antenna's resistance, resulting in a strong conjugate impedance match with the microchip. As a result, these tag antennas can achieve a maximum read distance of 9 meters when placed on metal, using an EIRP power of 4W. The second antenna is a single-layer patch antenna with two complementarily placed C-shaped patches, designed for a metal-mountable tag with wide frequency tuning capabilities. The close coupling of the patches generates enough antenna reactance to tune the resonance frequency over a broad range from 920 MHz to 1.18 GHz without external lumped components. It achieves a maximum read distance of 9 meters on metal at 3.28W EIRP.

The third antenna is a new serpentine patch ZOR antenna used for designing an anti-metal tag with omnidirectional radiation on metallic surfaces. It features two closely stacked serpentine patches that support the zeroth-order resonance. The tag's resonance frequency can be adjusted by modifying the serpentine patch parameters. The tag is simple to manufacture with no complex structures and achieves good omnidirectional radiation. At 915 MHz with an EIRP of 4W, it has a maximum reading distance of around 10 meters on metal and provides uniform spatial coverage (> 8 meters) across the azimuth plane. The fourth antenna is a polarization-insensitive planar patch antenna designed for metal-mountable tags. It uses closely overlapped patches to create a large capacitive reactance, reducing the resonance frequency. By employing reverse-direction surface currents and orthogonal fields, the antenna becomes polarization-insensitive, and readable from almost all directions above the metal surface. It achieves a maximum read distance of 15 meters on metal with an EIRP power of 4W.

These tag prototypes are simple in structure, and they can be etched out of a piece of single-sided copper-clad polyimide film. The shorting stubs and shorting walls can be tactfully wrapped around the edges, and they do not require additional PCB fabrication processes. In these designs, different methodologies are used to provide multiple degrees of tuning freedom, and each design has a ground plane to isolate the radiator from the backing object. The transmission line and equivalent circuit models have also been derived for analysing the impedance characteristics. The proposed tag antennas have a compact size, low profile, simple structure, slight flexibility, and they can achieve better read performances than the other contemporary ones.
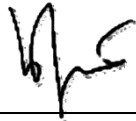
ACKNOWLEDGEMENTS

I would like to thank everyone who contributed to the successful completion of this project. I would like to express my gratitude to my research supervisors, Professor Dr. Lim Eng Hock and Associate Professor Dr. Chee Pei Song, for their invaluable advice, guidance, and their enormous patience throughout the development of the research. Additionally, I would like to especially thank Assistant Professor Dr. Lee Yong Hong, for guiding me in the experiments, which helped in this project. I would also like to express my deepest thanks to Dr. Morris Ezra, Founder & CEO of Hans Education Group, Malaysia.

APPROVAL SHEET

This thesis entitled "**DESIGN AND OPTIMISATION OF SINGLE-LAYERED ON-METAL TAG ANTENNAS FOR ULTRA-HIGH-FREQUENCY RADIO FREQUENCY IDENTIFICATION**" was prepared by MUTHUKANNAN MURUGESH and submitted as partial fulfillment of the requirements for the degree of Doctor of Philosophy (Engineering) at Universiti Tunku Abdul Rahman.

Approved by:

_____

(Prof. Dr. LIM ENG HOCK)
Date: 21 July 2023
Professor/Supervisor
Department of Electrical & Electronic Engineering
Lee Kong Chian Faculty of Engineering & Science
Universiti Tunku Abdul Rahman

_____

(Dr. CHEE PEI SONG)
Date: 21 July 2023
Associate Professor/Co-supervisor
Department of Mechatronics & Biomedical Engineering
Lee Kong Chian Faculty of Engineering & Science
Universiti Tunku Abdul Rahman

LEE KONG CHIAN FACULTY OF ENGINEERING AND SCIENCE
UNIVERSITI TUNKU ABDUL RAHMAN

Date: 21 July 2023

SUBMISSION OF THESIS

It is hereby certified that **MUTHUKANNAN MURUGESH** (ID No: **20UED00789**) has completed this thesis entitled "**DESIGN AND OPTIMISATION OF SINGLE-LAYERED ON-METAL TAG ANTENNAS FOR ULTRA-HIGH-FREQUENCY RADIO FREQUENCY IDENTIFICATION**" under the supervision of Professor Dr. Lim Eng Hock (Supervisor) from the Department of Electrical and Electronic Engineering, Lee Kong Chian Faculty of Engineering and Science (FES), and Associate Professor Dr. Chee Pei Song (Co-Supervisor) from the Department of Mechatronics & Biomedical Engineering, Lee Kong Chian Faculty of Engineering and Science (FES).

I understand that University will upload softcopy of my thesis in pdf format into UTAR Institutional Repository, which may be made accessible to UTAR community and public.

Yours truly,

(MUTHUKANNAN MURUGESH)

DECLARATION

I hereby declare that the thesis is based on my original work except for quotations and citations which have been duly acknowledged. I also declare that it has not been previously or concurrently submitted for any other degree at UTAR or other institutions.

_____

(MUTHUKANNAN MURUGESH)

Date: 21 July 2023

TABLE OF CONTENTS

3 COMPACT RING ANTENNAS WITH HIGH-IMPEDANCE LINE LOADED WITH DISTRIBUTED INDUCTORS

LIST OF TABLES

LIST OF FIGURES

CHAPTER 1

INTRODUCTION

1.1   Introduction to RFID

Radio frequency identification (RFID) technology has been around for decades and becoming more popular after it was used successfully for automatic identification (Auto-ID). Figure 1.1 shows the different ways that Auto-ID can be implemented, such as with optical character recognition (OCR), voice identification, biometrics, barcodes, and RFID (Tan and Ismail, 2012). Even though barcode technology has been around for more than 50 years, the RFID technology is slowly replacing it for certain applications. The RFID technology has many advantages over the barcode technology that make it stand out. For example, it can be read from a much considerably long distance quickly, and it doesn't need a clear line of sight to work (Finkenzeller and Muller Dorte, 2012). Table 1.1 shows how these two technologies stack up against each other. The RFID technology can also be better than other Auto-ID technologies for some applications because it can handle multiple tags simultaneously and send and receive data quickly. Also, this technology makes it possible to access the data of tagged objects from a distance in real time using the radio frequency communication method. This takes Auto-ID to the next level. With all of the above benefits, the Auto-ID industry will likely continue to use RFID technology in the coming years. In addition, the RFID technology has already been widely used in the real applications such like contactless identification, remote access, tracking inventory, and managing assets.
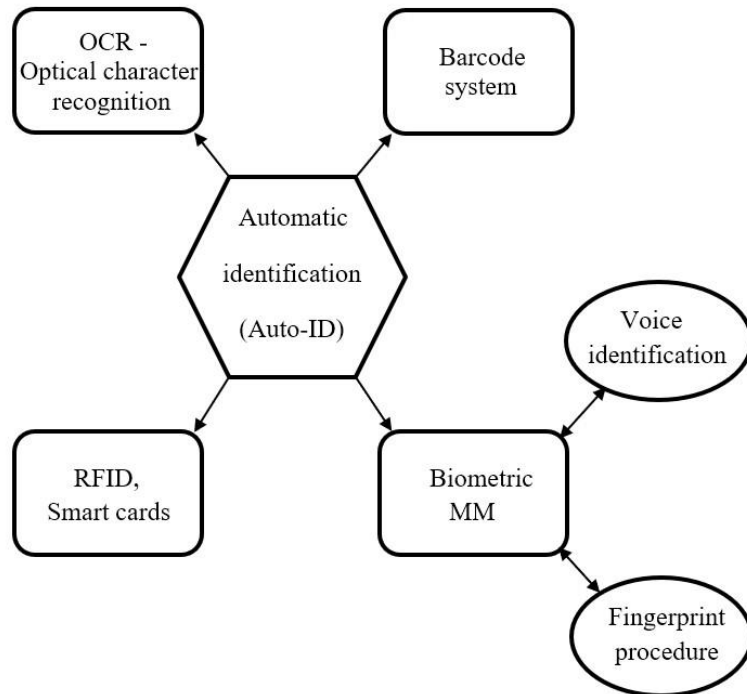
Figure 1.1. Auto-ID systems.

Table 1.1. Advantages of RFID technology as compared to barcodes.

	RFID	Barcode
Line-of-sight requirement	No	Yes
High storage capacity	Yes	No
Proper orientation requirement	No	Yes
Read / write function	Yes	No
Parallel identification	Yes	No
Recognition of objects, people, and animals	Yes	Items only

1.2   Operating Principle of RFID System

As seen in Figure 1.2, a simple RFID system consists of three core components: a host, an interrogator, and a transponder (Hunt et al., 2007). Through radio waves, the interrogator, comprising a reader and a reader antenna, communicates with the transponder (tag). The RFID system's operational principle is now described. When a tag reaches an interrogator's interrogation zone, the interrogator directs the tag to communicate the information stored in its microchip, which is activated by the power received

by the tag antenna. Finally, the data is sent from the interrogator to the host (a computer or workstation) via a network interface for data processing, monitoring, and change.
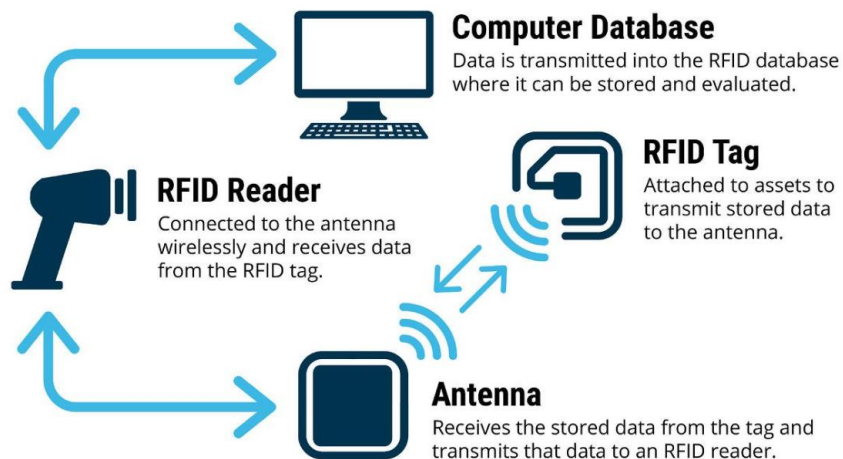
Figure 1.2. Typical RFID system.

1.3   RFID Tag Types and RFID Frequency Spectrum

RFID tags are classified into three types: passive tags, semi-passive tags, and active tags. The details for each category of the tag are now detailed more below:

(1) ***Passive tags.*** The microchip and the antenna are the only significant components of an passive tag. It is not equipped with a battery. As a result, the energy obtained from the interrogator is used to power up the chip. The extra energy is then used to communicate with the interrogator. Since some energy is used to activate the chip, the read range of the passive tag is less than those of the active and semi-passive tags. When compared to the active and semi-passive tags, the advantages of the passive tag include lower manufacturing costs, smaller size, and longer lifespan.

3

(2) *Semi-passive tags.* A semi-passive tag is the amalgamation of a passive and an active tag. Despite having a battery, the semi-passive tag, unlike the active tag, will only work when it receives a signal from the interrogator. However, only a fraction of the power generated by the interrogator is used to interrogate the chip. The battery also powers up other circuitries, such as the sensor and the chip. The majority of the gathered power is returned to the interrogator later. As a result, the semi-passive tag has a significantly greater read distance than the passive tag. Furthermore, the semi-passive tag has a longer lifespan than the active one.

(3) *Active tags.* The active tags, as opposed to those passive tags, include a battery, which increases the tags' read range and storage capacity. The active tag is also known as a beacon since signals are sent from the tag regularly without the need for interrogator power. Because the tag is powered by a battery, it can function for about 3 - 7 years, which is the lifespan of a battery. An active tag is more expensive and larger in size than the passive tag.

As illustrated in Figure 1.3, the RFID systems can operate in various frequency bands that vary depending on the tag's properties and the intended applications. The regulated low-frequency (LF, 120-140 kHz), high-frequency (HF, 13.56 MHz), and ultra-high-frequency (UHF, 860-960 MHz) frequency bands are extensively utilized (Chen and Hsu, 2013). The LF band is located in the lower half of the spectrum. This was the first frequency band employed in RFID applications, and it continues to have a large market, particularly in

4

animal tracking and identification. Meanwhile, the HF band is a frequently used frequency band in near-field applications such as contactless payments, access control, and smart card authentication.
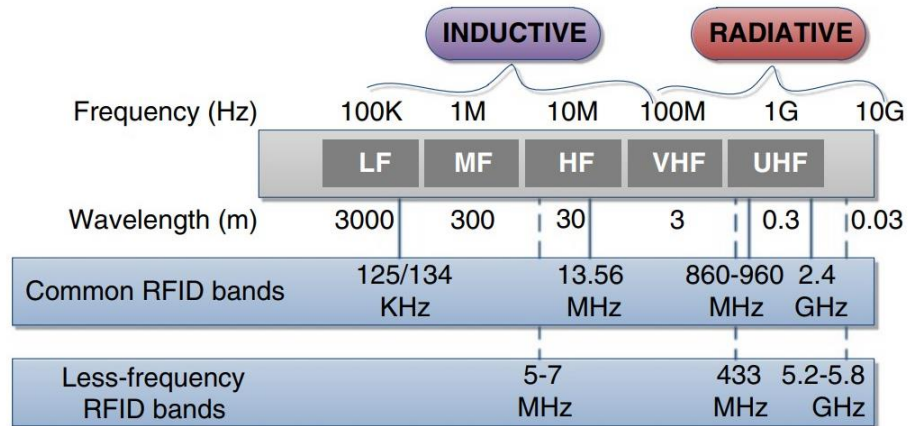
Figure 1.3. Regulated RFID frequency bands.

1.4   Problem Statements

The UHF RFID tags are frequently facing many practical challenges such as radiation performance, antenna size and fabrication costs. A practical tag must be ideally compact in size with single-layered structure, high in gain, long in read distance, insensitive in attaching platform, and low in fabrication costs. Most of the UHF RFID tags are frequently made using a dipole antenna. However, when this antenna is placed in close proximity to a metallic object, its image currents can dramatically reduce the radiation efficiency. As a result, most of the commercial metal tags have a read distance of less than 3 m.

Furthermore, the length of a dipole antenna must be designed to be half its working wavelength, which is too long for the practical UHF tagging applications. Several typical methods that can be used for reducing the tag

sizes have been proposed, including meandering the radiating arms (Shi et al., 2015), employing a high dielectric constant material (Babar et al., 2012), and adding slots (Reed et al., 2001), slits, or notches (Chen et al., 2012) into the radiators. However, as the tag antenna's size is reduced, its radiation efficiency also decreases.

Microstrip patch antennas are commonly used for designing many on-metal tags. In some cases, the broad ground plane and lack of flexibility of this type of antenna could make it unsuitable. The patch antennas can be reduced in size by including shorting pins and vias on a printed circuit board (Chen and Tsao, 2010a; Zhang and Long, 2013b). However, these vias may not be cost-effective for commercial tag applications because they necessitate additional printed circuit board (PCB) operations during fabrication. And because the characteristics of such an antenna typically depend on the location of the shorting vias, optimizing it can be lengthy and tedious (Lin et al., 2013). Impedance matching is an important factor in antenna design to maximize power transfer. However, the RFID tag design usually prohibits the use of external lumped elements to improve the impedance matching level due to fabrication costs and structural complexity. Consequently, it is essential that the antenna impedance can be adjusted to conjugate match with the chip impedance. Several matching techniques, including the use of modified T-match networks, are widely utilized in RFID tag design (Marrocco, 2008; Zamora et al., 2013).

1.5   Aim and Objectives

1.   To research and develop electrically small (with all dimensions smaller than λ/π) slightly flexible single-layered planar antennas which can have a read distance of beyond 9 m when mounted on metallic surfaces.

2.   To explore new ways for miniaturizing RFID tag antennas while maintaining their performances.

3.   To incorporate new impedance tuning mechanism into the RFID tag antennas so that conjugate match can be easily obtained.

4.   To explore new antenna configurations that can generate directional or omnidirectional radiation patterns, which may be useful for certain on-metal applications.

1.6   Contribution of the Study

My research contributions are discussed in this section. This thesis presents a comprehensive theoretical and experimental analysis on the metal-mountable passive UHF RFID tags. The important findings of this thesis are given below:

1.   Two compact UHF tag antennas, which consist of a square ring loaded with two distributed inductors, are proposed for on-metal applications. Miniaturization of the antenna footprint is realized by incorporating two distributed inductors. It will be shown that the required inductances are much dependent on their locations on the

ring resonator due to the variation of the current intensity. Due to the high-inductive nature of the distributed inductor, the antenna resistance of the ring resonator can be significantly enhanced so that it can achieve a conjugate impedance match with the microchip.

2. A single-layer patch antenna, which is constructed using two complementarily placed C-shaped patches, has been proposed for designing a metal-mountable tag with a wide-range of frequency tuning capabilities. The two patches are closely coupled to generate sufficient antenna reactance, which is, in turn, employed as a tuning mechanism. With only the employment of this tuning mechanism, the tag's resonance frequency can be successfully tuned over a broad range covering 920 MHz - 1.18 GHz without using any other external lumped components, shorting stubs, or vias.

3. A new serpentine patch antenna is used for designing an anti-metal tag with omnidirectional radiation characteristics on metallic surfaces. The zeroth-order resonance (ZOR) structure here comprises two closely stacked serpentine patches for providing the parasitic elements required for supporting the zeroth-order resonance. Also, the geometrical parameters of the serpentine patches can be used for effectively tuning the tag resonance frequency. The proposed tag contains no complex structures like metallic vias, small notches, and narrow slots.

4.   A polarization-insensitive planar patch antenna with a large embedded serial capacitance is proposed for constructing a metal-mountable tag by using merely a single radiator. The proposed antenna structure contains two flaps of patches, which are very closely overlapped, for generating a large capacitive reactance for reducing the resonance frequency of the tag. It has been found that the surface currents in the overlapped region are in the reverse direction as the large capacitance is virtually placed in series. This feature has been tactfully employed for producing a pair of orthogonal currents for designing the polarization-insensitive tag antenna. It can generate orthogonal fields uniquely, making it readable from almost all directions at all points above the metal surface.

1.7 Thesis Overview

This thesis is divided into seven chapters. The first chapter discusses the fundamentals of the conventional RFID systems. The RFID technology's advantages and disadvantages are compared with the other common Auto-ID technologies, such as barcode technology. The corresponding working mechanism and the limits of each frequency bands are briefly described. The current trends of the UHF RFID systems are highlighted. The specific problems and technical concerns for constructing tag antennas are also reviewed.

In chapter 2, some of the contemporary on-metal tags are analysed. The feasibility of designing UHF RFID tags using different antenna structures is explored. This chapter has also covered several miniaturizing methods. Furthermore, different types of radiation patterns, design methodologies, and matching techniques are introduced in the same chapter.

Chapters 3 – 6 discuss the design and characterization of electrically small RFID tag antennas. Each chapter provides technical analysis of the tag antenna design as well as the corresponding transmission line model or equivalent circuit model that can be used for analysing its impedance characteristics. Simulations and experiments have been employed to characterize the tag's performance.

In the last chapter, the significant features of each antenna are highlighted, and the research works are summarized.

CHAPTER 2

LITERATURE REVIEW

2.1   On-Metal UHF RFID Tag Antenna

Nowadays, the usage of UHF RFID technology is increasing rapidly across a wide range of industry sectors due to the technology's ability to automate tracking and identification. However, identifying metallic objects remains a big challenge for a RFID tag antenna since metallic items in close proximity can significantly impact the tag antenna's input impedance and radiation properties (Ghiotto et al., 2008). Different types of antenna structures that can be used for on-metal tag design are introduced in this section.

2.1.1   Dipole Antenna

Dipole antennas are commonly used for constructing RFID tags since they have the simplest form, consisting of two identical conducting arms. The total length of the two conducting arms must be half of the operational wavelength for a half-wavelength center-fed dipole, as shown in Figure 2.1. According to Figure 2.1, the paper dipole is designed to resonate at 915 MHz, which is falling in the US band where most UHF RFID systems operate. It requires a dipole length of 164 mm, which is too long for UHF tagging applications. To minimize antenna size even further, the dipole arms can be folded (Genovesi and Monorchio, 2010), meandered (Marrocco, 2003), or wrapped into a spiral shape (Cho et al., 2008). Packing wires closely, on the other hand, can cause

the antenna to become more reactive (Hansen, 2006), introducing current crowding effect (Shen et al., 2011). It can reduce radiation efficiency and bandwidth.
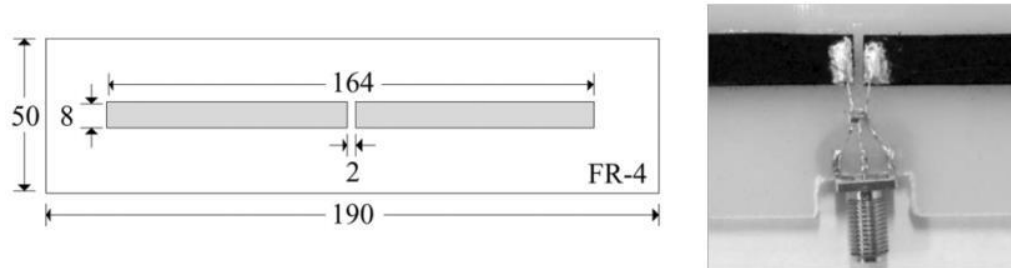
Figure 2.1.   A conductive paper-based center-fed half-wavelength dipole.

Image currents can lower the antenna impedance and radiation efficiency (Ukkonen et al., 2005). (Koo et al., 2011) Moving a dipole closer to a metallic plate can reduce its read distance from 7.32 m to 3.01 m. Inserting a foam or ceramic spacer (Koo et al., 2011) between the dipolar tag and the metallic object can reduce the effects. However, ceramics require high-temperature heat curing. Figures 2.2 and 2.3 illustrate the electromagnetic isolation methods for tag design using the electromagnetic band gap (EBG) structures (Gao and Yuen, 2011) and artificial magnetic conductors (AMC) (Kim and Yeo, 2008), but these methods can complicate the tag design processes.
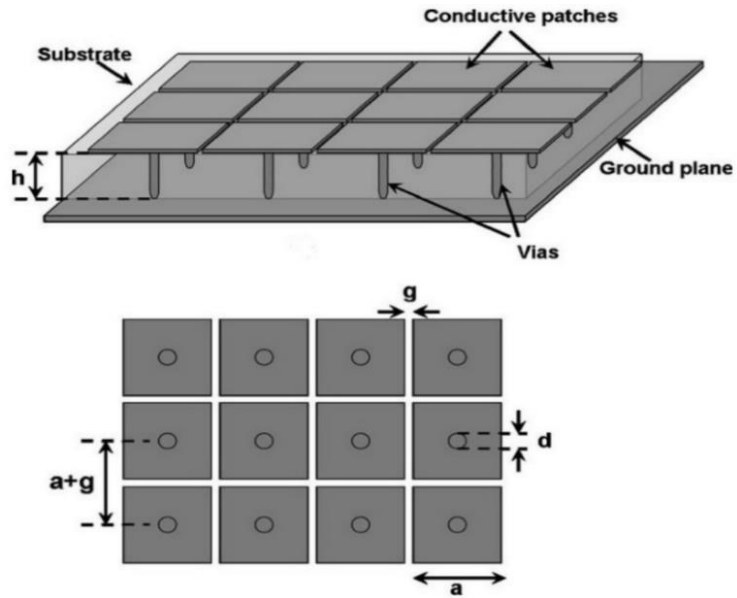
Figure 2.2. Cross-sectional view and top-down view of the EBG structure.
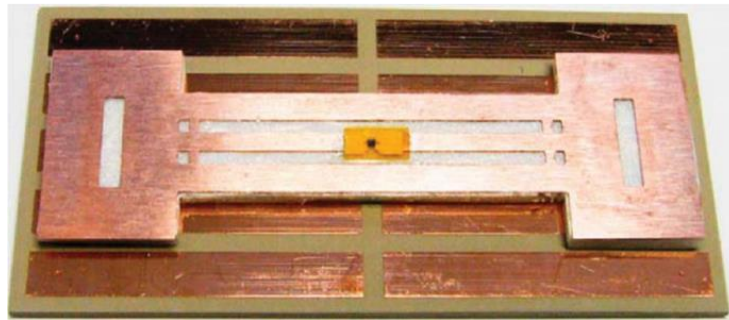
Figure 2.3. A modified dipole antenna mounted on an AMC ground plane.

2.1.2 Microstrip Patch and Slot Antenna

On-metal tags have also been designed using a microstrip patch antenna with a ground plane underneath. This is due to the ground plane's ability to isolate the radiator from the backing metal electromagnetically. Figure 2.4 (Mo and Qin, 2010) depicts a microstrip patch design consisting of a radiating patch and an open-stub feedline laminated on top of a grounded dielectric substrate. Furthermore, the tag in (Lin et al., 2016) was created with a 120 mm × 60 mm radiating plate with a Z-shaped slot etched at the center of the plate, as shown in Figure 2.5. The slot, which has a total length of about half a guided

13

wavelength, acts as an exciter for the radiating plate. Lifting the radiating plate, a certain distance above the metallic plane increases the tag's realized gain as the reflection from the metallic plane increases. Another slot-type tag may be found in (Ryoo et al., 2012), which has a slot radiator activated by a simple loop. Patch-type and slot-type tags can achieve good read performances with simple structures. However, they are inflexible and typically huge in size, making them unsuitable for small metallic objects.
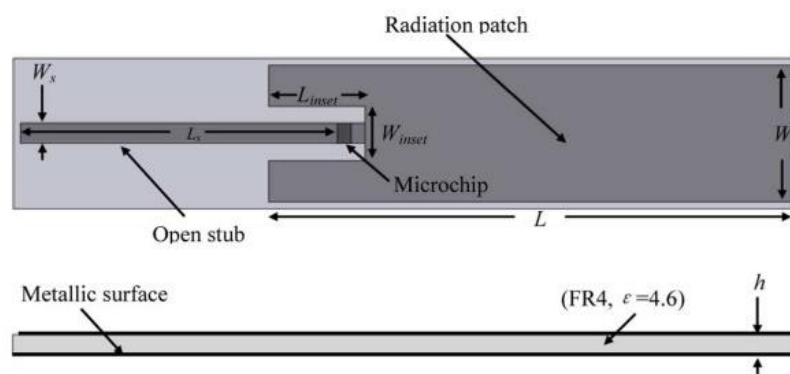
Figure 2.4. A top and side view of a patch-type tag antenna.
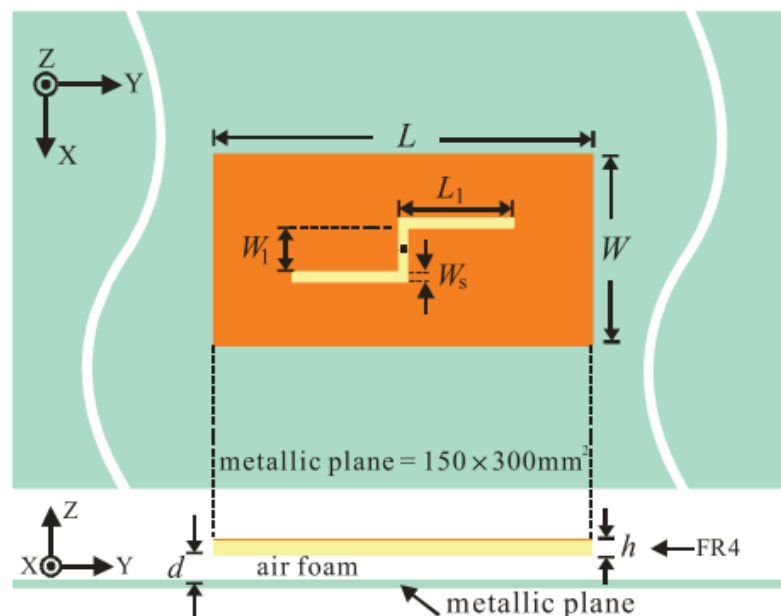
Figure 2.5. A top and side view of a patch-type slot antenna.

2.1.3 Planar Inverted Antenna

Half-wavelength patch antennas, like dipoles, suffer from size constraint. The antenna size, however, can be lowered by connecting one edge of the patch radiator to the ground plane through inductive vias or shorting stubs, resulting in a planar inverted structure, as shown in Figures 2.6 (Hassan et al., 2009) and 2.7 (Ooi et al., 2022). These planar inverted structures such as planar inverted-L antenna (PILA), and planar inverted-F antenna (PIFA), which are also the modified forms of the monopole, resonate at a quarter-wavelength, allowing them to achieve high compactness. Furthermore, they can offer wide bandwidth, a low profile, and high gain, making them an excellent choice for designing the UHF RFID tag antennas. Nonetheless, shrinking the radiating patch from half-wavelength to quarter-wavelength has a negative impact on its radiation performance. According to (Yang et al., 2011), a single-patch tag antenna's achievable read distance was only half of that of the double-patch tag antenna. Furthermore, decreasing the profile of these planar inverted structures can often compromise their radiation effectiveness (Zhang and Long, 2013a). Some planar inverted antennas may require a thickness of greater than 3 mm in order to work effectively, and such a large profile may be an issue for certain RFID applications (Michel et al., 2018). In addition, the ground plane that makes these planar inverted structures insensitive to the backing metallic objects, similar to the patch antenna, might also be excessively large.
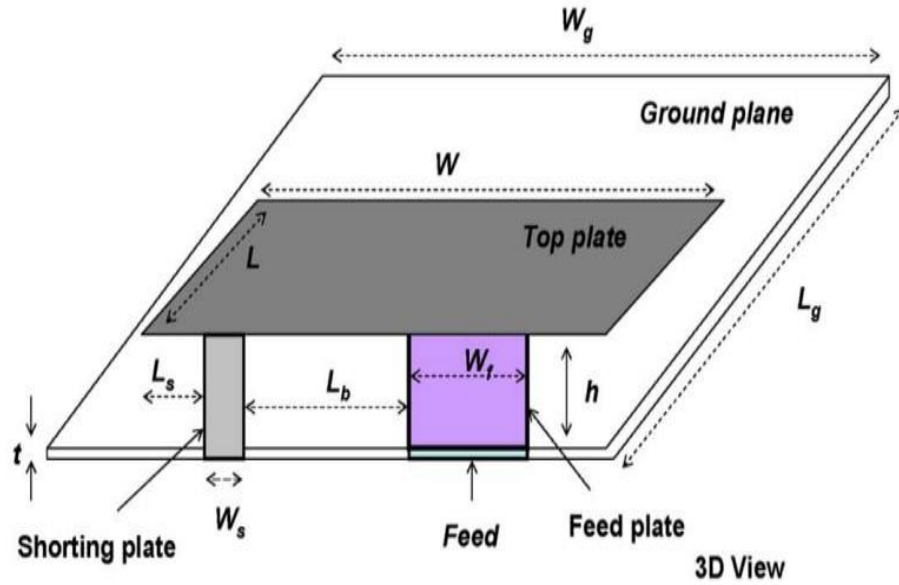
Figure 2.6. Planar Inverted-F antenna.
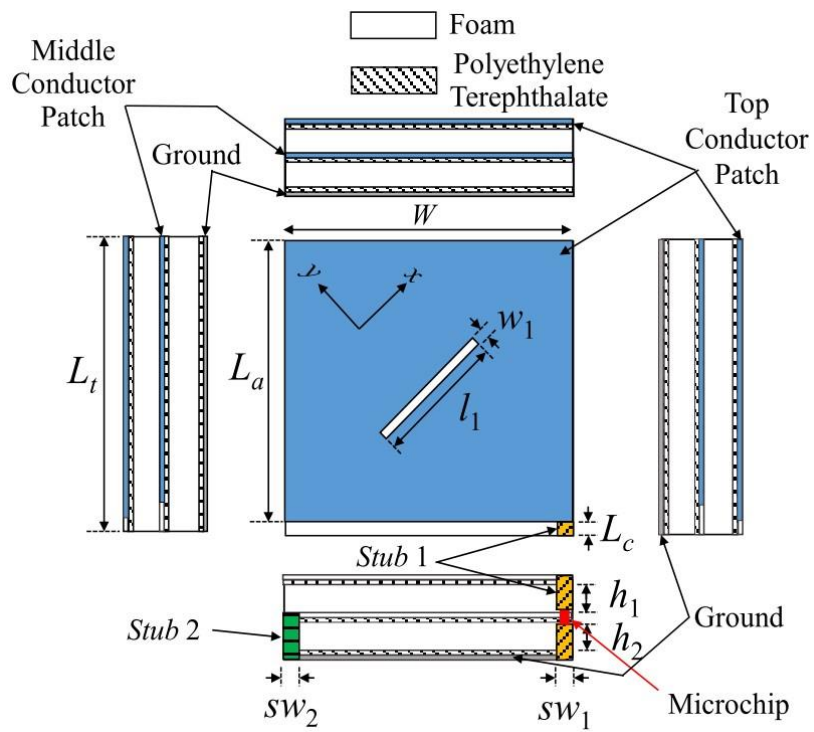
Figure 2.7. Planar Inverted-L antenna.

2.1.4 Ring Antenna
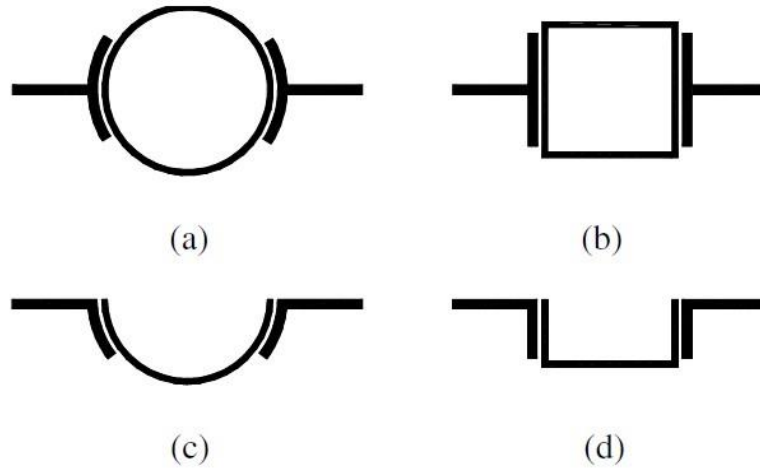
Figure 2.8. Layouts of the (a) annular ring, (b) square ring, (c) open-loop ring with curvature effect, and (d) U-shaped open-loop ring resonators.

Ring antennas can be made into any shape such as annular, square, triangular, etc., as shown in Figure 2.8. The first microstrip annular ring was proposed in (Bergman and Schultz, 1955). Recently, the ring resonator, which is simple in geometrical shape, has been explored for designing different antennas and microwave circuits (Hsieh and Chang, 2005). The resonance modes of a closed ring are usually in the multiple of its operating wavelength. A ring resonator that works in the fundamental mode, where the circumference is approximately one guided wavelength, is simply too large to be useful for the UHF RFID (860 – 960 MHz) tag design. Over the past years, several design techniques have been applied to miniaturize the ring size and optimize the tag performance. It was shown (Okano, 2006) that the aperture shape inside a ring resonator could be modified to broaden the bandwidth of a tag antenna with a 50 Ω port. This antenna, however, can never be used in practice as the RFID chip impedance is always complex. Multiple lumped (Taylor and

Batchelor, 2019) and distributed (Liu et al., 2013) capacitors were integrated with a ring resonator for miniaturing the tag footprint and achieving a conjugate impedance match with the chip, as shown in Figure 2.9. A ring meandered in many folds (Chen et al., 2016) for designing a compact circularly polarized tag antenna (58.6 mm $\times$ 58.6 mm) that was able to reach a very far read range (~ 20 m). However, the above-mentioned tag antennas can't be used on metal surfaces as the induced image currents can cause the radiation performances to deteriorate significantly. To solve this problem, a meandered-loop tag antenna, shown in Figure 2.10 (Koo et al., 2011), was elevated up to 10 mm from the metal surface to mitigate the impact of the metal surface, with the price of increasing the antenna profile. In this case, multiple folded dipoles have been employed to increase the antenna gain, resulting in a large footprint (91 mm $\times$ 27 mm). A gain degradation of ~ 10 dB was also observed when the ring antenna came near (1 mm) to metal. A recent work (Borchardt, 2020) has proposed to erect the ring resonator in vertical with respect to the metal surface for designing a metal-mountable tag antenna. However, this antenna profile is simply too high (~16.5 mm), making it not suitable for tagging applications.
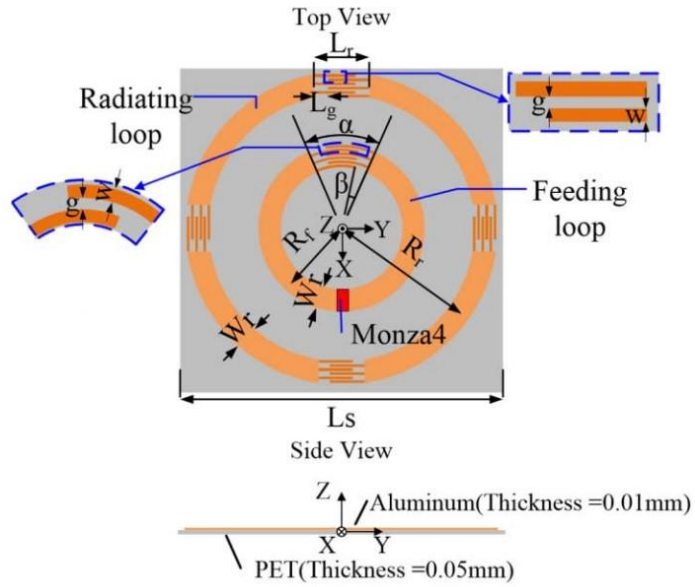
Figure 2.9. Capacitively loaded, inductively coupled fed loop antenna.
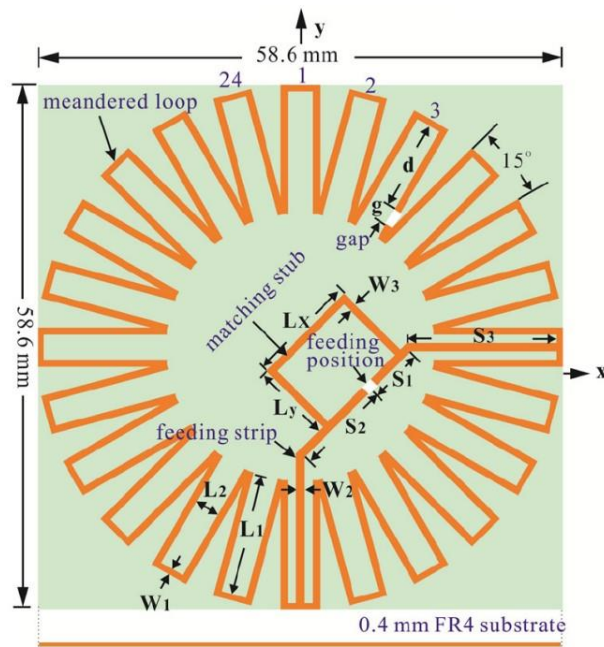
Figure 2.10. Compact circularly polarized meandered-loop antenna.

2.1.5 Polarization-Insensitive Antenna

The demand for planar polarization-insensitive UHF tags has been growing as radiators can provide readability in all polarizations. Combining multiple single-polarized resonators is a possible way to design an antenna that can read all polarizations. As indicated in Figure 2.11(a) of (Yang and Son, 2016),

two dual-planar inverted-F antennas are placed in the cross arrangement and fed through two balanced ports to provide polarization insensitivity in all directions. However, the tag antenna is large (64 mm × 64 mm), and it requires the use of four lumped capacitors and 12 vias. This can also introduce uncertainty as some antennas are very sensitive to the locations of vias. Despite the fact that four-chip capacitors are included in the antenna construction to improve impedance matching, the maximum power transfer achieved at the tag's resonance is just 59%. As depicted in Figure 2.11(b), a polarization-insensitive UHF tag antenna that can be mounted on a metal surface has been proposed (Bong et al., 2018), where two dipolar patches are positioned orthogonally for designing a tag that can be detected in all directions in the upper space ($\theta \leq 90^{\circ}$). The blind spots of either dipole have been effectively removed by combining the fields generated by the other. Although the tag antenna has a compact footprint, its impedance is poorly matched to the chip, limiting its detection range to not more than 3.5 meters. This is because no tuning mechanisms are incorporated into the tag's design. However, the reported tags in (Yang and Son, 2016) and (Bong et al., 2018), both of which have employed two pairs of radiators, have a short read range (less than 3.5 m), and they require a four-port microchip (Monza 4D).
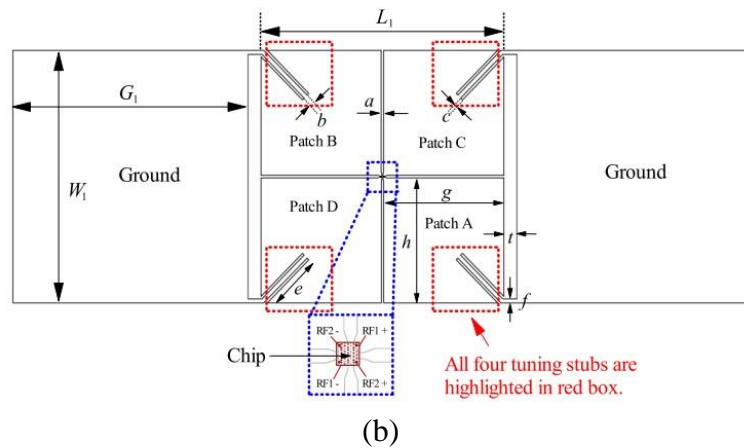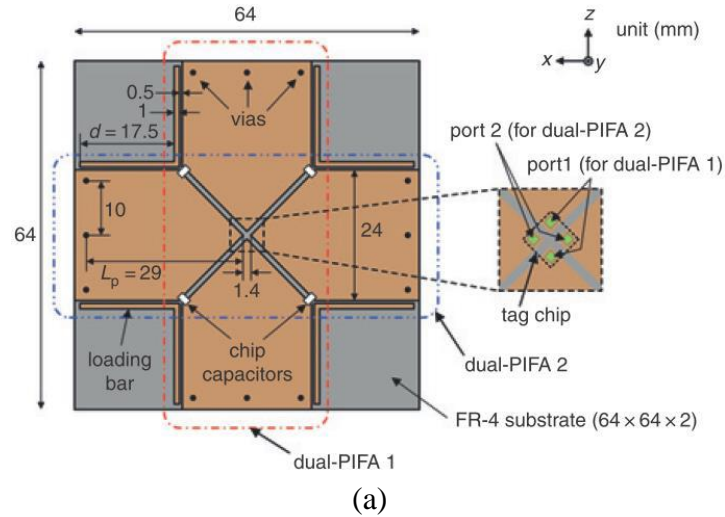
Figure 2.11. Polarization diversity tag antennas designed using (a) Planar inverted-F antenna and (b) folded-patch antenna.

2.1.6 ZOR antenna

In recent years, the zeroth order resonance (ZOR) mode antennas have been explored for constructing low-profile omnidirectional tags. A patch resonator with loading slits (Li et al., 2020), open stubs (Park and Lee, 2011), shorted ring (Yoo and Kahng, 2012), circular microstrip (Zhang et al., 2018), and loading slots (Pyo et al., 2009) can be used to design linearly and circularly polarized ZOR antennas. The input impedance of the ZOR antennas is usually 50 Ω, but the impedance of the RFID chips is always a complex number. As a result, the ZOR structures can't be directly used for RFID applications. In the

zeroth-order mode, the operating frequency of an antenna is regardless of its physical dimension, allowing it to be shaped into any size without affecting the radiating characteristics. The composite right/left-handed transmission line (CRLH-TL) characteristics can be carefully adjusted to obtain the ZOR resonance, and the antenna size can be easily reduced because of this feature. Designing a UHF RFID tag antenna can be done by cascading several ZOR elements, such as the magnetic loop antenna in (Lee and Lee, 2007) and the mushroom structures in Figure 2.12(a) (Lai et al., 2007) and Figure 2.12(b) (Park et al., 2007), but this can substantially increase the structural complexity and manufacturing costs. As shown in Figure 2.13, a low-profile cap-shaped zeroth order resonance patch antenna has been proposed for metal mountable UHF RFID applications (Ooi et al., 2023). Here, the tag read distance is high, but the inductive stubs are very sensitive to the tag resonance frequency, which will make the prototyping process more complicated.

(a)   (b)
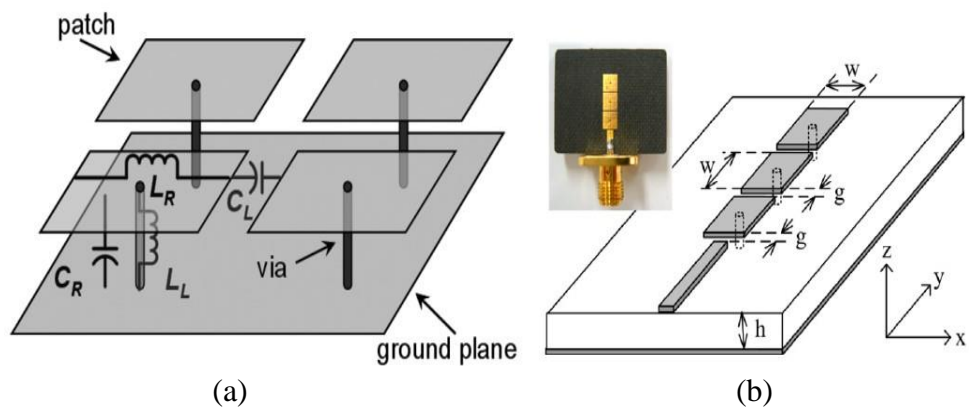
Figure 2.12.   (a) Infinite wavelength ZOR structure and (b) Epsilon negative ZOR antenna.
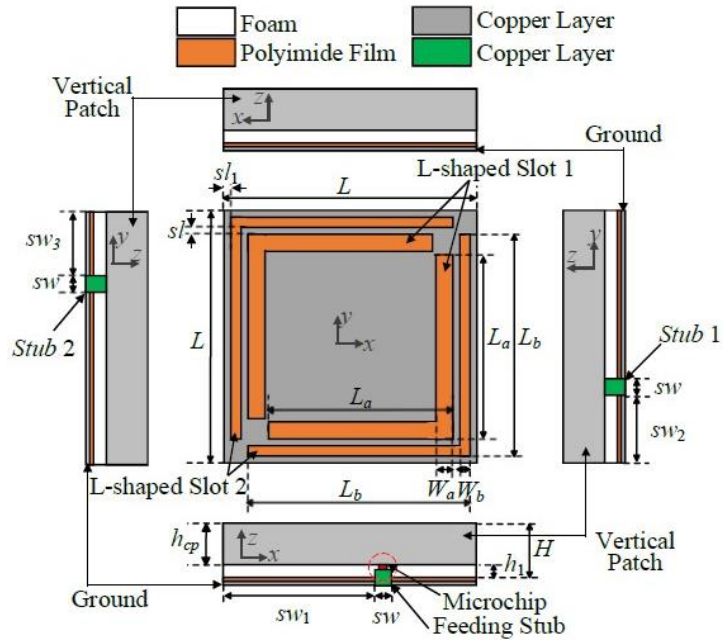
Figure 2.13. Slot-loaded cap-shaped patch ZOR antenna.

2.2 RFID Tag Antenna Design Methodology

2.2.1 UHF RFID Tag Design Requirements

When designing a passive UHF RFID tag, the following requirements must be taken into consideration.

1) **Power and regulated frequency:** Each country has its own UHF RFID regulations. The North and South America's regulated UHF bands are falling within 902-928 MHz; European's band is 865-868 MHz; while some Asian countries are using 920-926 MHz (Rao et al., 2005a). In most of the RFID systems, the permitted power level is 4 W EIRP (or 2 W ERP). As a result, it is critical to ensure that the proposed tags meet the regulatory requirements in the targeted regions.

23

2) **Read distance and tag size:** RFID tags should be small and compact in order to be used in applications with limited tagging space. Electrically small RFID tags, on the other hand, are associated with poor read distance and low radiation efficiency (Shahpari and Thiel, 2018). As a result, tags must be optimized to maximize their read distances, while remaining compact.

3) **RFID tag applications:** The electrical characteristics and surface curvatures of the tagged objects can have an effect on the radiation characteristics of the tag (Ghiotto et al., 2008). Therefore, it is necessary to understand the RFID tag's application prior to selecting the appropriate antenna type.

4) **Matching technique:** Additional lumped components are not permitted in antenna design due to cost constraints. As a result, the matching technique should be integrated directly into the antenna structure itself to improve power transfer.

5) **Manufacturing costs:** One of the reasons why the RFID industry is continuously growing is the possibility to make the systems/tags low in cost. It is quite common that costing is to become an important factor in the selection of substrates and materials for tag design. For example, despite having lesser electrical conductivity than copper, aluminum is nevertheless extensively utilized in commercial RFID tags due to its low cost. Tags with ceramic-based substrates are usually expensive and

difficult to manufacture. As a result, they are only applied for some specific applications.

2.2.2 UHF RFID Tag Design Processes

A flowchart has been given to describe the tag design processes for the four metal-mountable UHF RFID tags in Figure 2.14. Following is a detailed description of each of the stages:

Stage 1: Finding out the intended application

Before designing a UHF RFID tag, it is important to determine what object it will be attached. The UHF tag's efficiency will also be greatly influenced by the surrounding metals, resulting in a much shorter detectable range. It is to ensure that the proposed tag can function well in the specified environment.

Stage 2: Finding out the design criteria

The design criteria are figured out then. It includes the determination of the tag's footprint and profile. Other design criteria, such as the requirements of read performance and costs of materials, are also important to be considered.

Stage 3: Choosing a suitable antenna structure

Next, an appropriate antenna structure is selected to meet the design criteria. Some of the possible antenna structures for metal-mountable tags were also discussed in Section 2.1. The properties and performances of the chosen antenna must be carefully analysed before commencing the design. Designing a tag also requires careful selection of dielectric substrates and conductive materials, which can affect tag performance significantly.

Stage 4: Building and optimizing the simulation model

After deciding on a suitable antenna structure, the CST Studio Suite software is used to build a simulation model of the UHF tag antenna and its supporting object. Also, the same software is used for all the simulations and optimizations. During the simulations, it might be necessary to include the effects of the environment to tell how well the tag works. This can also make sure that the results are accurate.

Stage 5: Making a prototype and carrying out measurements

After optimization, the UHF tag prototypes are made for assessment. The Voyantic Tagformance Pro Measurement System is employed for performing all the measurements in a RFID measurement chamber (anechoic cabinet). It is to ensure that the measured outcomes match well with the simulated ones. Otherwise, investigations are to be conducted to fix the discrepancy. If the measured and simulated results can agree well, the design

26

process is completed, and the UHF tag can be used for the selected application.
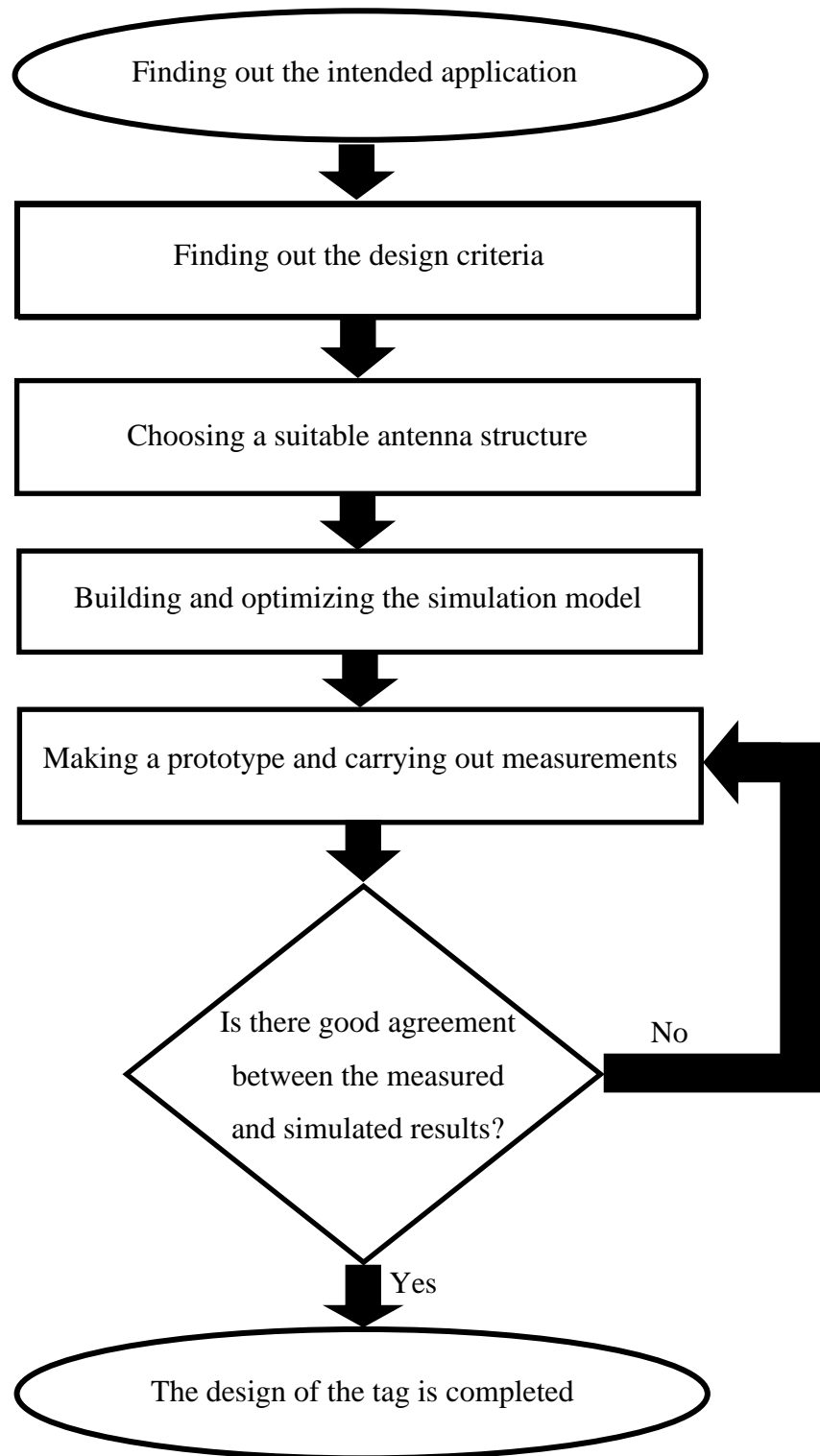
Figure 2.14. A UHF RFID tag antenna design procedure.

2.3   UHF RFID Tag Measurement Methods

2.3.1   Polarization Measurement

For the broadside metal-mountable tag antennas, their main beams are pointing to the normal direction ($\theta = 0°$). As a result, the polarization angle (ϕ_p) of each directional tag antenna can be found by placing the reader antenna right above the tag (z-direction), while allowing the tag to rotate around its own z-axis, as shown in Figure 2.15. The measured curve can tell how good the polarization characteristic in a certain direction is. On the other hand, an omnidirectional tag antenna does not need polarization measurement in the boresight. This is due to the fact that it can only generate vertically polarized electric fields (perpendicular to the platform) and radiate effectively in all directions perpendicular to the z-axis.
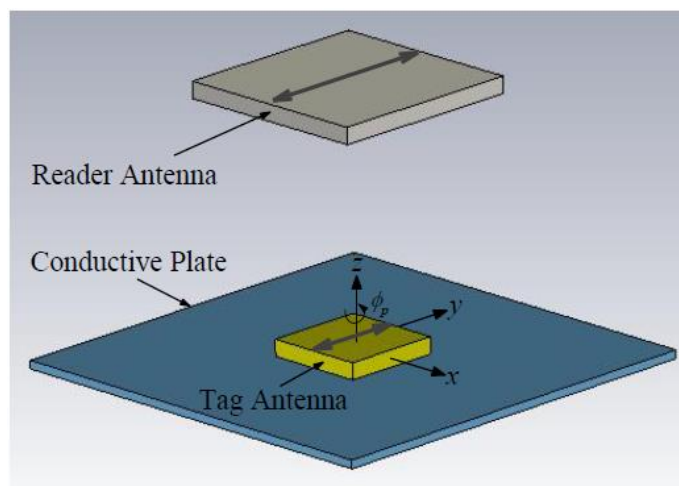
Figure 2.15. Polarization measurement setup.

2.3.2 Read Pattern Measurement

The radiation characteristics of a tag antenna can be visualized from its read pattern measurement. The reader antenna is fixed in the *z*-direction, as shown in Figure 2.16(a), and the read patterns in the *yz* and *xz* planes are generated by rotating the tag antenna about its *x* and *y* axes, respectively. As illustrated in Figure 2.16(b), the reader antenna is fixed along the *x*-axis, while the tag antenna rotates along its *z*-axis, for *xy* plane measurement. However, this *xy*-plane measurement setup is simple for characterizing the azimuthal read pattern.
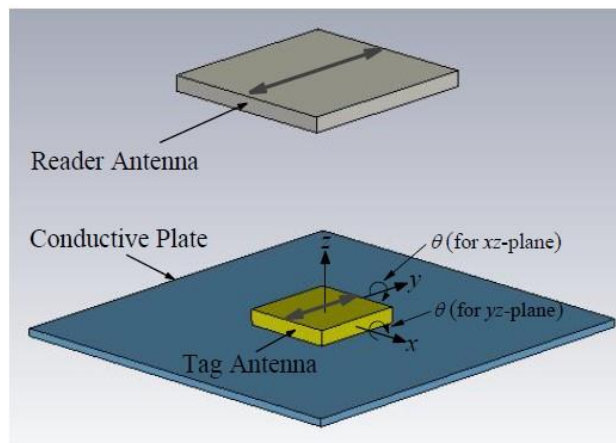
(a)
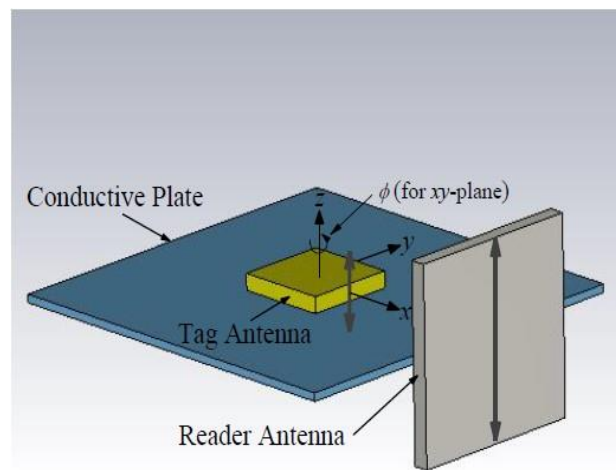
(b)

Figure 2.16. Read pattern measurement setup (a) *xz*, *yz* planes and (b) *xy* plane.

CHAPTER 3

COMPACT RING ANTENNAS WITH HIGH-IMPEDANCE LINE LOADED WITH DISTRIBUTED INDUCTORS

3.1   Introduction

In this chapter, a square ring resonator loaded with two distributed inductors is employed for designing a compact metal-mountable UHF tag antenna. The ring resonator, which is simple in geometrical shape, has been explored for designing different types of antennas and microwave circuits (Hsieh and Chang, 2005). The resonance modes of a closed ring are usually in the multiple of its operating wavelength. A ring resonator that works in the fundamental mode, where the circumference is approximately one guided wavelength, is simply too large to be useful for the UHF RFID (860 - 960 MHz) tag design. The proposed tag antenna has a low profile (~ 0.01λ). Also, for the first time, the distributed inductor is used together with a T match for miniaturizing the antenna size and improving the impedance matching. The employment of the two tuning mechanisms has not only brought down the tag resonance frequency successfully to the regulated UHF passband. But it has also enhanced the antenna resistance adequately so that a conjugate match can be achieved between the antenna and the chip. It will be shown that the inductor's value has to be properly adjusted according to its location on the ring due to the variation in current intensity.

Although the ring resonator has long been utilized for designing tag antennas for non-metal surfaces such as human body (Amendola et al., 2015) and dielectric objects, to our best knowledge, very little work has been done exploring its application on conductive surfaces. This is because placing the ring resonator in close proximity to metal is always very challenging due to the generation of image currents. This chapter has shown that incorporating distributed inductors into a ring resonator can improve its impedance characteristics, making it useable for tag design on metal.

Several design techniques have been applied to miniaturize the ring size and optimize the tag performance in recent years. The aperture shape inside a ring resonator (Okano, 2006) could be modified to broaden the bandwidth of a tag antenna with a 50 Ω port. This antenna, however, can never be used in practice as the RFID chip impedance is always complex. Multiple lumped capacitors (Taylor and Batchelor, 2019) and distributed capacitors (Liu et al., 2013) were integrated with a ring resonator to miniature the tag footprint and achieve a conjugate impedance match with the chip. A ring was meandered in many folds (Chen et al., 2016) for designing a compact circularly polarized tag antenna (58.6 mm $\times$ 58.6 mm) that was able to reach a very far read range (~ 20 m). However, the above-mentioned tag antennas can't be used on metal surfaces as the induced image currents can cause the radiation performances to deteriorate significantly. So that, in this proposed tag design, a ground plane is inserted to isolate the ring radiator from the backing metal.

3.2   Antenna Configuration and Design Analysis

3.2.1   Tag Antenna Configuration

Figures 3.1(a) and 3.1(b) show the schematic structures of the proposed tag antennas, both of which are excited by a UCODE 8 microchip through an inductive matching loop. The chip has a read sensitivity of −20.58 dBm with an input impedance of $13 - j191$ Ω at 915 MHz. The top metallic layers are made out of a thin copper film (thickness: 0.009 mm) that was pre-deposited on top of a thin polyethylene terephthalate (PET) film with a thickness of 0.05 mm. The prototypes can be conveniently fabricated using the conventional PCB etching procedure. To make the subsequent discussion easier, the tag antenna configurations in Figures 3.1(a) and 3.1(b) are named as *Tag A* and *Tag B*, respectively. A flexible foam block with a permittivity of $\varepsilon_r = 1.06$ and a loss tangent of tan $\delta = 0.0001$ is employed as the substrate, and it is sandwiched in between the radiator and the ground. The substrate is square in shape with $w \times l$ mm^2 and it has a thickness of 3.2 mm. For each tag antenna, the top layer locates the radiator while the bottom is the ground. The radiator on the top mainly comprises a ring antenna that is built from a high-impedance line (~ 140 Ω). A T-match loop is employed for improving the impedance matching. With reference to Figure 3.1(a), *Tag A* has two distributed inductors, which are made using meandered inductive lines, cascaded in series on the opposite side of the microchip. Figure 3.1(b) shows the configuration of the second proposed tag antenna – *Tag B*. It consists of two distributed inductors which are placed in opposite on the top and bottom arms. It will be later shown that *Tag A* and *Tag B* require different design strategies due to the

32

variation of the current distribution on the ring resonator. The design processes will be further elaborated when the establishment of the transmission line models is discussed later.
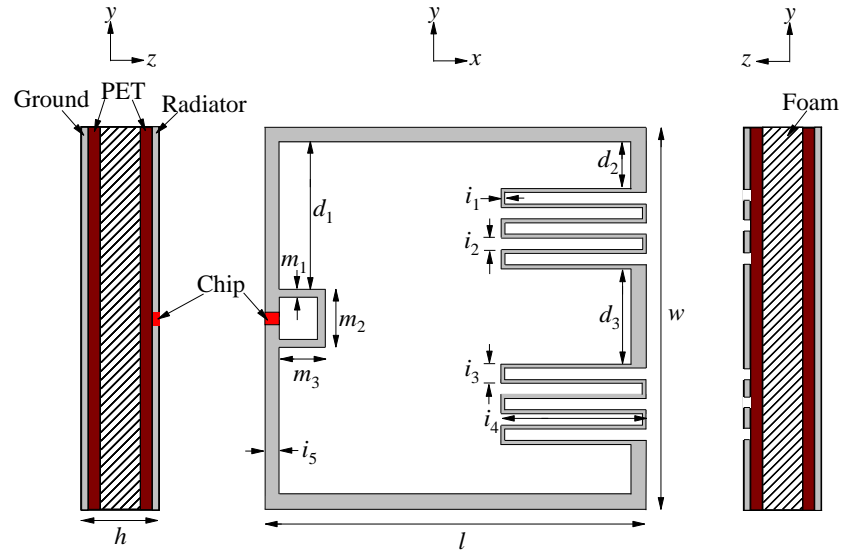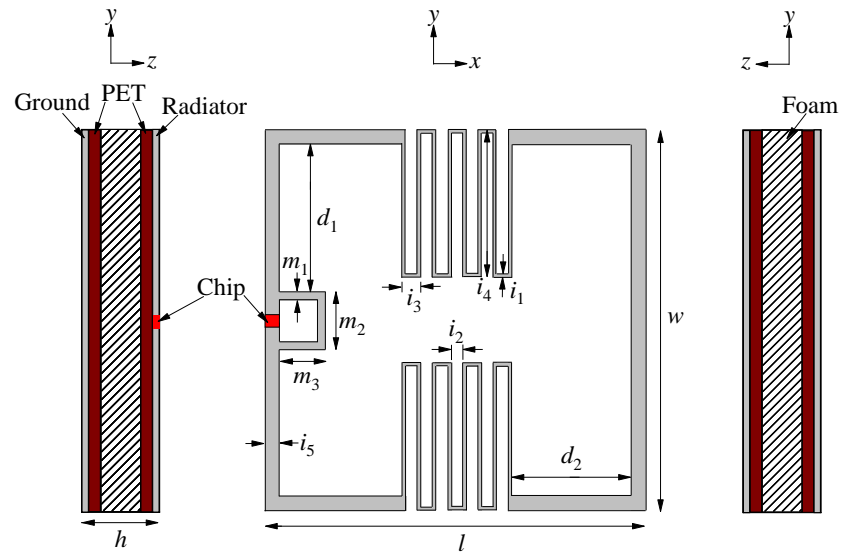
Figure 3.1. Design structures of (a) *Tag A* ($l = 50$, $w = 50$, $h = 3.318$, , $m_1 = 1$, $m_2 = 7.55$, $m_3 = 6$, $i_1 = 0.5$, $i_2 = 1.5$, $i_3 = 2.5$, $i_4 = 19$, $i_5 = 2$, $d_1 = 19.225$, $d_2 = 6.25$, $d_3 = 12.5$), (b) *Tag B* ($l = 50$, $w = 50$, $h = 3.318$, $m_1 = 1$, $m_2 = 7.55$, $m_3 = 6$, $i_1 = 0.5$, $i_2 = 1.5$, $i_3 = 2.5$, $i_4 = 19$, $i_5 = 2$, $d_1 = 19.225$, $d_2 = 15.75$). All are in mm.

The top views of the prototypes are shown in Figure 3.2. For ease of fabrication, the microchips are first bonded across a pair of PET flaps. The two ends of the flaps are then soldered to the ring antenna for feeding purposes. The tag antenna can also be directly etched on a rigid substrate such as FR4 to enhance its mechanical stiffness. In fact, the tag size can be further scaled down by half if it is to be made using a FR4 substrate. The main reason to employ PET (polyethylene terephthalate) substrate in the design is to make the antenna structure slightly flexible. In the design process, we have included the PET substrate into the simulation model. The soft foam material is used for providing slight flexibility as well so that the tag can be applied on a slightly uneven backing object.
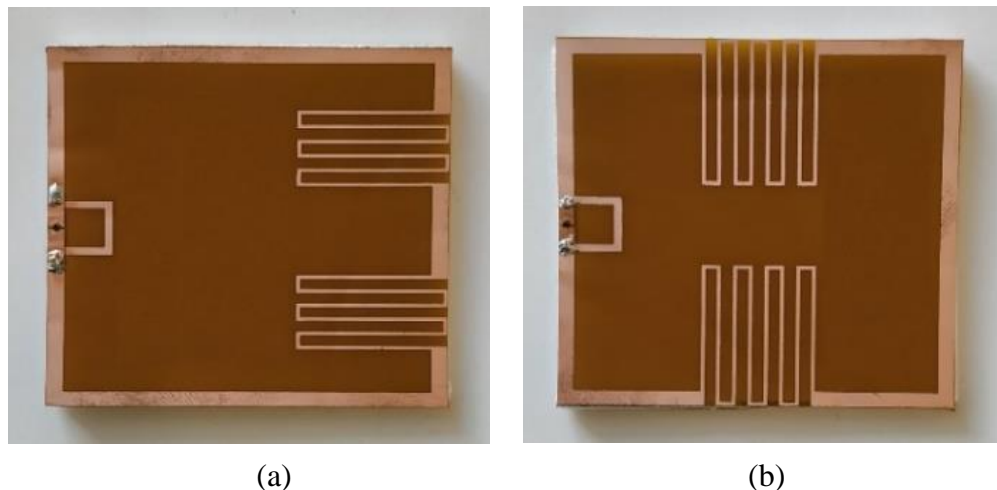
(a)   (b)
Figure 3.2. Prototypes of (a) *Tag A* and (b) *Tag B*.

3.2.2   Analysis of Ring Resonator

It is essential to understand the currents, fields, and impedance characteristics of the electrically small ring resonator before incorporating the distributed

inductors into the tag design. To start, the footprint of the antenna is fixed to be 50 mm × 50 mm. The analysis starts with a simple square ring antenna, which has the same high-impedance microstrip line (i_5), a T-match loop, as well as a ground plane on the reverse surface, as shown in Figure 3.3(a). With reference to the surface current distribution in Figure 3.3(a), two current standing wave patterns are clearly seen, with two nulls on the top and bottom arms, along the perimeter of the ring. For this resonance, the perimeter of the ring is about λ_g, and it is in the multiple of guided wavelength $n\lambda_g$, where the mode number is $n = 1$ in this case. The current distribution shows that it is not an antiresonance. Since the tag antenna is meant for metal-mountable applications, it is placed at the center of a 20 cm × 20 cm metal plate for all the subsequent simulation processes. With reference to Figure 3.3(b), the self-resonance frequency (mode number $n = 1$) of this ring resonator is found to be 1.477 GHz (shown in Figure 3.3(c)), which is quite close to the one-wavelength fundamental resonance mode at $\lambda_g \sim 1.5$ GHz, as can be observed from the distribution of the surface current in Figure 3.3(a), where this current standing wave can be described as a function of $I(x') = I_0 \sin(\beta x')$ (Hsieh and Chang, 2005) with its differentiation expressed as $\frac{dI(x')}{dx'} = I_0 \cos(\beta x')$. Therefore, the instantaneous voltage and current at any point on the high-impedance line, which is illustrated in Figure 3.3(b) from A to A', can be related by $V(x') = L\frac{dI(x')}{dx'} = LI_0 \cos(\beta x')$. Obviously, the inductance effect depends on the gradient of the current change on the line. With reference to Figure 3.3(c), the tag resonance frequency is located at 1.4 GHz. For the RFID community, the tag resonance frequency is defined as the frequency at which

the antenna impedance is at conjugate match with the chip impedance. At the tag resonance, the antenna impedance and realized gain are found to be $4.51 + j192.24$ Ω and 4.12 dBi, respectively. Here, however, the antenna resistance is too low, and it cannot achieve a conjugate matching level with the microchip. It was also found from the simulation that, for this simple antenna, the ring footprint had to be enlarged to at least 90 mm $\times$ 90 mm if the tag resonance frequency were to be designed within the UHF passband. The reason for obtaining the differentiation $I'(x)$ is to explain that the required inductance of the distributor inductor is depending on its location along the ring as $V(x') = L\frac{dI(x')}{dx'}$. It is observed that *Tag B* requires a larger inductance value as the distributed inductors are located near to the nulls, where $\frac{dI(x' = 0\text{mm})}{dx'} = 0$ and $\frac{dI(x' = 100\text{mm})}{dx'} = 0$, of the ring resonator, as can be seen in Figure 3.3(b). This is because L is required to be higher when $\frac{dI(x')}{dx'}$ becomes lower. As $\frac{dI(x')}{dx'}$ changes, the requirement on the inductance is also different. This explains why *Tag A* and *Tag B* require different inductances when the meandered-line inductors are loaded at different locations on the ring. To reduce the tag resonance frequency and miniaturize the footprint, two distributed inductors are incorporated into the ring resonator to form *Tag A* and *Tag B*, respectively, and their current distributions are shown in Figures 3.4(a) and 3.4(b). The tag resonance frequency of *Tag A* is found to have lowered to 915 MHz, where the corresponding antenna impedance and realized gain are $14.99 + j190.35$ Ω and -4.0 dBi, respectively. For *Tag B*, its tag resonance frequency is found to be 919 MHz and the corresponding input impedance and realized gain are $17.58 + j189.40$ Ω and -4.5 dBi, respectively.

With reference to Figures 3.4(a) and 3.4(b), the current intensities on the high-impedance line, including those on the distributed inductors, still follow the standing wave pattern, as was discussed in Figure 3.3. For *Tag A*, as can be seen in Figure 3.4(a), its current intensity is found stronger when it comes near to the central portion of the right arm as there is a crest in the standing wave, which coincides with the current distribution in Figure 3.3(a). On the other hand, the nulls of the ring resonator are reflected at the centers of the top and bottom inductors of *Tag B*, as can be seen in Figure 3.4(b). Due to this reason, the required inductances for *Tag A* and *Tag B* are different. The corresponding radiation patterns for *Tag A* and *Tag B* are shown in Figure 3.5. Broadside radiation has been observed in both, which is typical for a ring resonator with $n = 1$. For the two cases, their radiation patterns and antenna gains are quite similar, implying that the locations of the distributed inductors do not affect far-field characteristics much.
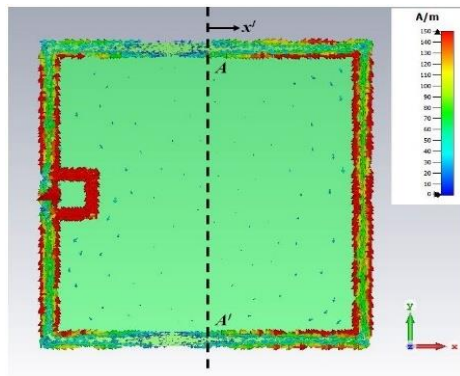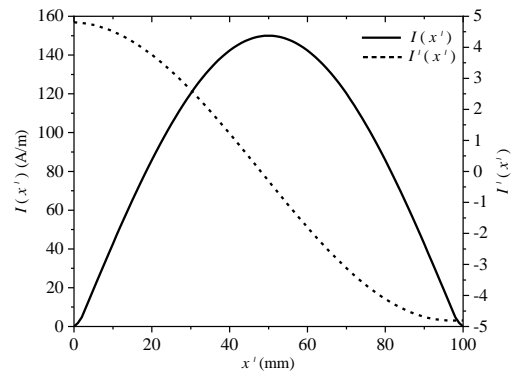
(a)   (b)
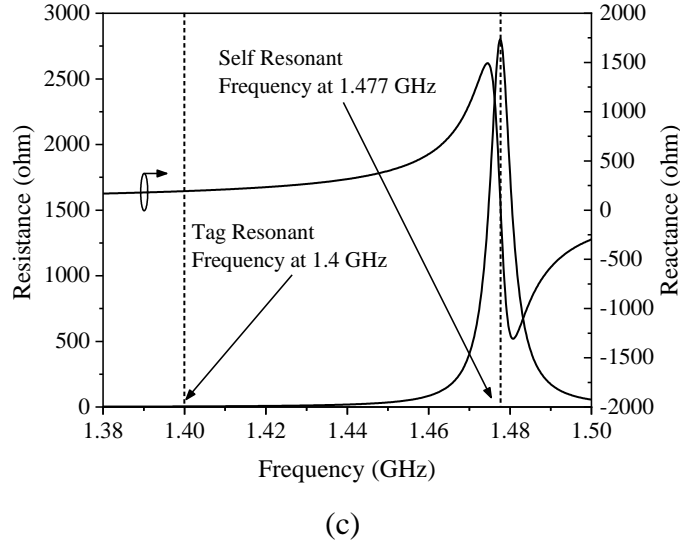
(c)

Figure 3.3. (a) Surface current distribution of the simple ring antenna at 1.4 GHz. (b) The intensity of current distribution on the ring antenna. (c) Input impedance.

Simulations have been conducted to study the effects of the distributed inductors on the radiation efficiency. With the loading distributed inductors removed from *Tag A* (Figure 3.3(a)), the radiation efficiency (e_r) is found to be −4.163 dB (~ 38%) at the tag resonance frequency of 1.4 GHz, which is too high to be usable for the regulated UHF RFID passband. Due to the poor impedance matching between the antenna and the chip, the power transmission coefficient (τ) is found to have deteriorated to ~ 0.7. We have also found out from the simulation that the ring footprint has to be enlarged by 80% (90 mm × 90 mm) in order to tune down the tag resonance frequency to the regulated passband. This dimension is simply too large for most of the commercial applications. Next, with the inclusion of the two distributed inductors, the radiation efficiency of *Tag A* has reduced to −12.19 dB (~ 6%). The reduction of e_r here is mainly due to two reasons. Firstly, reducing the frequency from 1.4 GHz to 915 MHz has caused the electrical size of the

antenna to decrease from 0.234 λ_g to 0.153 λ_g, which makes e_r to become much smaller. The second reason for efficiency reduction is due to the increase of ohmic loss, which is being introduced by the two distributed inductors. Despite the decrease in the radiation efficiency, the power transmission coefficient has been enhanced to τ ~ 0.99, due to the improvement of the impedance matching. In summary, there is a tradeoff when the distributed inductors are inserted into the ring resonator for miniaturizing the tag size. A similar effect is also seen for *Tag B*.

(a)   (b)
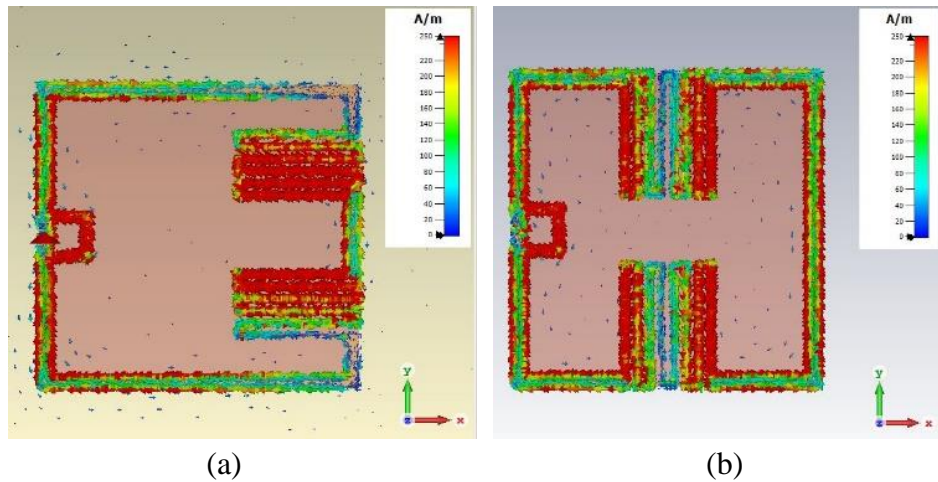
Figure 3.4. Surface current distributions on (a) *Tag A* at 915 MHz, (b) *Tag B* at 919 MHz.

(a)   (b)
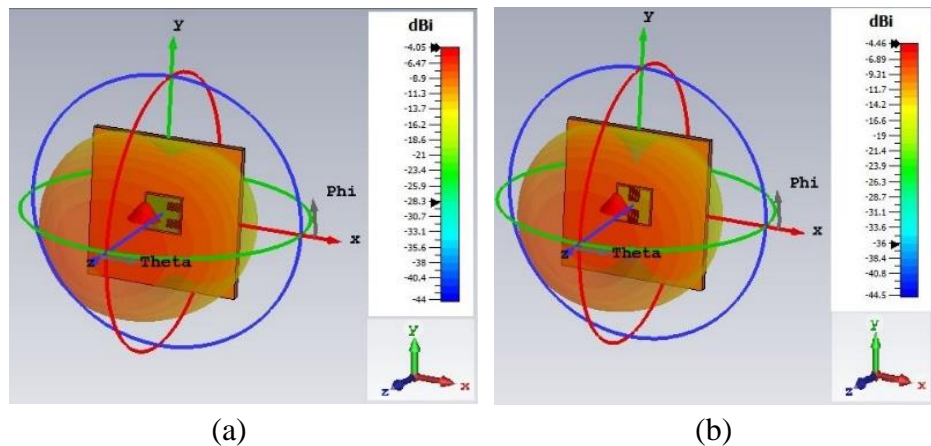
Figure 3.5. 3-D simulated radiation patterns for (a) *Tag A*, (b) *Tag B*.

3.2.3   Design Procedure and Transmission Line Model

The design starts with building the transmission line (TL) models, which represent the two proposed tag antennas, respectively, as shown in Figure 3.6. For both cases, the inductors are to be adjusted such that the tag resonance frequency for each tag falls somewhere within 902 – 920 MHz. Again, the CST Microwave Studio Suite is used for simulating the TL characteristics. First, the entire ring antenna is segmented. Knowing that the current intensity on the high-impedance line changes with its position, as discussed in the previous section, accurate segmentation is required for establishing the TL models. The high-impedance lines and the T-match networks are modeled using multiple sections of transmission lines, each of which represents a segment of microstrip. Bends and T-junctions are employed to accurately describe the TL characteristics. To ease the design procedure, a lumped element model (Acua et al., 2001) will be employed for modelling the distributed inductors. A meandered-line distributed inductor can be represented by a lumped element model consisting of an inductance (L), a capacitance (C), and a resistance R_c (loss resistance $R_l \sim 0$) in parallel, where $Z_L = L||C|| R_c$, as shown in Figure 3.7. Derivation is now demonstrated for *Tag A*, which has three turns ($N = 3$), and *Tag B*, which has four turns ($N = 4$). The design parameters of the meandered lines are $i_1 = 0.5$ mm, $i_2 = 1.5$ mm, $i_4 = 19$ mm, and the substrate thickness is $h = 3.2$ mm. With reference to (Acua et al., 2001), the inductance can be calculated as

$$L = N\left[k_1 l_e \ln\left(\frac{D - l_e}{D + l_e}\right) + k_2 s_e \ln\left(\frac{E - s_e}{E + s_e}\right)\right.$$

$$+ k_3 l_e \ln\left(\frac{l_e + B}{i_1}\right) + k_4 \frac{l_e^2}{i_1} \ln\left(\frac{i_1 + B}{l_e}\right)$$

$$\left. + k_5 \frac{s_e^2}{i_1} \ln\left(\frac{i_1 + A}{s_e}\right)\right]$$

$$+ \left[k_6 l_e \cdot \left(\ln\left(\frac{l_e + B}{i_1}\right) - \ln\left(\frac{D - l_e}{D + l_e}\right)\right)\right.$$

$$+ k_7 s_e \ln\left(\frac{E - s_e}{E + s_e}\right) + k_8 \frac{l_e^2}{i_1} \ln\left(\frac{i_1 + B}{l_e}\right)$$

$$\left. + k_5 \frac{s_e^2}{i_1} \ln\left(\frac{i_1 + A}{s_e}\right)\right] (\text{nH})$$

$$(3.1)$$

where

$$l_e = i_4 - i_1$$
$$s_e = i_2 + i_1$$
$$A = \sqrt{s_e^2 + i_1^2}$$
$$B = \sqrt{l_e^2 + i_1^2}$$
$$D = \sqrt{l_e^2 + s_e^2}$$
$$E = \sqrt{s_e^2 + h^2}$$

and $k_1 = 1.09$, $k_2 = 2.6$, $k_3 = -0.11$, $k_4 = 4.24$, $k_5 = 1.96$, $k_6 = 0.37$, $k_7 = 0.42$, and $k_8 = -0.5$.

The capacitance can be calculated as

$$C = N(k_1 i_4 + k_2 i_4 . i_1 + k_3 + k_4 i_1 + k_5 i_4 . i_2 + k_6 i_2)$$
$$+ k_7 i_4 + k_1 i_4 . i_1 + k_8 i_1 + k_9 i_4 . i_2 + k_3 i_2 \text{ (pF)}$$

$$(3.2)$$

and $k_1 = -1.1$, $k_2 = 0.13$, $k_3 = 4.41$, $k_4 = -3.91$, $k_5 = 0.26$, $k_6 = -2.97$, $k_7 = -0.11$, $k_8 = 4.17$, and $k_9 = 0.64$.

The resistance can be calculated as

$$
\begin{aligned}
R_C = N \Big[\frac{1}{i_1} \big(& k_1 i_2{}^2 i_4{}^2 + k_2 i_2{}^2 i_4 + k_3 i_2{}^2 + k_4 i_2 . i_4{}^2 \\
& + k_5 i_2 . i_4 + k_6 i_2 + k_7 i_4{}^2 + k_8 i_4 + k_9 \big) \\
& + k_{10} + k_{11} N^2 + k_{12} i_4{}^3 \Big] \\
+ \frac{1}{i_1} \big(& k_{13} i_2{}^2 i_4{}^2 + k_{14} i_2{}^2 i_4 + k_{15} i_2{}^2 + k_{16} i_2 . i_4{}^2 \\
& + k_{17} i_2 . i_4 + k_{18} i_2 + k_{19} i_4{}^2 + k_{20} i_4 + k_{21} \big) \\
+ k_{22} & + k_{23} N^2 + k_{24} i_4{}^3 \; (\Omega)
\end{aligned}
$$

(3.3)

and $k_1 = 86$, $k_2 = -1457$, $k_3 = -764$, $k_4 = 132$, $k_5 = -414$, $k_6 = -530$, $k_7 = -103$, $k_8 = 861$, $k_9 = -2.87$, $k_{10} = 2256$, $k_{11} = 17$, $k_{12} = -20.14$, $k_{13} = 275$, $k_{14} = -41$, $k_{15} = -230$, $k_{16} = -389$, $k_{17} = 578$, $k_{18} = -83$, $k_{19} = -66$, $k_{20} = 1467$, $k_{21} = 113$, $k_{22} = -602$, $k_{23} = -242$, and $k_{24} = -0.22$.

With the use of (3.1)-(3.3), the numerical values of the elements for *Tag A* are calculated to be ($L = 49.03$ nH, $C = 0.425$ pF, and $R_C = 29.15$ kΩ); while the elements' values for *Tag B* are ($L = 65.37$ nH, $C = 0.956$ pF, and $R_C = 26.27$ kΩ). To work in the regulated UHF passband, obviously, *Tag B* requires a much higher inductance as the locations of the two distributed inductors coincide with the two nulls of the ring resonator, as explained in the previous section. Due to the decrease of $\frac{dI(x')}{dx'}$ around the null position, as can be seen in Figure 3.3(b), a higher inductance (L) is therefore needed here.

The transmission line model is commonly used to analyse and design the antenna's behaviour. It uses multiple transmission lines with certain electrical parameters to represent the antenna structure. Although it does not include radiation, the transmission line model simplifies the analysis and design of a tag antenna, providing a basic understanding of its behaviour.
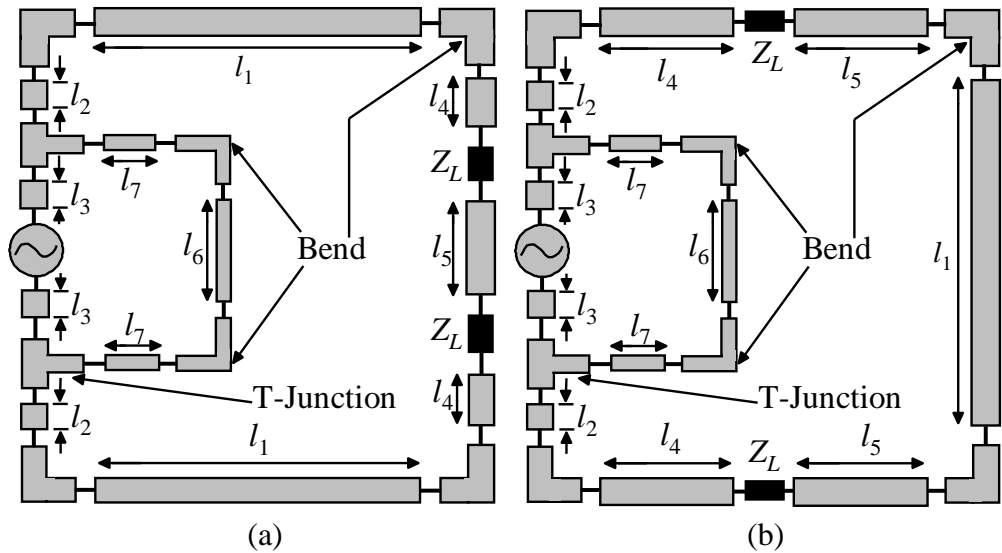
Figure 3.6. Transmission line models for the proposed tag antennas. (a) *Tag A* ($l_1 = 50$, $l_2 = 19.225$, $l_3 = 2.6$, $l_4 = 6$, $l_5 = 12.5$, $l_6 = 5.55$, $l_7 = 5$). (b) *Tag B* ($l_1 = 50$, $l_2 = 19.225$, $l_3 = 2.6$, $l_4 = 18$, $l_5 = 18$, $l_6 = 5.55$, $l_7 = 5$). All are in mm.
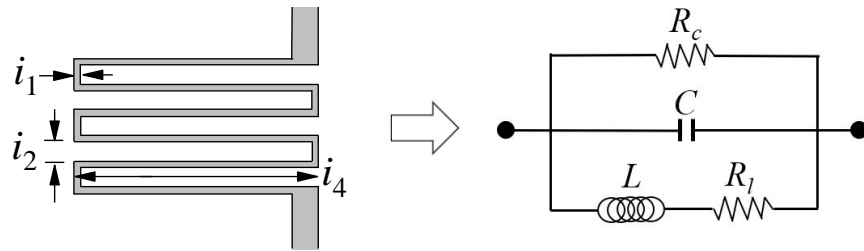
Figure 3.7. Lumped element model of the meandered-line inductor.

A design procedure has been given to show how to apply the TL model. The design process usually starts with a given tag size. For the proposed tag, it is to fit within a footprint of 50 mm × 50 mm, where the foam being employed has a thickness of 3.3 mm. First, the TL sections of the high-impedance lines and the T-match networks of the ring antenna are entered into the two-dimensional circuit simulator of the CST Microwave Studio, as shown in Figure 3.6. Here, the distributed meandered-line inductor is converted into a lumped element model, as shown in Figure 3.7, where the corresponding L, C, R_l, and R_c (~ 0 Ω) can be easily tuned and simulated together with all the TL

43

sections so that an optimum design can be obtained. By knowing the required inductance and capacitance, the geometrical dimension of the meandered-line inductor can be determined. After obtaining all the optimum design parameters, the ring antenna can be constructed and verified through conducting a full-wave simulation using the CST Microwave Studio. Designing and tuning the TL model using the circuit simulator is much faster than using the full-wave simulator as the former requires much less computational resources and it can be done in a faster manner. For example, performing one full-wave simulation on the ring antenna with the loaded distributed inductors can take up 20 minutes, but the TL model can be simulated within 1 second.
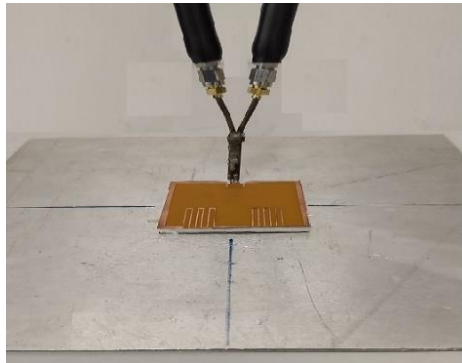
Figure 3.8. Measurement setup of the input impedance using a differential probe.

A differential probe and a vector network analyzer (shown in Figure 3.8) are used to measure the input impedance of the proposed tag antenna. The tag without a microchip is first measured by attaching the differential probe to the bonding pads. Curves for the resistances and reactances that are generated from the TL models as well as those generated by the CST simulation are then compared with the measured results. Also given is the conjugate chip

impedance. The results for the two tags are respectively illustrated in Figures 3.9(a) and 3.9(b) for ease of comparison. For both cases, the modeled curves are found to agree very well with their simulated and measured counterparts. The modeled antenna impedance for *Tag A* is found to be 15.65 + *j*190.15 Ω at the tag resonance of 912 MHz, which is very close to the CST-simulated impedance of (14.99 + *j*190.35 Ω) at 915 MHz as well as the measured one (14.56 + *j*190.27 Ω) at 913 MHz. It is almost in conjugate match with the chip impedance (13 – *j*191 Ω). On the other hand, *Tag B* has a modeled antenna impedance of (16.33 + *j*189.97 Ω) at 914 MHz and a simulated antenna impedance of (17.58 + *j*189.40 Ω) at 919 MHz, both of which are quite close to the measured antenna impedance (15.21 + *j*189.12 Ω) at the tag resonance of 916 MHz. Again, good impedance matching is observed between the antenna and the microchip.
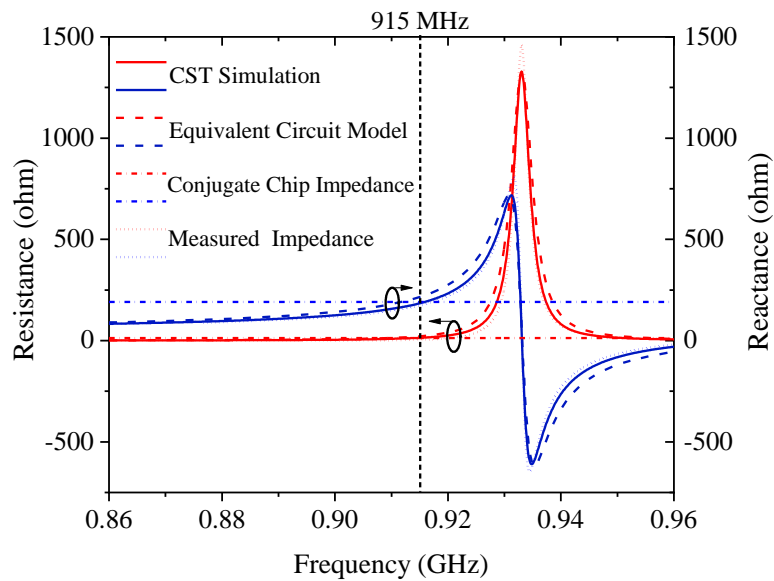
(a)
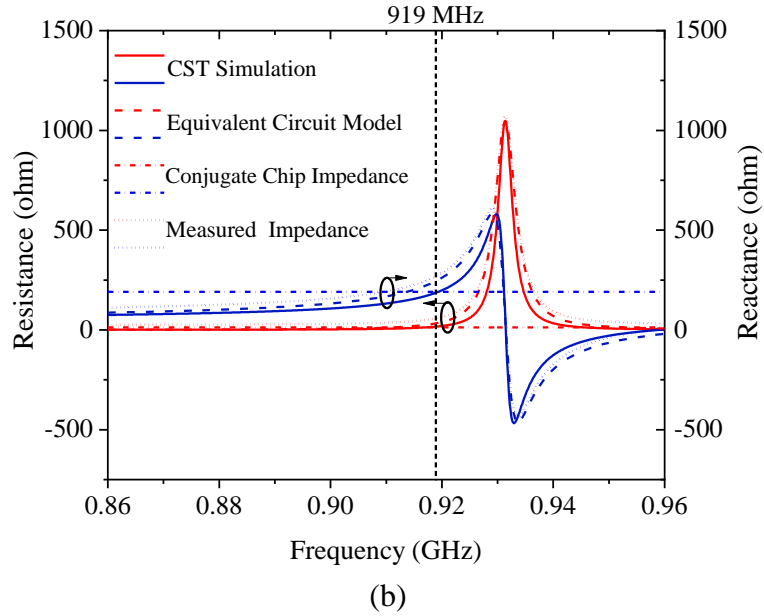
Figure 3.9. Measured, simulated, and modeled input impedances of the proposed antenna (a) *Tag A*, (b) *Tag B*.

3.3   Parametric Analysis

Parametric analysis has been performed to study the effects of the distributed inductors. By decreasing the line width (i_1), as can be seen in Figures 3.10(a) and 3.10(b), the tag resonance frequencies of both the tag configurations (*Tag A* and *Tag B*) decrease due to increasing inductance. In all cases, the antenna impedances can be easily made conjugate so that they can match with the chip impedance. As a result, as can be seen in Figures 3.11(a) and 3.11(b), the maximum power transmission coefficient can be maintained > 0.98 for all cases as the antenna impedance is matched well with the chip impedance.

Simulation has been conducted to study the effects of the substrate height on the bandwidth, read range, and realized gain. The 3dB bandwidth (~ 0.8 %) is found to be quite stable, and it is not affected much by changes in the substrate height. Also observed is that the realized gain reduces when the substrate gets thinner, causing the read range to decrease as well.
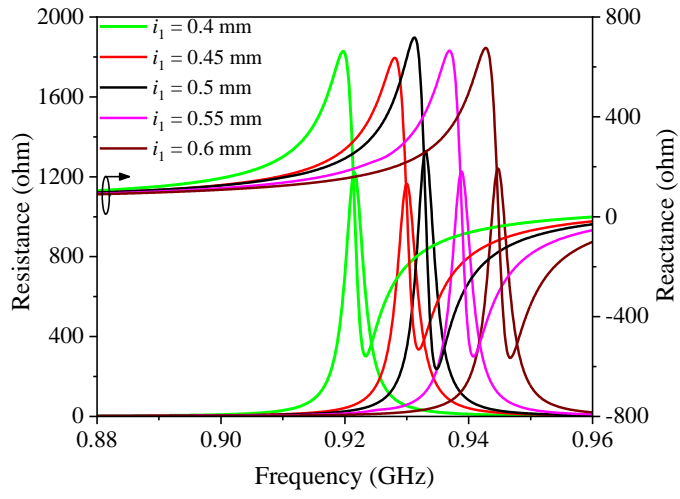
(a)
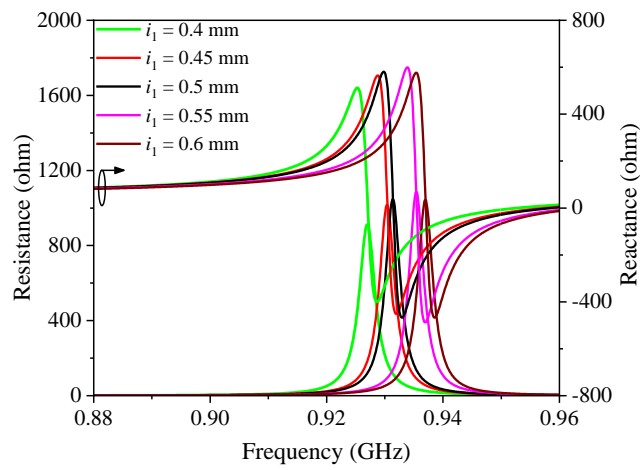
(b)

Figure 3.10. Effects of varying the line width i_1 on the antenna impedance for (a) *Tag A*, (b) *Tag B*.

(a)
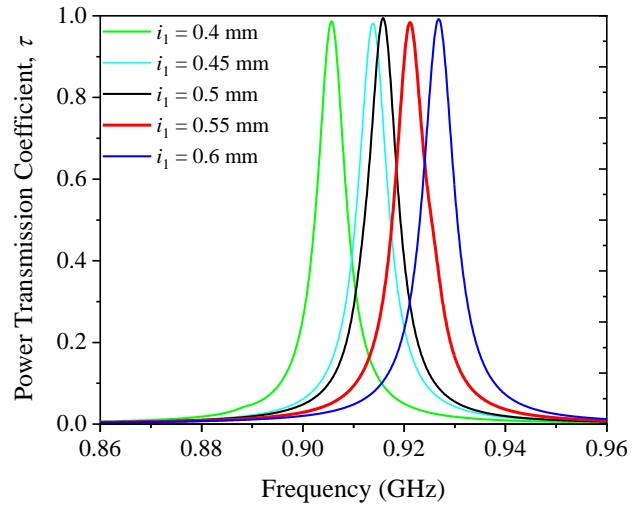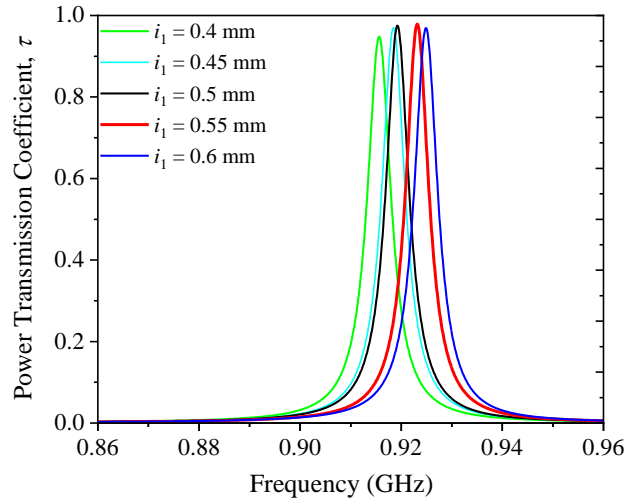
Figure 3.11. Effects of varying the line width i_1 on the power transmission coefficients for (a) *Tag A*, (b) *Tag B*.

3.4 Measurement Setup

The read performances of the proposed UHF RFID tag antennas are measured using the Voyantic Tagformance measurement system, which is specially designed for measuring the maximum read distance, resonance frequency, tag sensitivity, and realized gain automatically in an anechoic environment. An 8 dBi reader antenna is used for characterizing the proposed tags. In the measurement processes, the transmitting and receiving antennas are aligned such that their polarizations are aligned so that the matching factor is near to unity. Figure 3.12 shows the experimental setup inside an anechoic cabinet. The proposed tag antenna is placed at the center point of a 20 cm × 20 cm metal plate throughout the entire measurement process, and the linearly polarized antenna is used for measuring and receiving the backscattered signals. Styrofoam with a relative permittivity of ~1 has been employed for supporting the metal plate and the tag antenna at a proper position inside the anechoic cabinet.
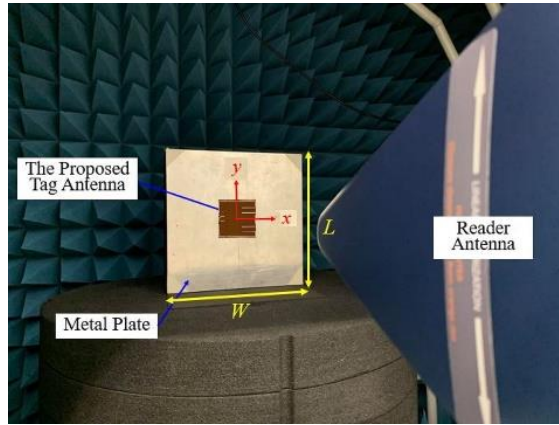
Figure 3.12. Measurement setup inside an anechoic cabinet.

3.5 Experimental Results and Discussion

Read distance and realized gain are the two most important parameters for characterizing the performances of an RFID UHF tag antenna. First, we discuss the procedure for measuring the realized gain of the tag antenna, which can be defined as $G = \frac{P_c}{L_l P_t}$, where P_c is the microchip read sensitivity (-20.58 dBm), L_l is the measured forward-link losses which include cable loss and free space path loss, and P_t is the reader threshold level at a specific frequency during the threshold power sweep. The maximum realized gain (G) and maximum power transmission coefficient (τ) can then be used to calculate the realized gain of the tag antenna ($G_r = \tau G$). A good impedance match between the microchip and the antenna is important for reducing the gain loss. Figures 3.13(a) and 3.13(b) show the measured and simulated realized gains, and the measured tag sensitivity for the two tags. The optimum tag sensitivity of *Tag A* is measured to be -19.19 at $\sim$ 915 MHz. The corresponding realized gain is measured -5.4 dB (Simulation: -5.6 dB). On the other hand, *Tag B* has

49

an optimum tag sensitivity of −19.38 dB at ~ 920 MHz. In this case, the maximum realized gain is measured to be −6.4 dB (Simulation: −6.7 dB). It was found that, for both cases, the discrepancies between the measurement and simulation are mainly contributed by the fabrication tolerances especially the air gap introduced by the lamination processes.
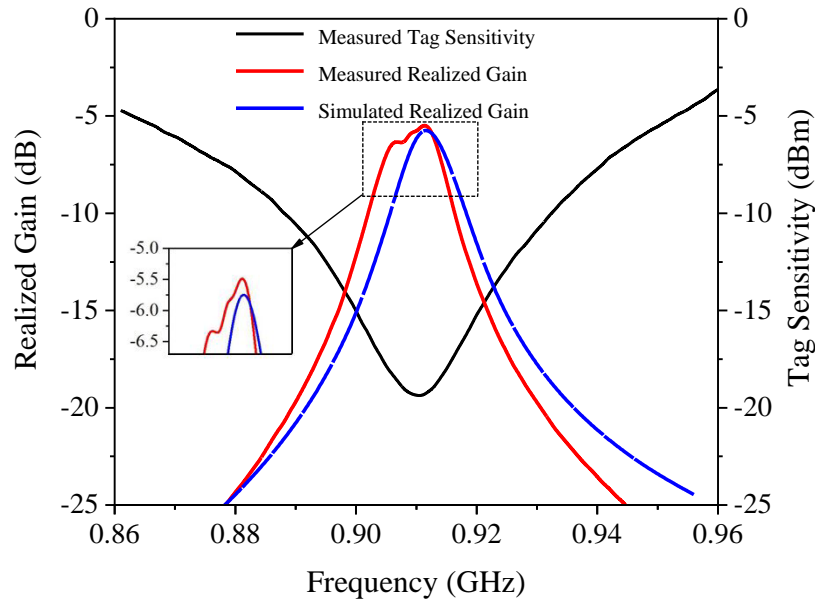
(a)
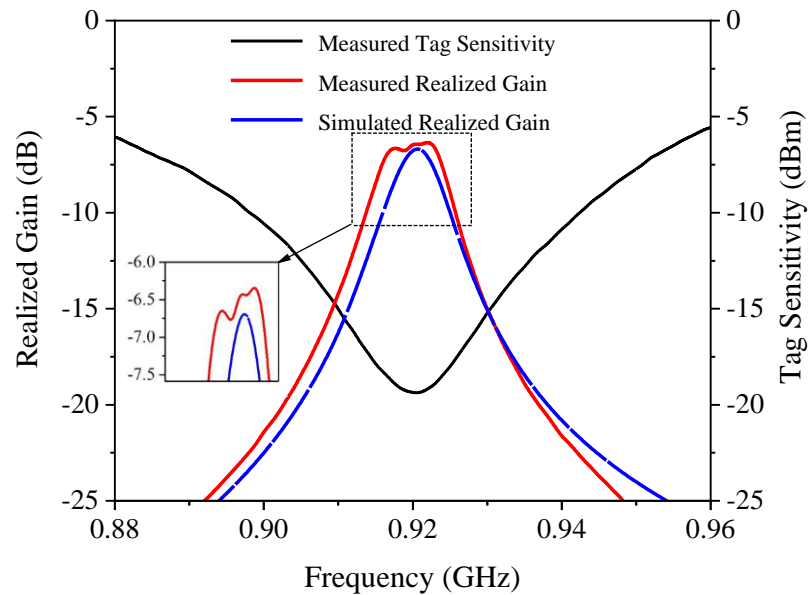
(b)

Figure 3.13. Measured and simulated realized gains and the measured tag sensitivity of (a) *Tag A*, (b) *Tag B* on a 20 cm × 20 cm metal plate.

Read distance is one of the most important parameters that can be used to characterize the performance of a tag antenna. A 4 W effective isotropic radiated power (EIRP) is used in all the subsequent measurements, which are done by using the tagformance measurement system. In the experiment, the reader antenna fixed at a constant distance and the tag antenna is placed upon a metal plate, where it is rotated for measuring the read patterns. For *Tag A*, the measured read patterns are shown in Figures 3.14(a) and 3.14(b) at the tag resonance frequency of 915 MHz in the *xy*-, *xz*- and *yz*- planes. From the *xy*-plane measurement, a maximum read distance of 9 m is measured at $\phi = -10°$ and $\phi = 170°$, and it shows that the tag antenna is linearly polarized. With reference to the *xz*- and *yz*-plane read patterns in Figure 3.14(b), the tag antenna is broadside, where it has a maximum radiation in the boresight direction ($\theta = 0°$). The front-to-back ratio is very high due to the existence of the backing metal plate. Here the maximum read distance in the boresight is found to be 8.5 m. The measured read patterns of *Tag B* are shown in Figures 3.15(a) and 3.15(b) at 919 MHz in the *xy*-, *xz*- and *yz*- planes. As can be observed from the *xy*-plane measurement, a maximum read distance of 7.5 m is measured at $\phi = 10°$ and $\phi = -170°$. Again, the radiation is broadside in nature, and it mainly distributes in the upper half plane.

In this research project, the achieved read range of 9 m is a result of using a highly sensitive RFID chip, especially the UCODE 8 flip-chip with a read sensitivity of -20.85 dBm and an input impedance of $13 - j191$ Ω at 915 MHz. This sensitive chip contributes to the extended read ranges obtained in the experiments. However, as mentioned in the datasheet, it is important to

51

note that the theoretical maximum read range, which is approximately 25 m, is achievable by integrating the same UCODE 8 chip with a dipole antenna. Our read range is 9 m falling short of the theoretical maxima, prompting a discussion on how to further improve the read range. To achieve a higher read range, several factors can be considered. First, optimizing the antenna and matching it more precisely to the RFID chip's input impedance can further enhance the tag's performance. Using RFID readers with a higher sensitivity can improve the system's ability to detect weak tag signals, thus increasing the read range. Identifying the optimal frequency for communication, which may vary depending on the application and environment, can impact the read range. Ensuring proper tag placement on the object being tracked and avoiding interference can contribute to better signal reception and extended read range. Analysing and adjusting the environment in which the RFID system operating can lead to better signal propagation and increased read range.

(a)　　　　　　　　　(b)
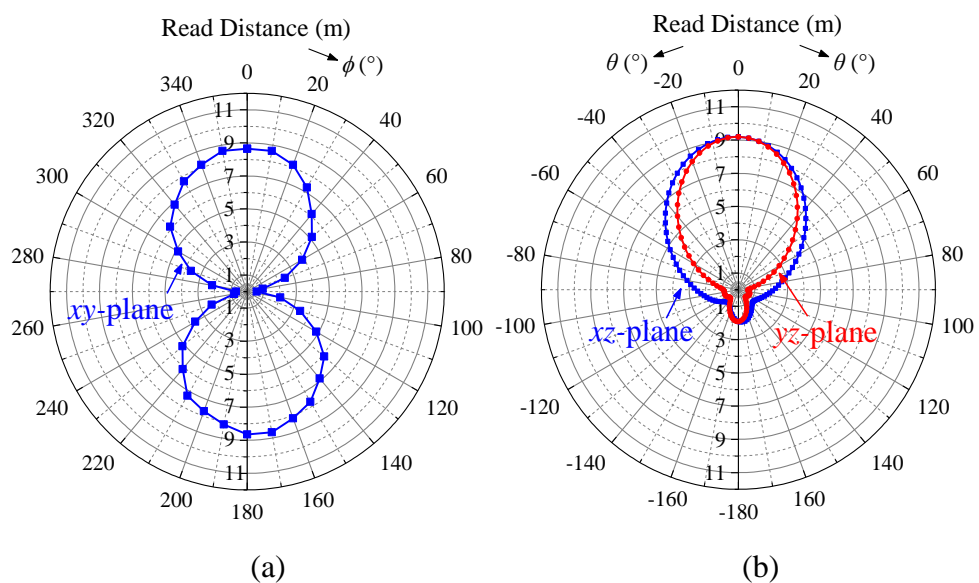
Figure 3.14.　Measured read distances of *Tag A* in the (a) *xy*-plane, (b) *xz*- and *yz*- planes at 915 MHz.

52
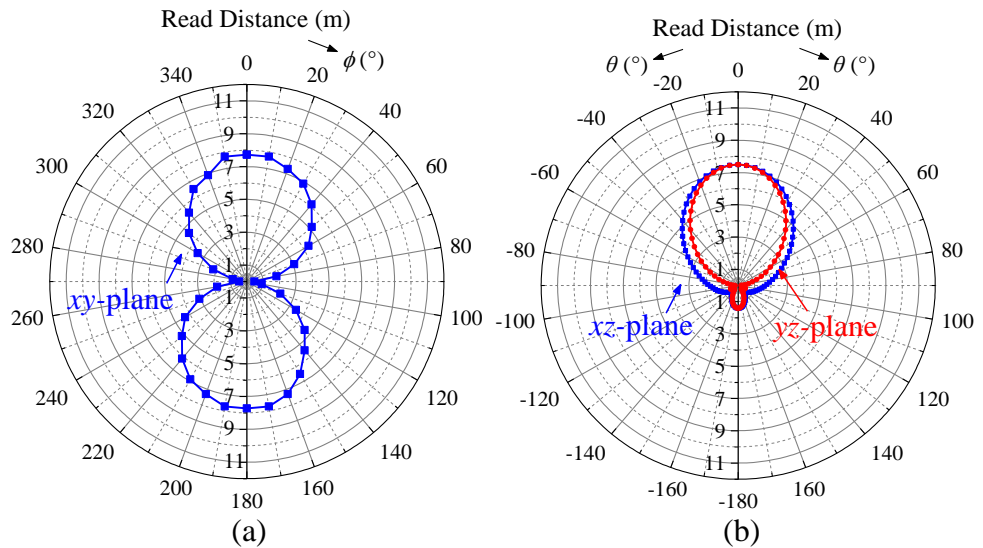
Figure 3.15. Measured read distances of *Tag B* in the (a) *xy*-plane, (b) *xz*- and *yz*- planes at 919 MHz.

Figures 3.16(a)-(d) show the read distances measured using different backing metal plates with different sizes in the boresight direction ($\theta = 0°$). The plate thickness is ~ 5 mm. To start, measurement is conducted by varying the plate length (*L*) from 8 cm to 24 cm and the plate width (*W*) is fixed at 20 cm. As can be seen from Figures 3.16(a) and 3.16(b), the tag resonance frequency of *Tag A* is very stable, and it is not affected much by changes in the plate dimension. When *W* is reduced to 8 cm, the read distance becomes slightly shorter (~ 8 m). The tag resonance for *Tag B*, similarly, is also very stable, as can be observed in Figures 3.16(c) and 3.16(d), where the read range falls within 6 m - 8.5 m. Stable tag resonance frequency is a very desirable feature for a UHF RFID metal-mountable tag antenna.

(a)

(b)

(c)

54
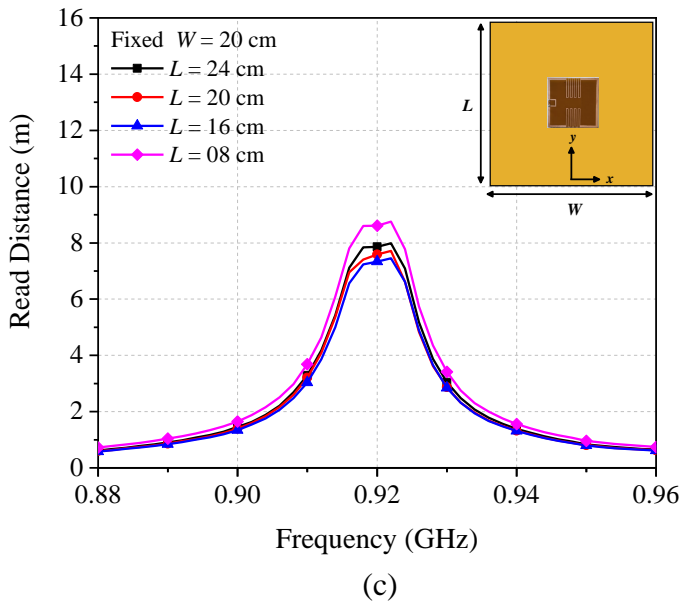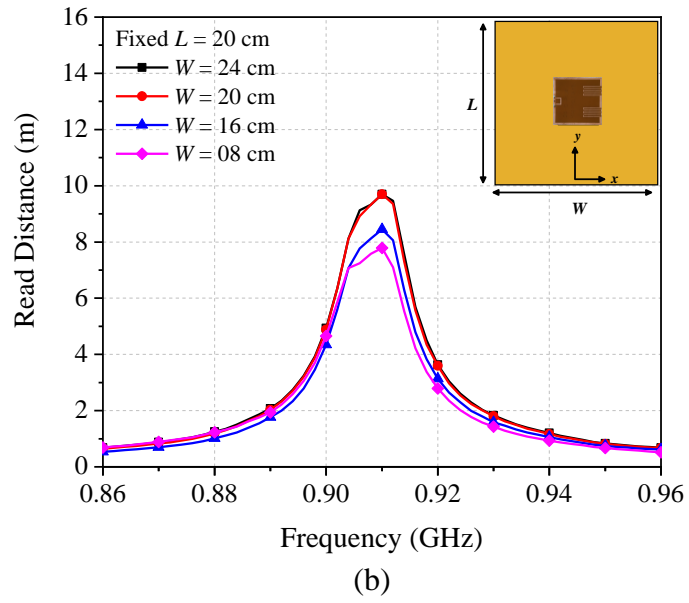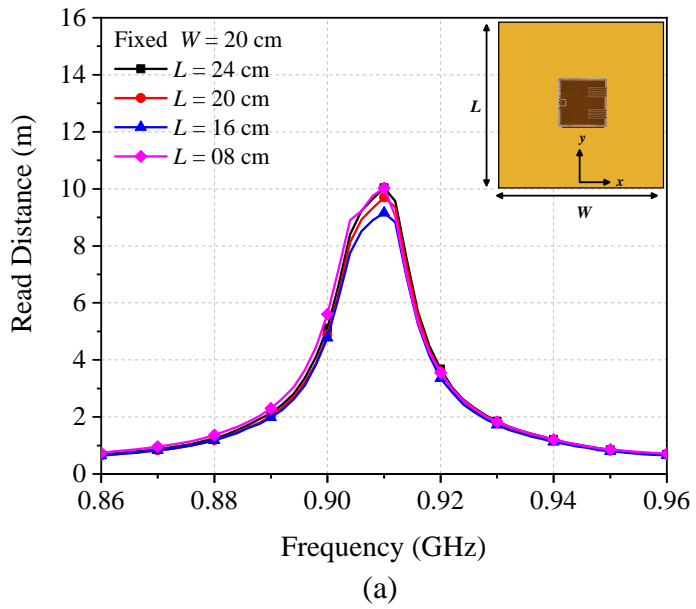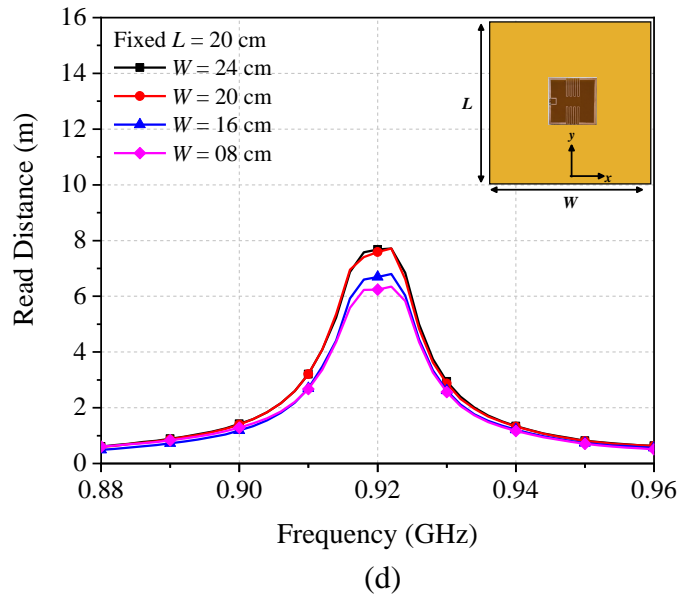
Figure 3.16. Measured read distances of the proposed tag antenna for metal plates with different widths and lengths: (a) *Tag A* with fixed *W*, (b) *Tag A* with fixed *L*, (c) *Tag B* with fixed *W* and (d) *Tag B* with fixed *L*.

The read distance of the proposed tag antenna is also tested using different metallic household products, which are different in width, length, and height, as shown in Figure 3.17. Since they are randomly purchased from a department store, the material properties of these metallic containers are unknown. In the measurement process, the tag is attached to two different places, either on the container base or on the container body, as shown in Figures 3.17(a) and 3.17(b), and the corresponding read distances are measured in the boresight ($\theta = 0°$) direction. The results shown in Figures 3.18(a) and 3.18(b). Again, the tag resonance frequencies of the two tag antennas are very stable, and they are not affected much by the backing metallic objects. The minimum read distances for *Tag A* and *Tag B* are 7.5 m and 6 m, respectively.
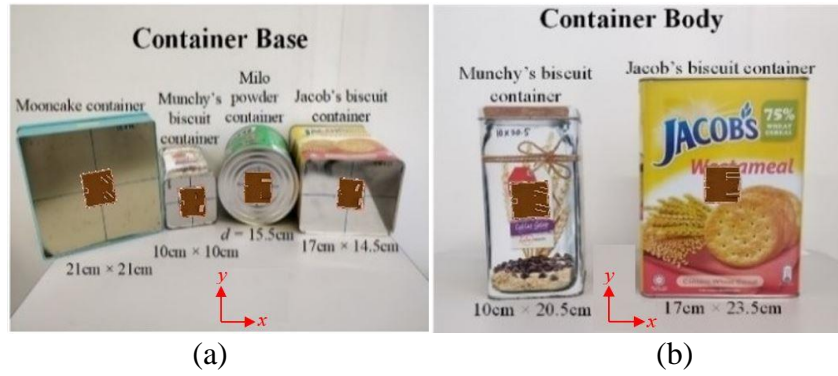
Figure 3.17. Different metallic containers (a) with the tag antenna attached to the base, (b) with the tag antenna attached to the body.
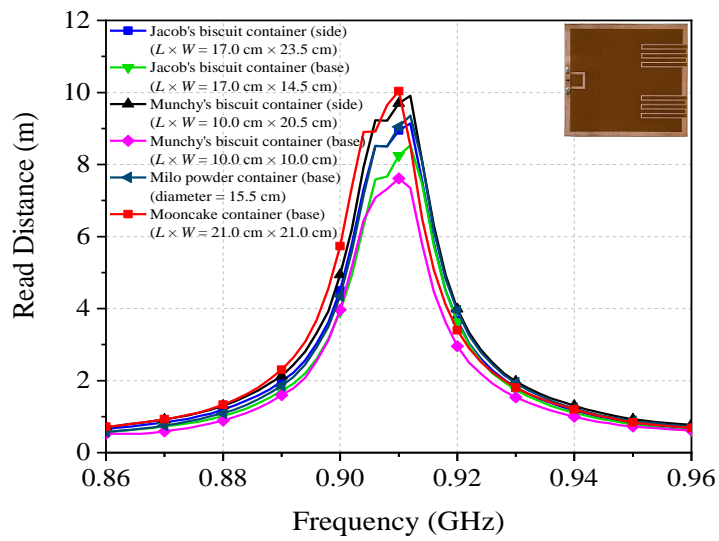
(a)
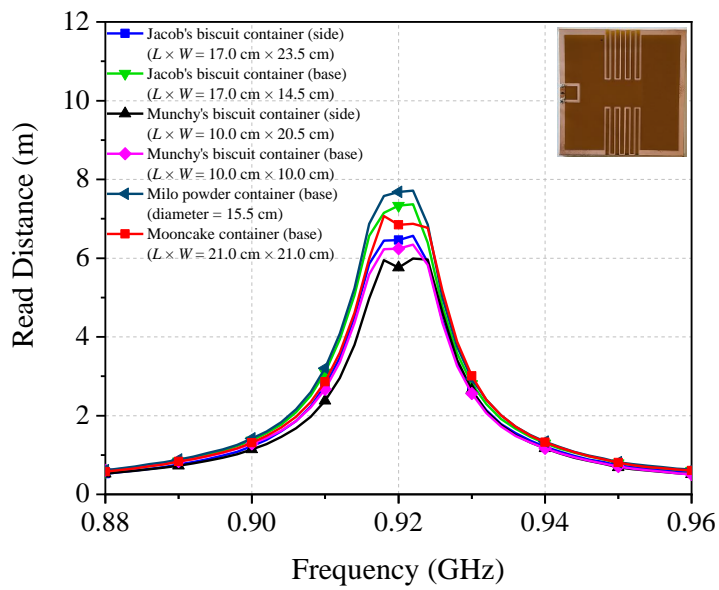
(b)

Figure 3.18. Measured read distances for different metallic containers, (a) *Tag A*, (b) *Tag B*.

Table 3.1. Comparison with the state-of-the-art mountable tag antennas.

Ref.	Tag Dimension (mm³)	Power (EIRP)	Max. Realized Gain (dBi)	Shorting Elements	Chip sensitivity (dBm)	Flexibility	Frequency (MHz)	Max. Read Distance (m)
This work	50 × 50 × 3.318	4 W	-5.4	None	-20.58	Yes (Foam, PET)	915	9.0
(Zuffanelli et al., 2017)	45 × 45 × 1.27	4 W	-4.0	Vias	-17	No (RO3010)	923	6.8
(Zhang and Long, 2014)	26 × 14 × 2.4	4 W	-1.4	Vias	-15.0	No (FR4)	923	5.5
(Bong et al., 2017)	30 × 30 × 3	4 W	-5.2	Stubs	-17.8	Yes (Foam, PET)	915	7.2
(Sohrab et al., 2017)	86 × 41 × 3.2	4 W	-	Stubs	-19.5	No (FR4)	865	5.6
(Lee et al., 2020)	38 × 38 × 1.6	4 W	-6.8	Stubs	-17.8	Yes (Foam, PET)	915	5.3
(Nguyen et al., 2020)	30 × 30 × 3	4 W	0.3 dB (Gain)	Stubs	-22.9	No (FR4)	915	6.4

The proposed tag antenna is also compared with other contemporary metal-mountable tags in terms of size, gain, frequency, read distance, and other parameters in Table 3.1. A complementary split-ring resonator was explored for designing a low-profile on-metal UHF RFID tag in (Zuffanelli et al., 2017). However, the antenna structure requires the use of 28 vias for implementation. A compact double-layered tag antenna (Zhang and Long, 2014) was designed by integrating a dual-element planar-inverted-F antenna with a high impedance surface, but the fabrication process was much tedious as it had involved four inter-layers metallic vias. The soft folded patch in (Bong et al., 2017) was serrated for tuning the tag resonance frequency, but a high-inductance loop-shaped matching stub, which was complex in shape, was required for introducing sufficient reactance. A hybrid tag antenna that would require a four-port microchip was proposed in (Sohrab et al., 2017) for application on both the metal and non-metal platforms, but it was realized using a large footprint that could become impractical for many actual

applications. The tag in (Lee et al., 2020) had employed a magnetic loop antenna for generating an omni-directional radiation pattern, however, the antenna structure required the use of two shorting stubs. A compact C-shaped patch was proposed for metal-mountable applications in (Nguyen et al., 2020), however, the antenna structure was made on a rigid substrate, and it was not flexible. On the other hand, our newly proposed compact tag antenna can be made merely on a single layer, and it does not involve any metallic vias and shorting stubs, making the antenna very simple. Our tag antenna is conformable as it is made using the flexible PET and the soft foam material.

3.6   Summary

Distributed inductors, which are made of high-impedance lines, have been integrated with a ring resonator for designing two metal-mountable tag antennas for on-metal applications. Miniaturization of the antenna footprint is done through the incorporation of the distributed inductors. The high-inductive nature of the distributed inductor has caused the antenna resistance of the ring resonator to increase so that it can achieve a conjugate match with the microchip. Transmission line models have been constructed for designing the proposed tag antennas accurately. The tag antenna radiation is broadside in nature, and it mainly distributes in the upper half plane. The maximum read distance in the boresight is found to be 9 m. The proposed tag antennas are compact in size, single-layered structure, low in complexity, slightly flexible and low in profile. It should be mentioned that the tag resonance frequency is also very stable, and it is not affected much by changes in the backing metallic object.

CHAPTER 4

COMPLEMENTARILY COUPLED C-SHAPED MICROSTRIP PATCHES WITH WIDE-RANGE FREQUENCY TUNING CAPABILITY

4.1 Introduction

In the previous chapter, the distributed inductors were integrated with a ring resonator made of high-impedance lines to design two metal-mountable tag antennas for on-metal applications. However, the ring resonator does not allow frequency tuning over a wide range. It was shown that engaging an external lumped inductor in the tag design (Chiang et al., 2022) for a broad-range frequency tuning was possible. The tag antenna, on the other hand, has a two-layer structure with shorting stubs and a lumped inductor for broad-range frequency tuning. In this project, a single-layer patch antenna, which is constructed using two complementarily placed C-shaped patches, has been proposed for designing a metal-mountable tag with a wide range of frequency tuning capabilities. The two patches are closely coupled to generate sufficient antenna reactance, which is employed as a tuning mechanism. With only the employment of this tuning mechanism, the tag's resonance frequency can be successfully tuned over a broad range covering 920 MHz - 1.18 GHz without using any other external lumped components, shorting stubs, or vias.

4.2   Antenna Configuration and Design Analysis

4.2.1   Tag Antenna Configuration

Figure 4.1 depicts the tag antenna's configuration. The tag design process is usually begun by specifying the component size. This tag here is to fit within a footprint of 50 mm × 50 mm with a profile of ~ 3.3 mm. The antenna inlay contains a top radiator ($w \times l$), which consists of two C-shaped patches as well as a bottom ground, both of which are etched out of a thin layer of copper (0.009 mm thickness) on a thin single-layer polyimide substrate (0.05 mm thickness). The polyimide substrate is selected due to its flexibility, and this feature is important to make our tag conformable. Such substrate is economical and broadly adopted by the RFID industry. With reference to the figure, the larger C-shaped patch is embracing a smaller one for the formation of a complementary structure. The chip used in this design is a UCODE 8 flip-chip with a read sensitivity of −20.85 dBm and an input impedance of 13 − j191 Ω at 915 MHz. As can be seen from the figure, a square-shaped ($w \times l$) flexible foam, with $\varepsilon_r = 1.03$ (permittivity) and tan $\delta = 0.0001$ (loss tangent), is inserted in between the radiator and the ground for isolating them. The flexible foam has a thickness of $h_s = 3.2$ mm. As illustrated in the side view of Figure 4.1, the ground and the top radiator are physically attached to the bottom and top surfaces of the foam, respectively, using double-sided tapes. Obviously, the function of the foam is not only an insulator that separates the bottom ground patch from the top radiator, but also providing structural support to

keep the tag in its form. As seen in the top-down view of Figure 4.1, a small gap (0.15 mm) is set aside on the inner C-shaped radiator for bonding the RFID microchip. The tag antenna's input port is connected to the chip's two bonding pads, which are named as RF+ and RF−. The microchip itself has a power management circuit (rectifier and voltage regulator) that transforms the harvested RF energy to a DC voltage for powering up its internal circuits. The CST (Computer Simulation Technology) simulation software is utilized for all the coming design and optimization procedures. In the simulation, a 50 Ω discrete port is first applied across the bonding pads (RF+ and RF−). Then, the port is normalized to the complex chip impedance using the software's post-processing method. All the detailed geometrical parameters of the proposed tag, which is constructed to operate in the USA UHF RFID passband, are given in Table 4.1.

Table 4.1. The proposed tag antenna's optimized design parameters.

Design Parameter	Value (mm)	Design Parameter	Value (mm)
w	50	i_2	10
l	50	i_3	6
h	3.318	i_4	1
h_s	3.2	i_5	0.5
i_1	11	-	-
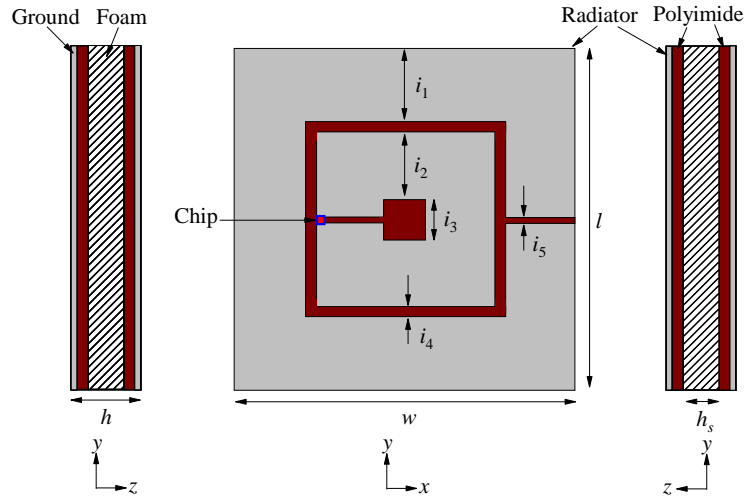
Figure 4.1. Proposed tag antenna configuration with side and top views.

4.2.2 Antenna Design Analysis

Antenna design analysis is started by replacing the microchip with an external discrete port which is set to have a complex impedance to represent the real chip impedance $(13 - j191\ \Omega)$. The antenna structure is first analysed by removing the outer C-shaped patch. In this case, the tag resonance frequency is observed to have shifted up to 1.72 GHz with an antenna impedance $(0.59 + j191.75\ \Omega)$, as can be seen in Figure 4.2(a), which goes far outside the regulated UHF passband. However, the realized gain $(-7.875\ \text{dBi})$ and the power transmission coefficient are too low (0.17), as shown in Figure 4.2(b), due to poor impedance matching performance. After adding the outer C-shaped patch, the operating frequency can be shifted back to 923 MHz. A large mutual capacitance can be formed between the two complementary C-shaped patches, and this is important for reducing the tag resonance frequency down to the suitable UHF passband. For the finalized tag design, the antenna's realized gain and impedance are achievable as $-3.72\ \text{dBi}$ and $12.76 + j190.66$

Ω, respectively, as shown in Figure 4.2(a), achieving a good power transmission coefficient of 0.99 (Figure 4.2(b)). At the simulated resonance frequency of 923 MHz, Figure 4.3 shows the simulated surface current distribution on the antenna. High current density is found flowing along the edges of the narrow slot in between the outer and inner patches, showing that it is highly reactive and can be used for tuning the patch antenna's resonance frequency effectively. The currents in the opposite edges along the slot are opposite to each other, which is a salient feature of complimentary coupling mechanism.

(a)

(b)
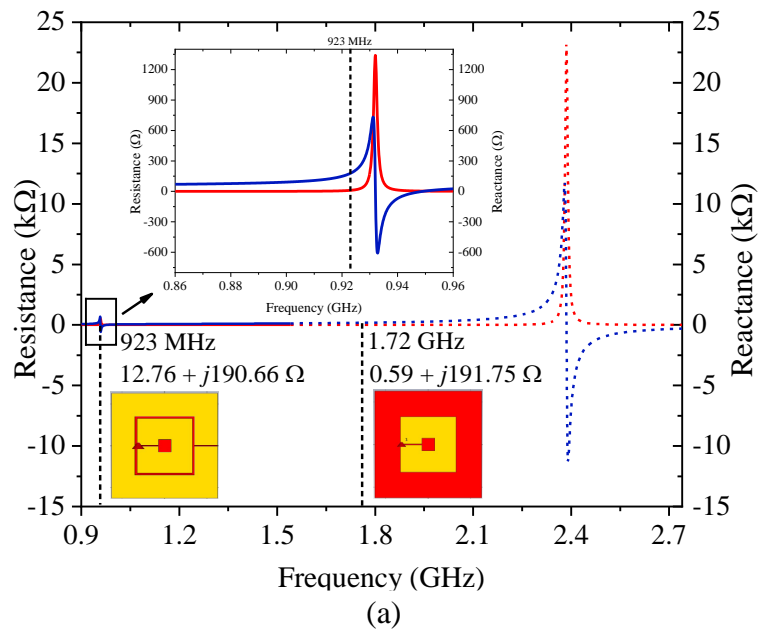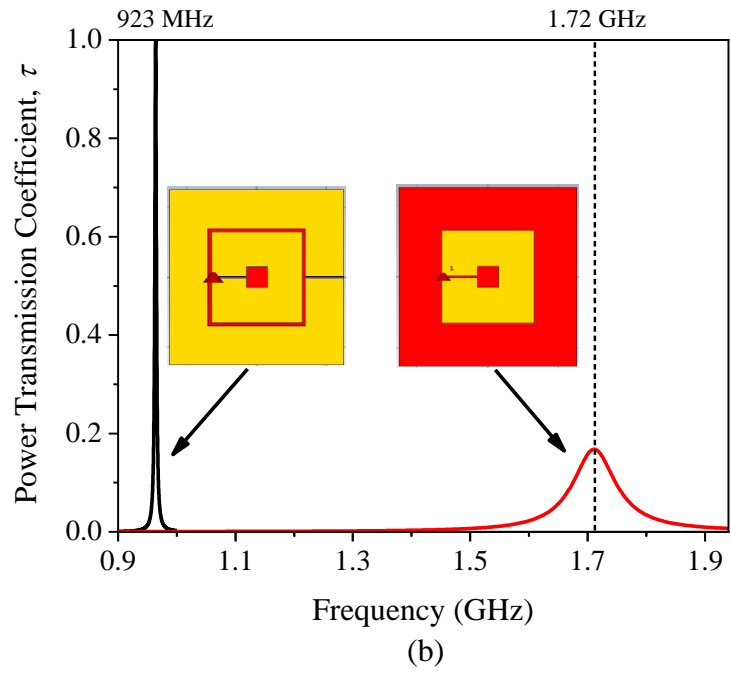
Figure 4.2. Analysis on the antenna structure for the cases with and without the outer C-shaped patch: (a) Impedance. (b) Power transmission coefficient.
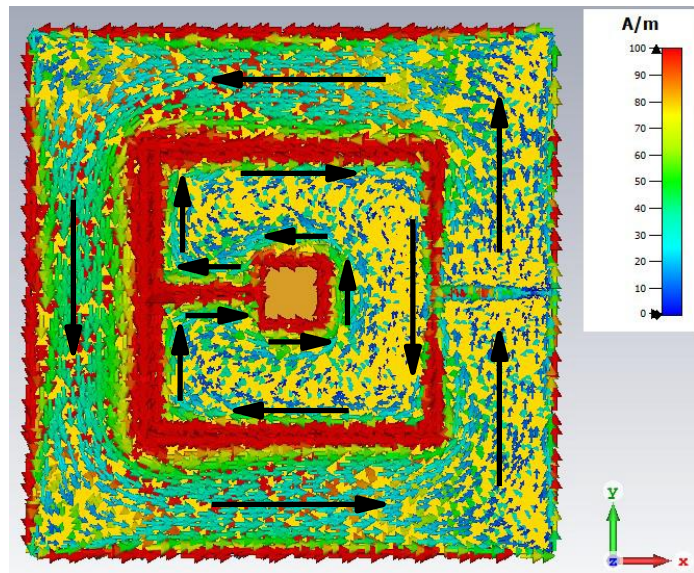
Figure 4.3. Surface currents for the antenna structure.

4.2.3 Transmission Line Model

A transmission line model (TLM), as shown in Figure 4.4(a), has been constructed for characterizing the antenna performance. The model can be

fully established by using multiple segments of transmission lines, without involving any lumped elements. Now, the modeling process is further elaborated. The 2D Circuit Simulator, which is a two-dimensional circuit solver provided by the CST Microwave Studio Suite, has been employed for building the TLM. First, the microstrip stripline model is selected in the "Substrate Settings", where all the required parameters such as substrate dielectric constant, conductor thickness, number of layers, and ground plate thickness are all properly configured in the reference block, as shown in Figure 4.4(b). Then, the model is established by dividing the antenna into 6 segments of stripline couplers, and they are interconnected by multiple stripline bends for better representing the actual antenna structure. Mutual capacitance effect that is formed between the two complementary C-shaped patches can be easily taken care by adjusting the separation gap of the coupled lines. With reference to the figure, a stripline gap is employed for describing the gap in the outer C patch, while a complex port is used for representing the chip. This model is then simulated using the 2D Circuit Simulator for generating the antenna impedance. Use of the circuit simulator for designing and tuning a tag antenna is substantially faster than using the full-wave simulator as the former takes considerably less computer resources. For example, a full-wave simulation of the proposed tag antenna can take up to 20 minutes, but the TLM simulation can be completed in 2 seconds. The TLM is not only useful for understanding the circuit characteristics, but it can also be employed for analysing the design parameters effectively. However, it is not able to capture the radiation effect as what a full-wave simulator does. The TLM also cannot simulate the diffraction of the backing metal plate. Both the

TLM-generated resistances and reactances are compared with those generated by the CST full-wave simulation in Figure 4.5, both of which are showing reasonably good agreement. Then, the microchip is removed for measuring the antenna impedance. The solder pads across the antenna port are accessed by a custom-made differential probe station, which is then connected to a vector network analyser. The modeled impedance is found to be agreeing reasonably well with that for measurement, as observed in Figure 4.5. For ease of comparison, in the same figure, the conjugate chip impedance is also supplemented. The TLM antenna impedance reads $16.21 + j184.82$ Ω at the tag resonance frequency of 919 MHz, which is quite close to the CST-simulated case of ($12.76 + j190.66$ Ω) at 923 MHz. Both are not far away from the measured impedance of ($10.56 + j181.54$ Ω) at 918 MHz. The antenna impedance is achieving almost a conjugate matching level with the chip impedance ($13 - j191$ Ω).

(a)

Stripline Coupler

Stripline Bend

Substrate Settings

Complex Port (Chip)

Stripline Gap

(b)
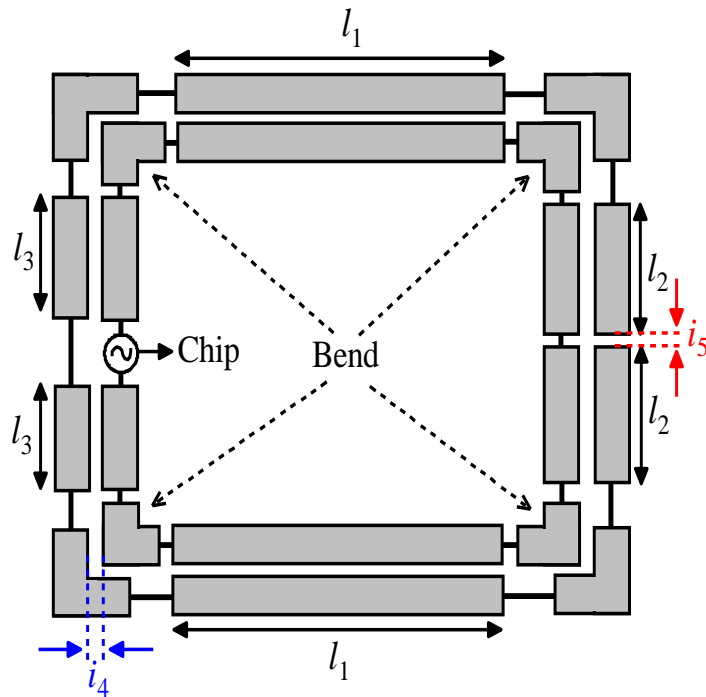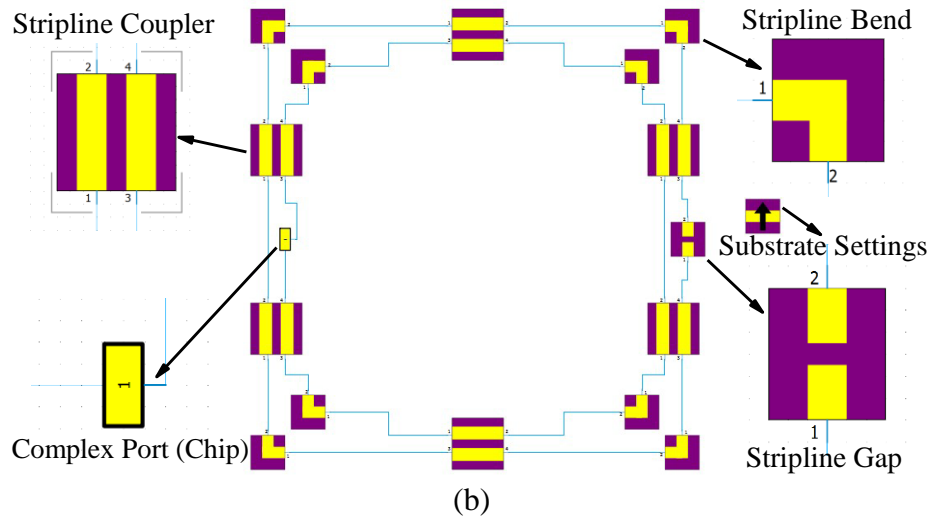
Figure 4.4. (a) The TLM model for the proposed tag antenna. ($l_1 = 50$ mm, $l_2 = 24.75$ mm, $l_3 = 24.85$ mm, $i_4 = 1$ mm, $i_5 = 0.5$ mm). (b) Transmission Line Model (TLM) established by the Circuit Simulator.
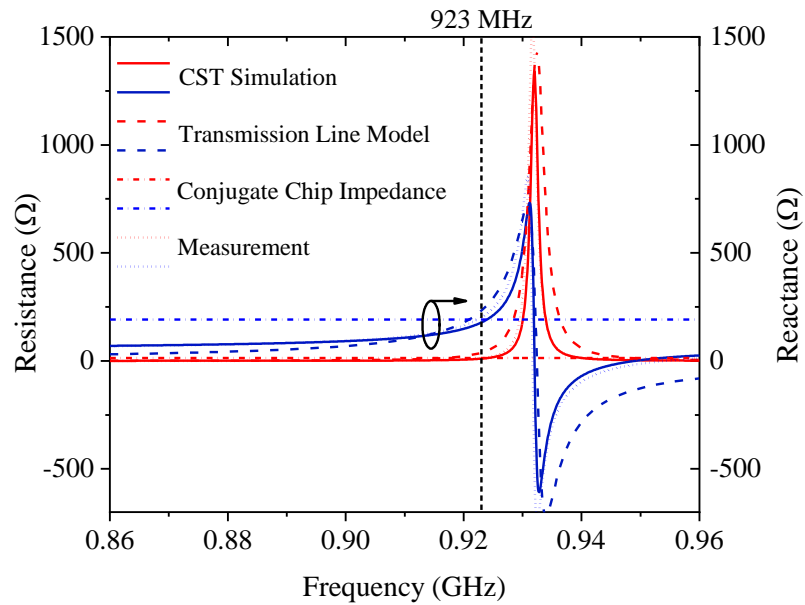
Figure 4.5. Antenna impedances generated by the CST full-wave simulation, transmission line model, and measurement.

4.3   Parametric Analysis

A parametric analysis is performed here for understanding the effects of the important design parameters. This task can obviously be done either with the employment of CST or TLM. The analysis is started by varying the gap (i_5) of the outer C-shaped patch as it is a crucial design parameter. It has been found that the resonance frequency of the tag antenna can be efficiently changed by altering the gap space i_5 without compromising the tag's performance. When the gap becomes larger, the coupled capacitance reduces due to the decrease of coupling edges, which has in turn raised the tag resonance frequency. The tag can be easily tuned to cover the entire UHF RFID spectrum (860 MHz to 960 MHz). To perform the frequency tuning, first, the parameter i_4 is adjusted to place the tag resonance frequency at ~ 860 MHz. Then, the parameter i_5 is slowly increased by a step size of 1 mm to slowly move it up, with ~ 13 MHz per step, to ~ 960 MHz, as can be observed in Figure 4.6(a). For all cases, with reference to Figure 4.6(b), the power transmission coefficient can be kept ~ 99 %. It is observed in Figure 4.6(c) that increases are seen in both the realized gain and radiation efficiency when the slot width i_5 becomes larger. This is reasonable as the frequency increase has caused the tag size to become electrically larger. The realized gain and radiation efficiency are in the ranges of –6 dB - –1 dB and 0.19 - 0.23, respectively, which are reasonable as the tag size is electrically small (Moh et al., 2018). Figures 4.7(a) and 4.8(a) show the CST full-wave simulated antenna impedance ($Z_{ant} = R_{ant} + j\ X_{ant}$) and power transmission coefficient for changing the parameter i_5 in the range of 0.5 mm to 30 mm. To demonstrate its design and simulation capability, the

corresponding TLM-generated Z_{ant} and τ are also included in Figures 4.7(b) and 4.8(b) for comparison. The TLM model is found to be able to estimate the tag resonances as good as the full-wave simulation model. However, there is a slight discrepancy in the respective peak values, for both the Z_{ant} and τ. This is due to the omission of radiation and diffraction effects, as mentioned earlier. Despite the difference, the TLM can still serve as a useful tool for characterizing the tag characteristic quickly in the early stage. After obtaining the initial design, the full-wave simulator can later be used for further optimization. With reference to the figures, the tag antenna's resonance frequency rises from 920 MHz to 1.18 GHz at a rate of 70 MHz when i_5 is increased from 0.5 mm to 30 mm at a 5 mm interval. As can be seen in Figures 4.8(a) and 4.8(b), the power transmission coefficient for all cases can be maintained at least 90%. Obviously, this parameter is helpful for tuning the tag resonance frequency in a very wide range without sacrificing τ. To have a higher accuracy, for the subsequently analysis, the CST full-wave method will be used instead. The effect of the coupling gap (i_4) between the inner and outer C-shaped patches is next investigated. As seen in Figures 4.9(a) and 4.9(b), raising i_4 from 0.6 to 1.4 mm leads the tag's resonance frequency to drop down, while retaining $\tau \sim 99\%$. However, this parameter only allows a fine tunability in the range of 910 - 940 MHz. With reference to Figure 4.9(c), decreasing i_4 causes the realized gain to increase, but it does not affect the radiation efficiency much. Subsequently, the dimension (i_3) of the internal square slot is studied, as shown in Figures 4.10(a) and 4.10(b). Increasing i_3 decreases the tag resonance frequency, although keeping a τ more than 90%.

The resonance frequency of the tag is observed to decrease at a rate of 7.5 MHz with each 1.0 mm increment in i_3. As the value is increased, as shown in Figure 4.10(b), the antenna becomes more resistive and inductive as the line width (i_2) has become narrower. The tag's realized gain increases when i_3 is decreased, as shown in Figure 4.10(c), and the radiation efficiency changes from 0.18 to 0.21 when i_3 is varied.

(a)

(b)

(c)
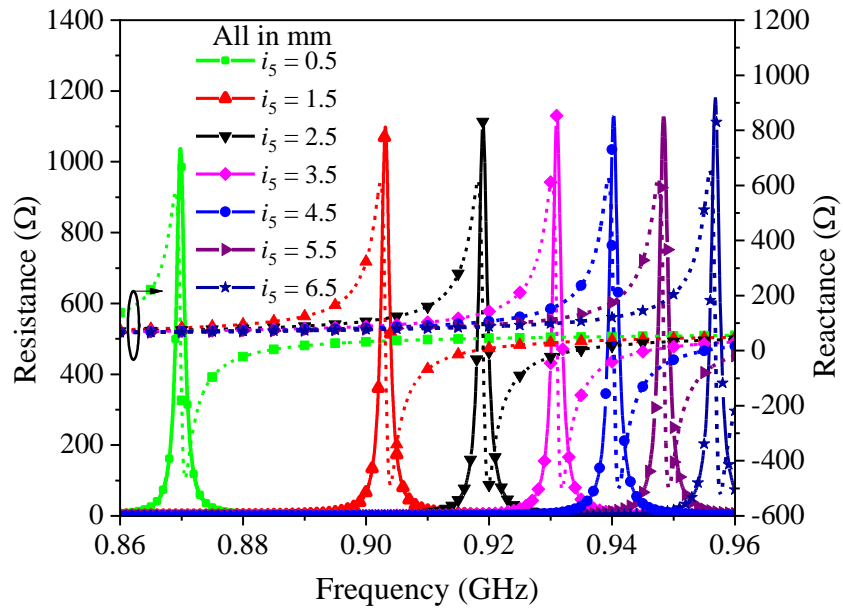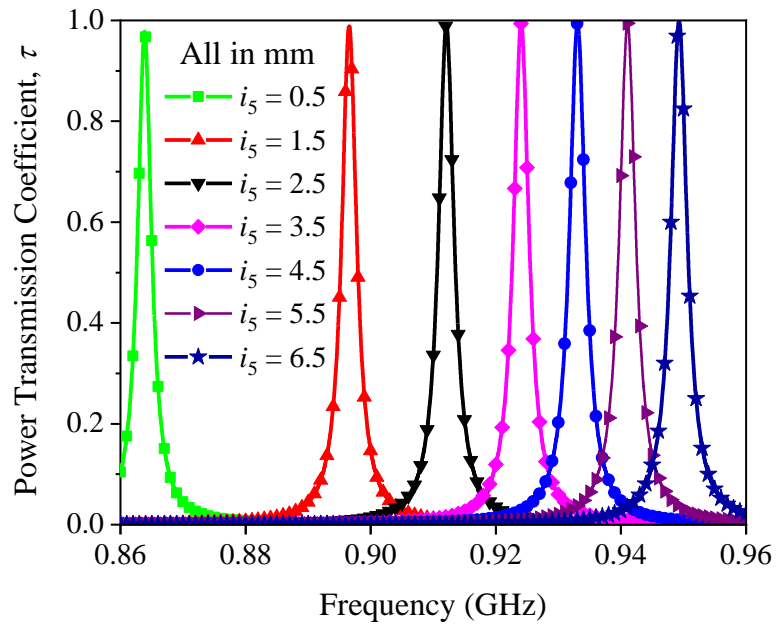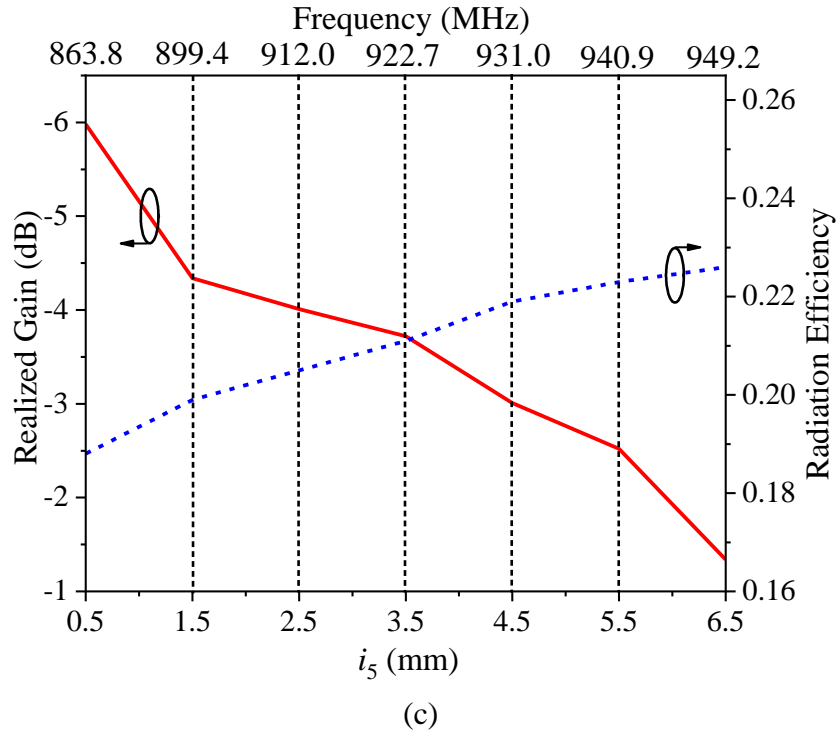
Figure 4.6. (a) Antenna impedance and (b) power transmission coefficient for changing the parameter i_5, and (c) realized gain and radiation efficiency.

(a)
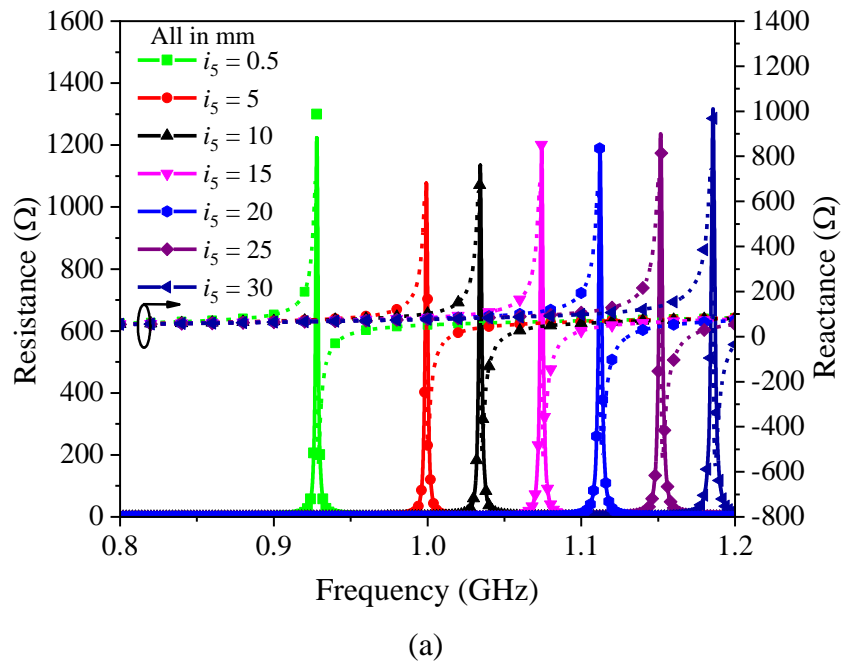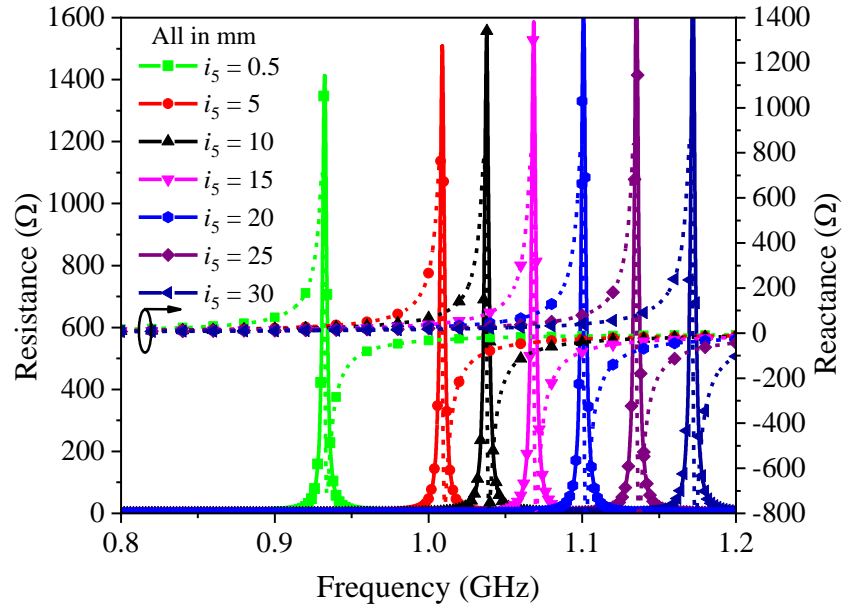
Figure 4.7. Comparison of the (a) CST-full-wave simulated and (b) TLM-modeled antenna impedances for changing the parameter i_5.
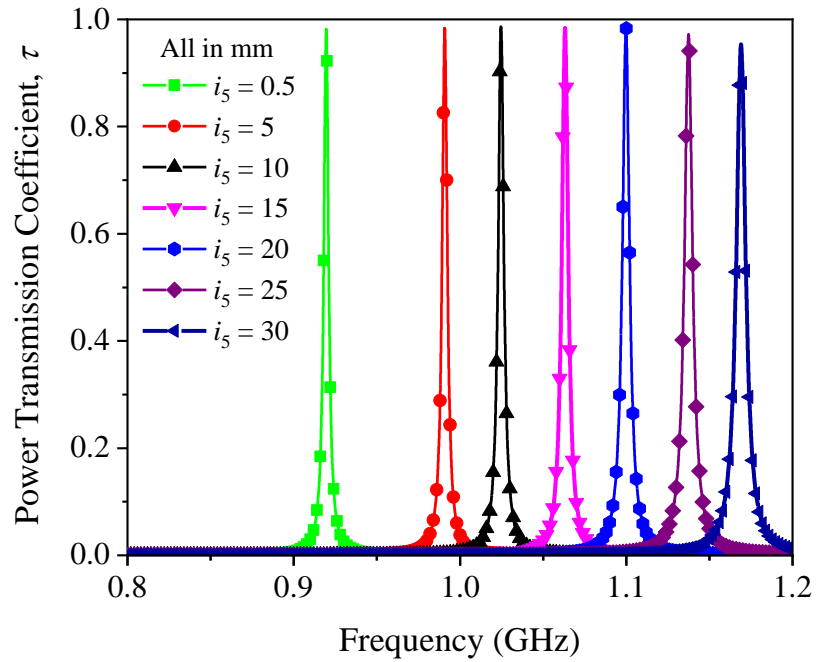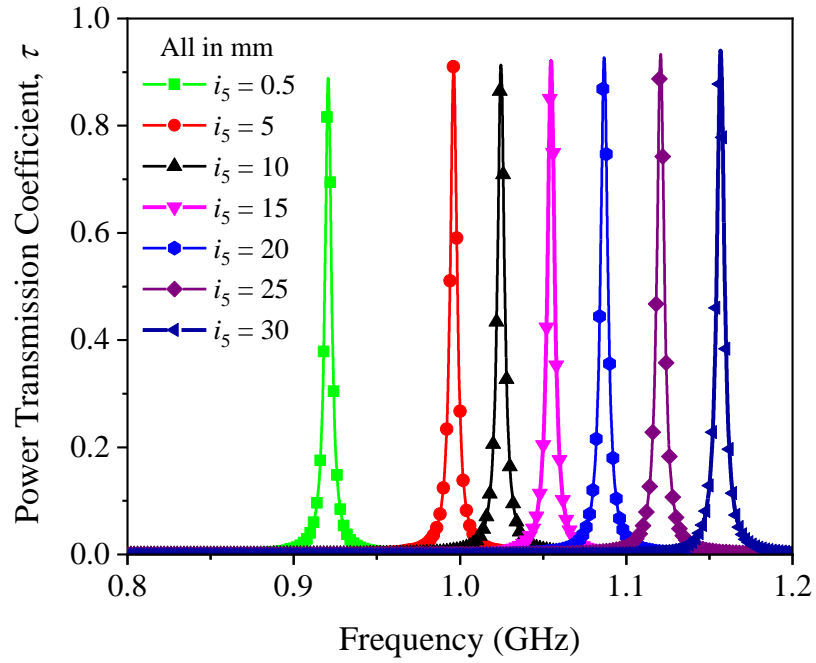
(b)

Figure 4.8. Comparison of power transmission coefficients for cases of (a) CST full-wave simulation and (b) TLM modeling for changing the design parameter i_5.
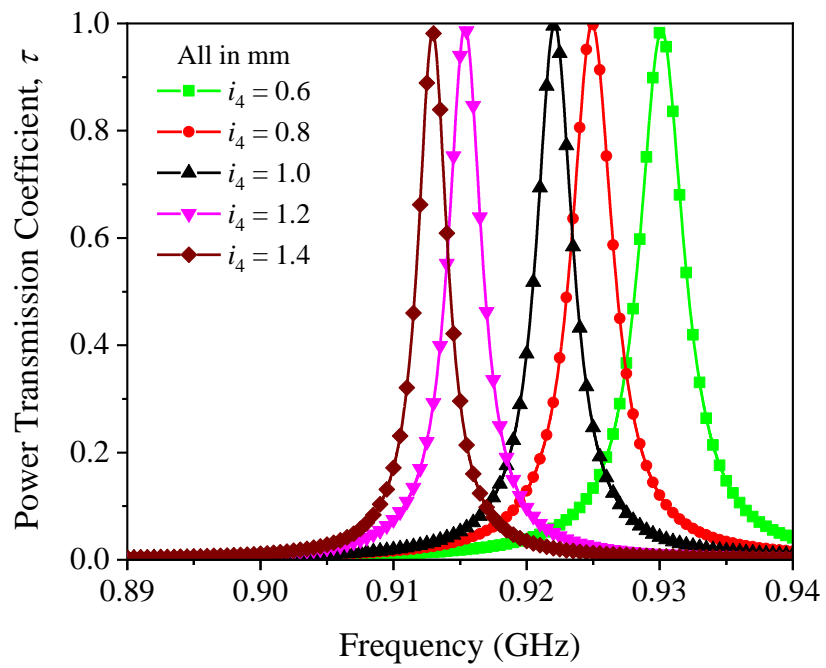
(a)
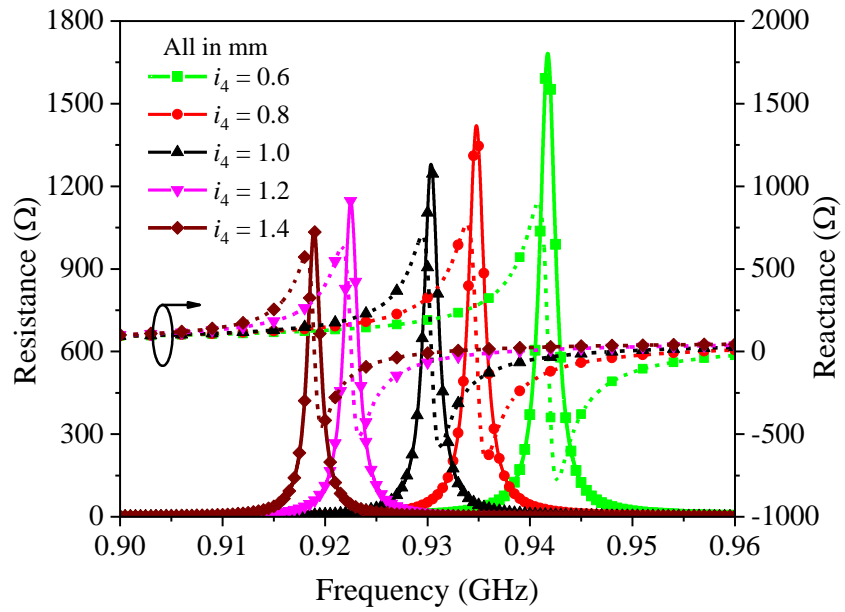
(b)
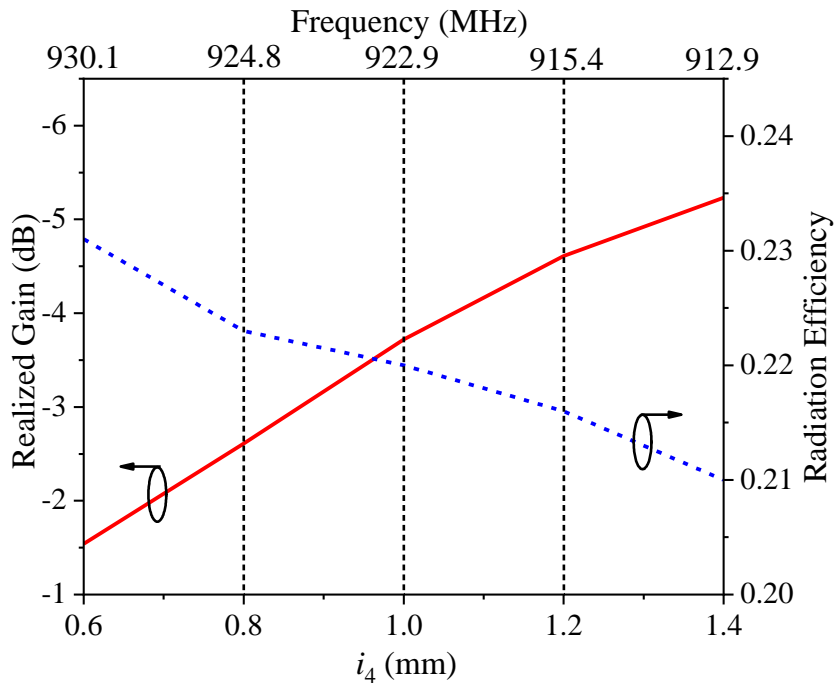
(c)

Figure 4.9. Effect of changing the separation gap (i_4) on (a) τ (b) Z_{ant} and (c) realized gain and radiation efficiency.

(a)

(b)

(c)
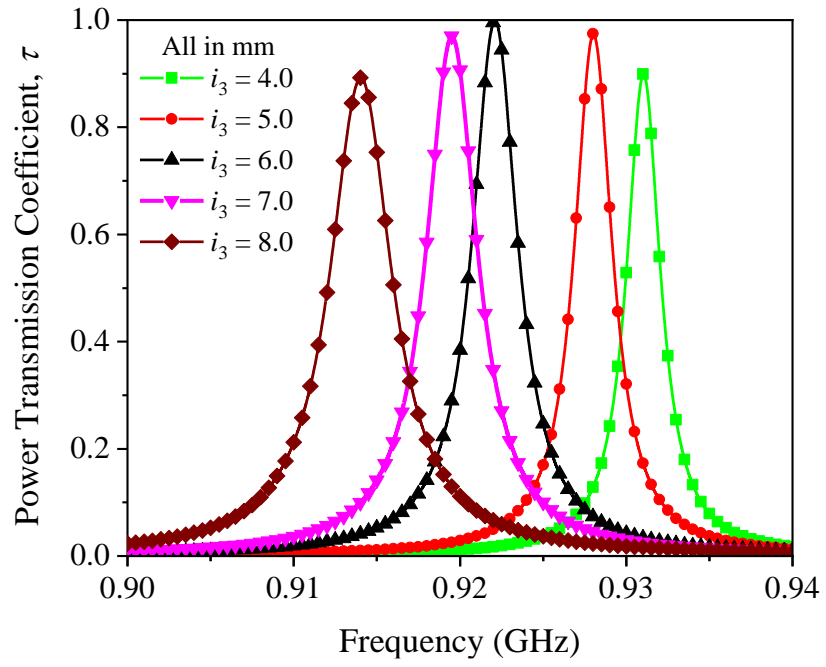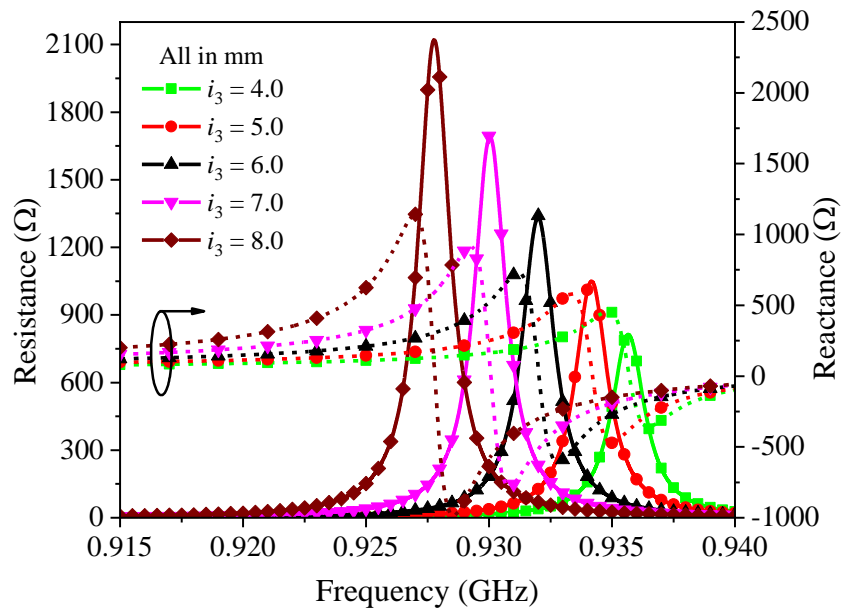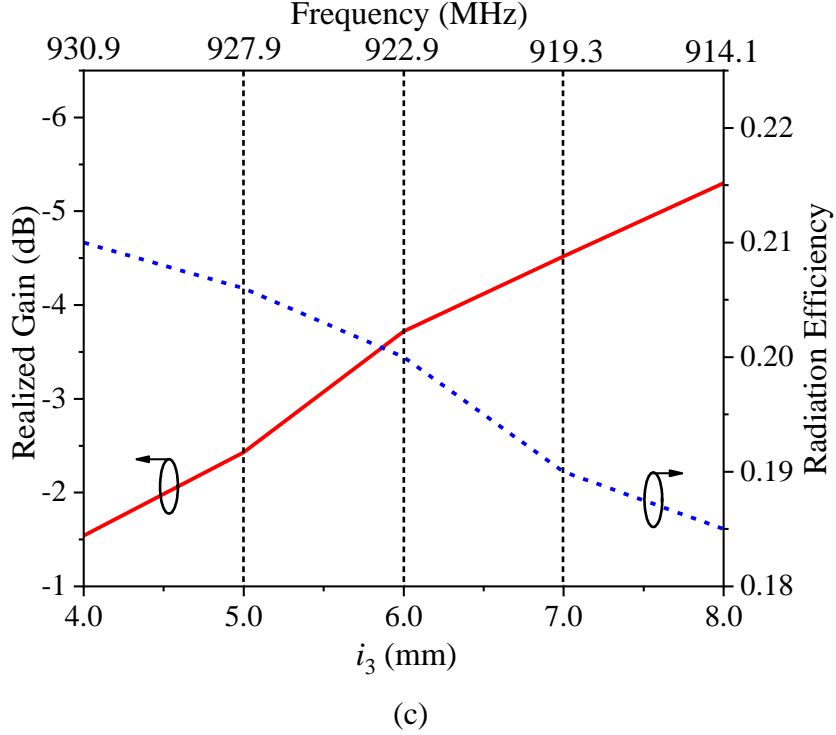
Figure 4.10. Effect of changing i_3 on (a) τ (b) Z_{ant} and (c) realized gain and radiation efficiency.

4.4   Measurement Setup

The Voyantic TAGFORMANCE Measurement System was employed for characterizing the tag's performances inside an anechoic chamber. In all the measurements, the prototype is placed at the middle of a 20 cm × 20 cm aluminum plate, which is held in place by a Styrofoam with $\varepsilon_r = 1$ as shown in Figure 4.11(b). The tag antenna is always positioned around the middle of the cabinet. Figures 4.11(a) and 4.11(b) show the fabricated prototype and the measurement setup, respectively. A reader with a linearly polarized antenna (8 dBi Gain) is employed for testing the proposed tag. The reader antenna is maintained at a constant length (52 cm) from the tag being measured along the z axis. The realized gain is $G_r = P_c / (L_l P_t)$, where P_c is the read sensitivity of

the Ucode8 microchip (–20.85 dBm), P_t is the reader threshold range at a certain frequency during the threshold power sweep, and L_l is the obtained forward-link losses (cable loss and path loss). In the threshold measurement, the chip sensitivity can be calculated by $P_c = P_{tag} \times G$, where $G = G_{tag} \times \tau$. Both P_{tag} and G are derived from Friis transmission equation fundamentally (Colella et al., 2016). It can be seen that P_{tag} has taken account of the tag sensitivity and channel losses while G has considered the tag's antenna gain as well as the efficiency of power transfer. Figure 4.12 depicts the measured and simulated realized gains of the proposed tag antenna. The highest realized gain is measured to be –5.18 dBi at 920 MHz, with reasonable agreement seen between the simulation and measurement data.

| (a) | (b) |
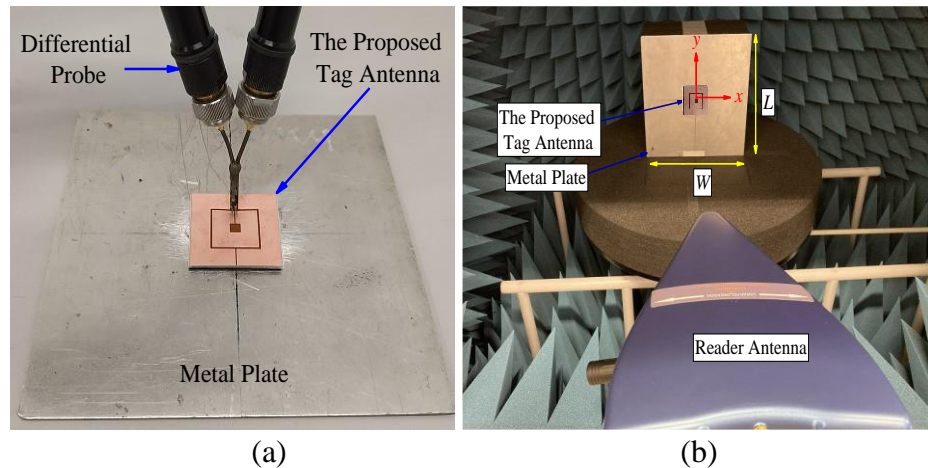
Figure 4.11. (a) Aluminum plate with the tag attached at the middle for measuring antenna impedance using a differential probe. (b) The anechoic cabin with the measurement setup.
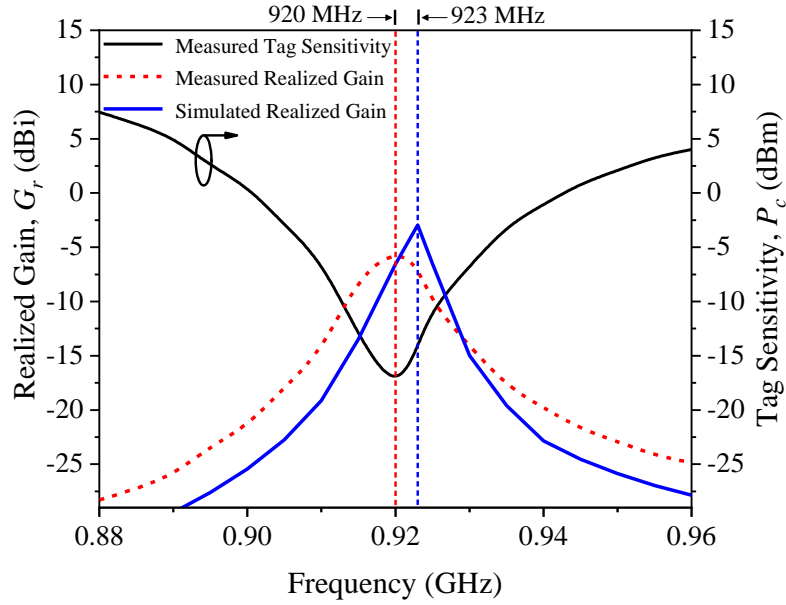
Figure 4.12. Measured and simulated realized gains of the proposed tag antenna when it is attached to a 20 cm × 20 cm metal plate.

4.5 Experimental Results and Discussion

One of the most crucial RFID characterizations is to evaluate the tag antenna's read distance. The TAGFORMANCE system, with 4 W EIRP, has been utilized for all the measurements. The reader antenna is set at a constant distance in the experiment, while the tag is positioned at the center on an aluminium plate and rotated to measure its reading patterns. Figures 4.13(a) and 4.13(b) illustrate the measured read patterns in the *xz*, *yz*, and *xy* planes at the tag resonance frequency of 920 MHz. Broadside characteristic has been observed in the *xz* and *yz* plane read patterns in Figure 4.13(a), yielding maximum radiation in the boresight direction (θ = 0°). The backing metal plate has improved the front-to-back ratio. The boresight's maximum read distance is found to be 9 m in this case. The maximum read distances in the *xy*

plane are found at $\phi = 0°$ and $\phi = 180°$, indicating that the tag is linearly polarized.
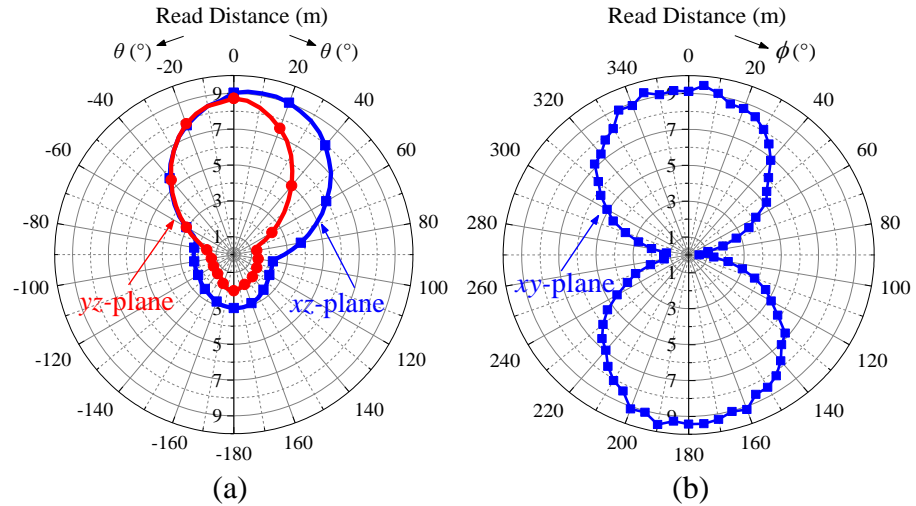
Figure 4.13. Measured read distance in the (a) *xz* and *yz* plane and (b) *xy* plane.

The proposed tag antenna is tested on a couple of aluminum plates with different sizes ($W \times L$), all with a thickness of ~5 mm, as the tag antenna is intended to be mounted on metal surfaces. The tag prototype was always positioned around the center point of the plate during the experiment. For measurement here, the maximum read distances are acquired in the boresight ($\theta = 0°$). When W is fixed to 20 cm and L is decreased gradually from 24 cm to 16 cm, the read distance falls from 9 m to 7 m, as shown in Figure 4.14(a). The plate width W is then altered while L is held constant at 20 cm, with the results displayed in Figure 4.14(b). The read distance falls in between 8 m to 9 m. The effects of the plate size on the antenna impedance are studied. With reference to Figures 4.14(c) and 4.14(d), the antenna impedance is not much affected by changes in the width and length of the backing metal plate.
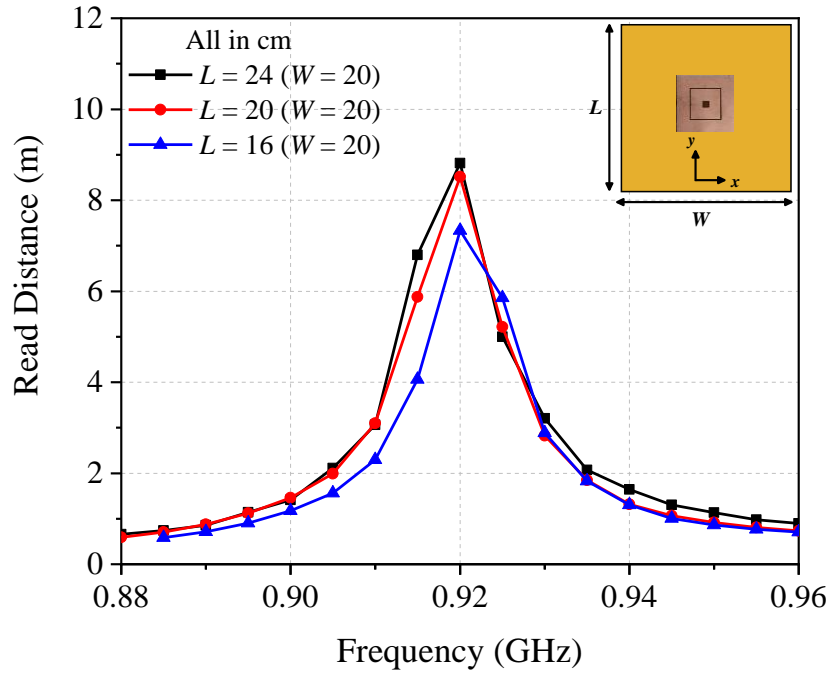
(a)
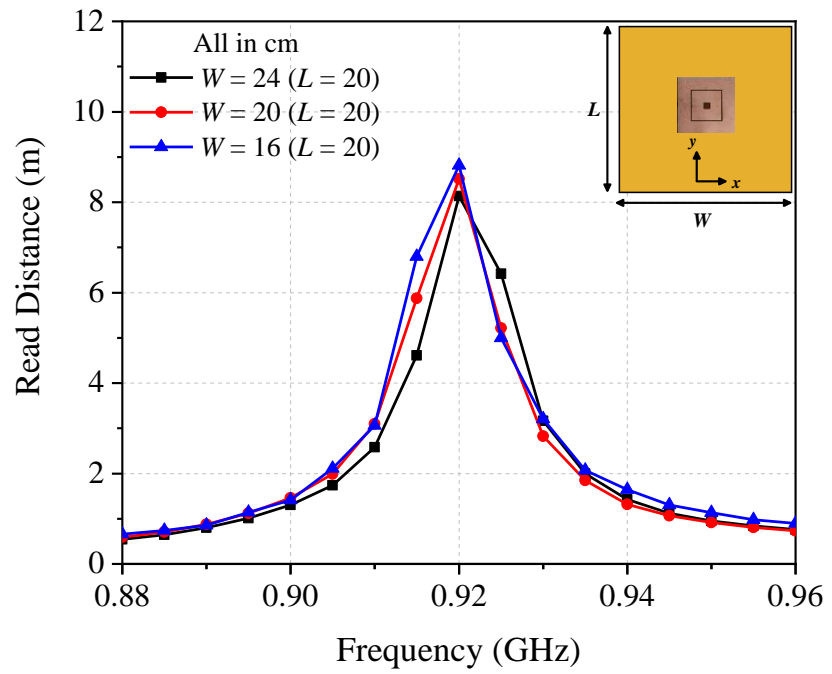
(b)
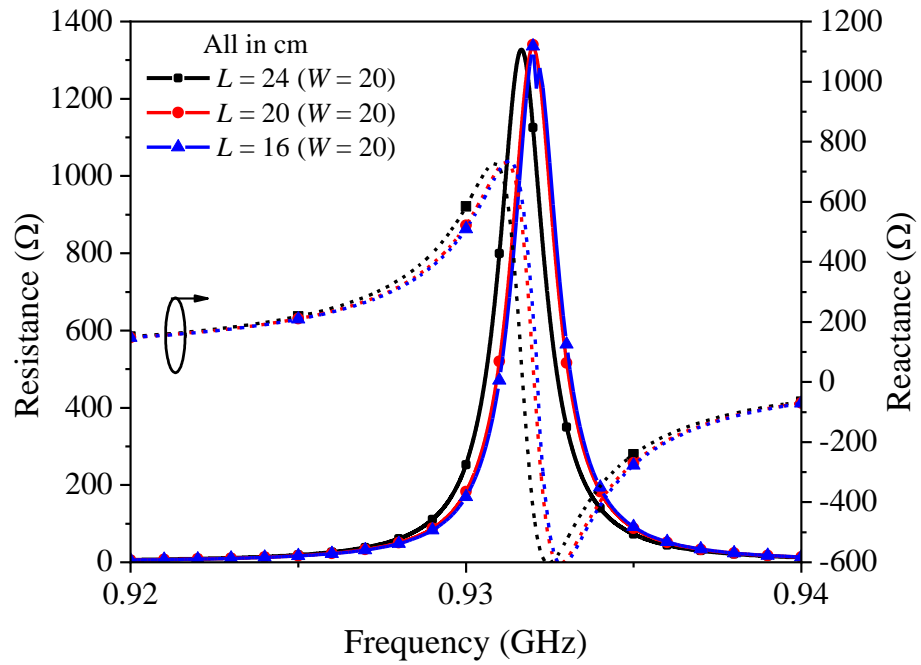
(c)
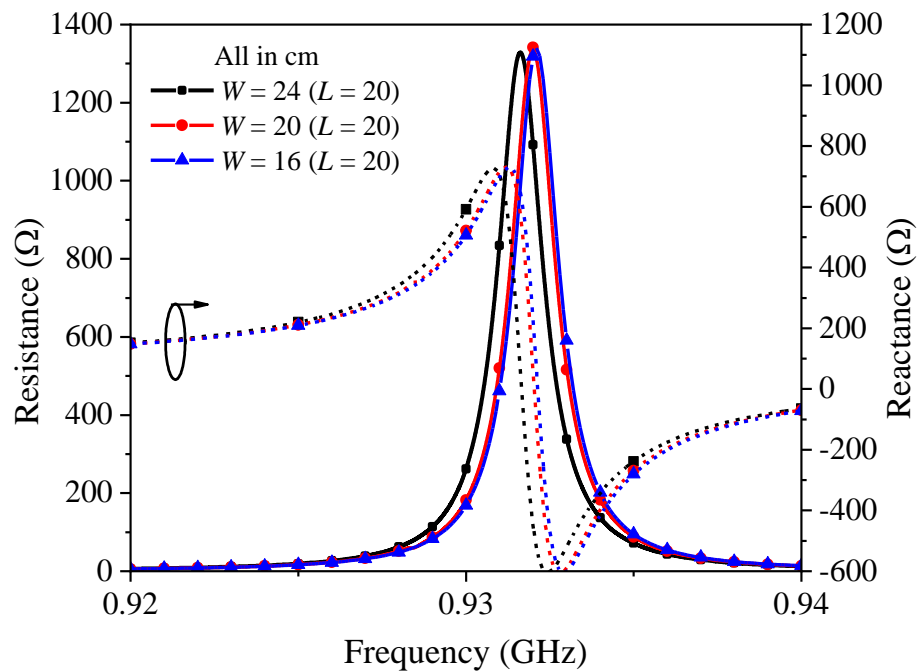
(d)

Figure 4.14. The read performances and impedance characteristics for different plate sizes: (a) Measured read distances for different plate lengths *L*. (b) Measured read distances for different plate widths *W*. (c) Simulated antenna impedances for different plate lengths *L*. (d) Simulated antenna impedances for different plate widths *W*.

The impact of the plate size on the radiation patterns and bandwidth has also been studied using simulations. Figures 4.15(a) - (c) illustrate the simulated radiation patterns in the *xz*, *yz*, and *xy* planes. Broadside characteristic has been observed in the *xz* and *yz* plane radiation patterns in Figures 4.15(a) and 4.15(b), yielding maximum radiation in the boresight direction ($\theta = 0°$). The boresight's maximum realized gain is found to be ~ -3 dBi and not much affected by the plate size. From Figure 4.15(c), the maximum radiation in the *xy* plane is found at $\phi = 0°$ and $\phi = 180°$, indicating that the tag is linearly polarized, and the radiation pattern is not much affected by the plate size. With reference to Figure 4.15(d), the tag antenna's half-power bandwidth was found covering from 922 MHz to 926 MHz and not much affected by variation in the backing metal plate's size.

(a)

(b)

(c)

(d)
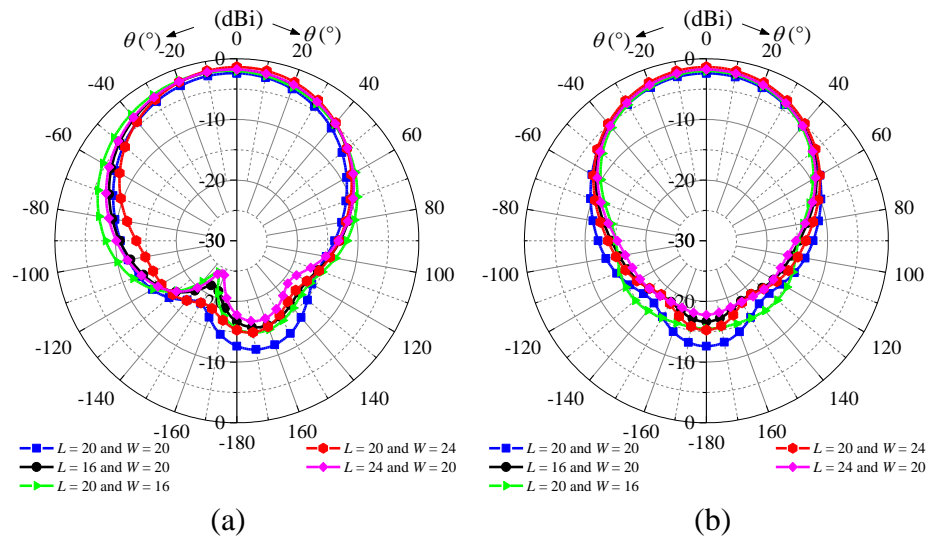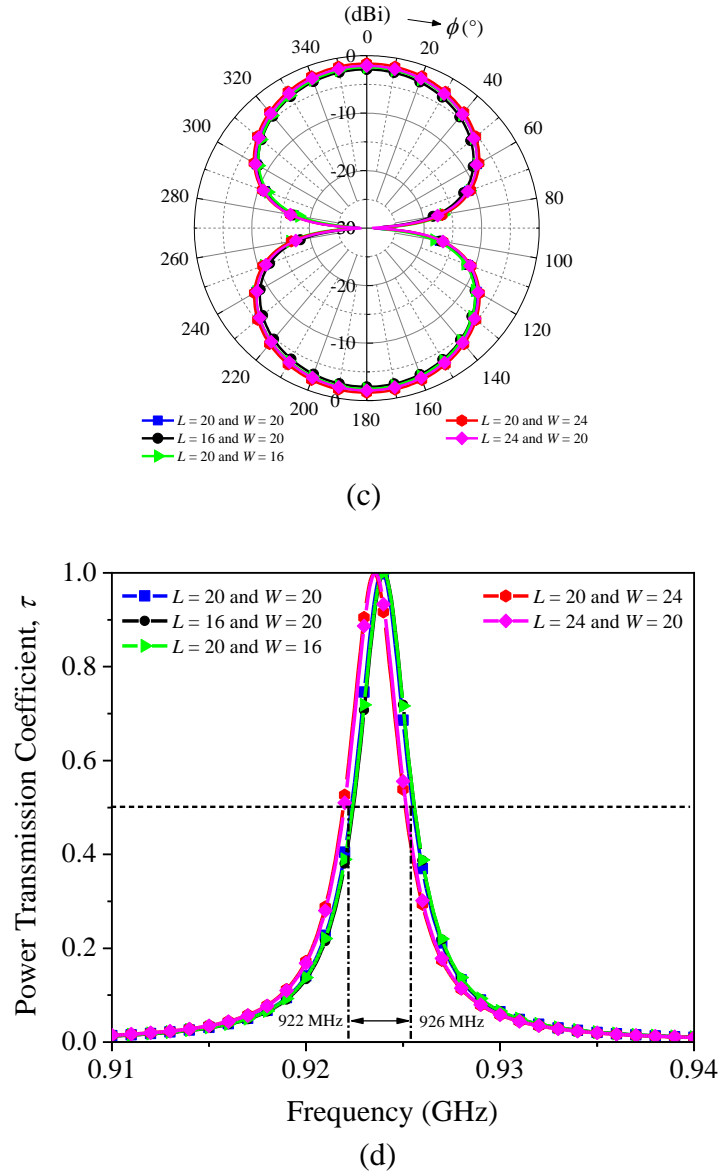
Figure 4.15. Effects of the length *L* and width *W* of the backing metal backing plate on the radiation patterns in the (a) *xz* plane (b) *yz* plane (c) *xy* plane as well as the (d) half-power bandwidth.

To study its practicality, the proposed tag was also tested over several metal boxes that are commonly found in household. To begin, the tag was attached to the base and on the body of the different household items, as displayed in Figures 4.16(a) and 4.16(b), to test their read ranges in the boresight ($\theta = 0°$) direction, with the corresponding measured curves given in Figure 4.17. A read distance in the range of 7 to 9 meters can be achieved. A

smaller surface does cause the read distance to degrade. Despite the metallic household items are made of different dimensions and materials, the tag antenna's resonance frequency can be well controlled around 920 MHz, while maintaining a stable read performance. This is a good feature as the proposed tag is not affected much by changes in its backing object.

(a)   (b)
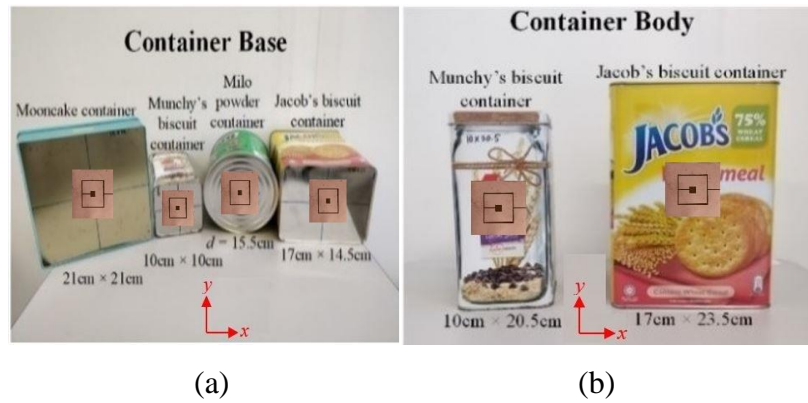
Figure 4.16. Household containers: (a) Attaching the tag on the container base and (b) attaching the tag on the container body.
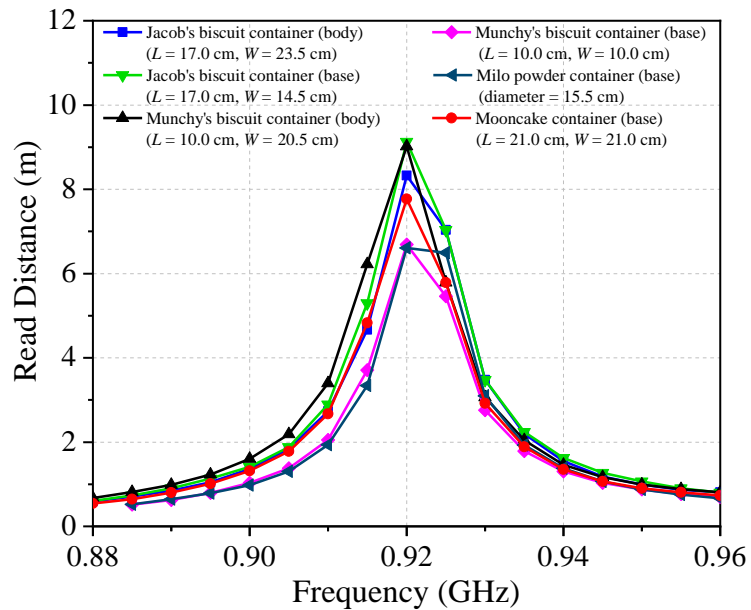
Figure 4.17. Measured read distances for different household containers.

Table 4.2 compares the proposed tag antenna with several previously reported metal-mountable tag antennas. Serrated edges (Bong et al., 2017) were used to fine-tune the tag resonance frequency in a flexible folded patch antenna. However, to provide enough reactance, a high-inductive loop-shaped matching stub was needed, and it was to be placed along the sidewall, making the tag structure very fragile. On the other hand, the reactance mechanism of our tag can be easily implemented within the same surface as the antenna. A hybrid tag antenna (Sohrab et al., 2017) that was designed using a four-port microchip was shown to be applicable on both nonmetal and metal surfaces. However, it was developed to have a huge size, making it unsuitable for many practical applications. Also, the antenna structure was becoming complicated due to the usage of the four-port microchip. In contrast, our tag structure only requires a simple two-port chip. A simple C-shaped tag antenna (Nguyen et al., 2021) was proposed for metal-mountable usage; however, the tag antenna prototype was fabricated using a hard FR4 substrate and was not flexible, where impedance matching can be tuned with the employment of shorting stubs. Different from that in (Nguyen et al., 2021), our antenna is made using a single-layer structure, and it does not require the use of any shorting elements. A dual-element PIFA (Zhang and Long, 2014) was integrated with a high-impedance surface for constructing a small double-layered tag antenna. However, the antenna structure was complicated as it would require the use of 4 metallic layers and multiple vias, which could increase the fabrication complexity and cost significantly. A complementary split-ring resonator was employed for constructing a compact on-metal tag in (Zuffanelli et al., 2017),

however, the antenna itself would need 28 metallic vias. It makes the antenna structure very complicated and increases the manufacturing costs. It was shown that engaging an external lumped inductor in the tag design (Chiang et al., 2022) for a broad-range frequency tuning was possible. The tag antenna, on the other hand, has a two-layer structure with shorting stubs and a lumped inductor for frequency tuning. The C-shaped tag in (Lee et al., 2019) would also require the use of a very narrow shorting stub for generating sufficient reactance. The PIFA in (Inserra and Wen, 2021) has cascaded three lumped inductors in series with its coplanar feedline for tuning its impedance. However, cascading multiple lumped inductances directly with the feedline can cause the tag's read performance to deteriorate. As a result, its achievable read distance is much shorter (3.6 m) than ours. Two compact UHF tag antennas, which consist of a square ring loaded with two distributed inductors, are proposed for on-metal applications (Murugesh et al., 2022). Here, the tag size and read range are the same as ours, but broad-range frequency tuning is impossible in this design. A compact metal-mountable tag is constructed using a highly capacitive stacked planar inverted-L antenna (PILA) (Ooi et al., 2022), with the price of having a higher profile. A double-layer antenna, with a rectangular loop deployed for exciting a patch underneath, is proposed for designing a broadband on-metal tag (Lee et al., 2022). However, both tags in (Ooi et al., 2022) and (Lee et al., 2022) have a two-layer structure, which can make the fabrication processes much more complex, resulting in a shorter read range, than our proposed design. A novel miniature UHF RFID tag has been designed to be placed on metallic objects (Erman et al., 2022). The antenna structure includes a U-shaped feeder inductively coupled to two E-type

connected patches. However, it can only reach a short read range of only 6.9 meters. In contrast, as compared with previously published papers, our newly proposed tag has a simple antenna structure, and it is easy to design for achieving a far read distance. The tag structure is also slightly flexible due to the usage of soft foam and polyimide. Most importantly, it does not need any shorting stubs and metallic vias.

Table 4.2. Comparison between the proposed tag antenna and other reported metal-mountable tag antennas.

Ref.	Tag Dimension (mm³)	Chip sensitivity (dBm)	Power (EIRP)	Shorting Elements	Frequency (MHz)	Flexibility	Max. Read Distance (m)
This work	50 × 50 × 3.318	-20.85	3.28 W	None	920	Yes (Foam, PET)	9.0
(Bong et al., 2017)	30 × 30 × 3.0	-17.8	4 W	Stubs	915	Yes (Foam, PET)	7.2
(Sohrab et al., 2017)	86 × 41 × 3.2	-19.5	4 W	Stubs	865	No (FR4)	5.6
(Nguyen et al., 2021)	30 × 30 × 3.0	-22.9	4 W	Stubs	915	No (FR4)	6.4
(Zhang and Long, 2014)	26 × 14 × 2.4	-15.0	4 W	Vias	923	No (FR4)	5.5
(Zuffanelli et al., 2017)	45 × 45 × 1.27	-17	4 W	Vias	923	No (RO3010)	6.8
(Chiang et al., 2022)	50 × 50 × 3.38	-20.85	3.28 W	Stubs	868	Yes (Foam, PET)	16.2
(Inserra and Wen, 2021)	29.8 × 29.8 × 0.813	-17	4 W	Vias	922.5	No (RO4003C)	3.6
(Murugesh et al., 2022)	50 × 50 × 3.318	-20.85	4 W	None	915	Yes (Foam, PET)	9.0
(Ooi et al., 2022)	31.5 × 31.5 × 3.2	-17.8	4 W	Stubs	867	Yes (Foam, PET)	7.25
(Lee et al., 2021)	47 × 21 × 2.36	-20.85	4 W	None	868.2-929.8	No (FR4)	7
(Erman et al., 2022)	65 × 20 × 1.5	-20.5	4 W	None	915	Yes (PTFE)	6.9

4.6   Summary

For the first time, a single-layer patch antenna, which is made up of two complementarily coupled C-shaped patches, has been proposed for designing a tag that can be placed on metal. The two patches are tightly coupled for generating a sufficiently high antenna reactance for the purpose of achieving conjugate match with the RFID microchip. This reactance has been made as a simple frequency tuning mechanism with broad-range capability. The tag resonance can be arbitrarily adjusted from 920 MHz to 1.18 GHz without using any other external lumped components, shorting stubs, and vias. A full-wave simulation software has been employed for characterizing the antenna structure, while a simple transmission line model has been proposed for quick design and analysis. Despite its simple structure, the proposed tag can be read from a maximum distance of ~ 9 m. Reasonably good stability is also observed in the tag resonance frequency. Changes in the backing metal have very least effect on it.

CHAPTER 5

ZEROTH-ORDER SERPENTINE PATCH WITH OMNIDIRECTIONAL CHARACTERISTIC FOR ANTI-METAL TAG ANTENNA DESIGN

5.1   Introduction

In Chapter 3, a square ring resonator loaded with two distributed inductors was employed for designing a compact metal-mountable UHF tag antenna. Next, a single-layer patch antenna, which was constructed using two complementarily placed C-shaped patches, had been proposed for designing a metal-mountable tag with a wide-range of frequency tuning capabilities. However, both the tag antennas are directional, and the tag's resonance frequency is much dependent on the patch's width and length as well as the substrate's height. This is proposing a new serpentine patch antenna for designing an anti-metal tag with omnidirectional radiation characteristics on metallic surfaces. The zeroth-order resonance (ZOR) structure here is made up of two closely stacked serpentine patches for providing the parasitic elements that are required for supporting the zeroth-order resonance. Also, the geometrical parameters of the serpentine patches can be used for effectively tuning the tag resonance frequency. The proposed tag contains no complex structures, such as metallic vias, small notches, and narrow slots. Therefore, it can be easily made through a simple etching process. Due to the successful excitation of the ZOR mode, the proposed tag antenna can generate a reasonably good omnidirectional radiation pattern. The ZOR tag antenna here

is basically a composite right/left-handed transmission line (CRLH-TL) structure whose resonance frequency is independent of the patch's dimension because of its infinite wavelength.

5.2   Antenna Configuration and Design Analysis

5.2.1   Tag Antenna Configuration

Figure 5.1(a) shows the tag antenna configuration. The inlay contains two patches ($l \times l$), each of which has a serpentine patch as well as a ground plane. The two patches are made by depositing a 9-μm copper layer onto the top surface of a thin and flexible 50-μm polyimide substrate, as illustrated in the single-sided inlay shown Figure 5.1(b), which is easy to make using the conventional PCB etching technique. Through two metallic shorting walls, which are named as *Shorting Wall* 1 and *Shorting Wall* 2, the closely overlapped top and bottom serpentine patches are connected to the ground. Here, a Ucode 8 (Ucode 8, 2021) microchip, with an actual read sensitivity of -20.85 dBm and a chip impedance of $13 - j191$ Ω at 915 MHz, is connected across the gap at the center of *Shorting Wall* 1. The tag structure can be easily constructed by folding the inlay, where the folding steps are described in Figures 5.2(a)-(c). First, a polyethylene foam substrate ($\varepsilon_r = 1.03$, tan $\delta \sim$ 0.0001) with geometrical parameters of ($l = 50$ mm and $h_1 = 3.2$ mm) is placed on the ground. The flap that contains the bottom patch is then folded, wrapping around the foam, as depicted in Figure 5.2(a), using adhesive. Next, the top patch is folded, overlapping with the bottom patch, as shown in Figure 5.2(b), forming the final tag structure in Figure 5.2(c). As can be seen in

Figures 5.1(a)-(b) and 5.2(a)-(c), the top and bottom patches are closely stacked, and the two metallic serpentine patches are overlapped. The two patches are only separated by a thin layer of polyimide substrate (0.05 mm thickness). The overlapped patches can introduce sufficiently large capacitive reactance for supporting the ZOR mode and for bringing down the tag resonance frequency. With reference to Figures 5.1(a)-(b), for the final tag structure, the bottom and top patches are connected to the ground through *Shorting Wall* 1 and *Shorting Wall* 2, which are now located on the vertical sidewalls after the folding process. After being folded, the chip goes to the vertical wall as well, avoiding from being easily hit by an external object. The foam can function as the structural support, ensuring that the tag holding its shape. Other parameters are summarized in Table 5.1.

Table 5.1.   List of design parameters.

Design Parameter	Value (mm)	Design Parameter	Value (mm)
l	50	i_3	2.0
h	3.38	i_4	7.5
h_1	3.2	i_5	1.0
i_1	5.0	i_6	0.5
i_2	5.0	i_7	48
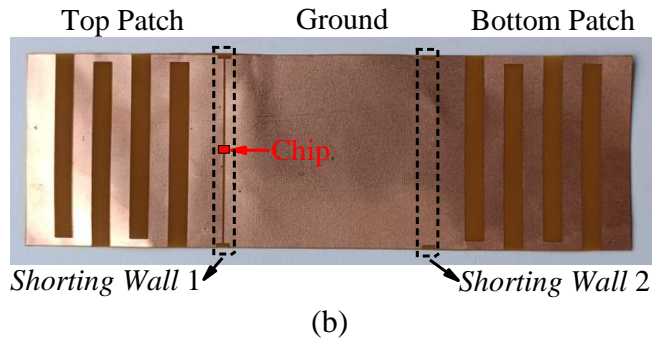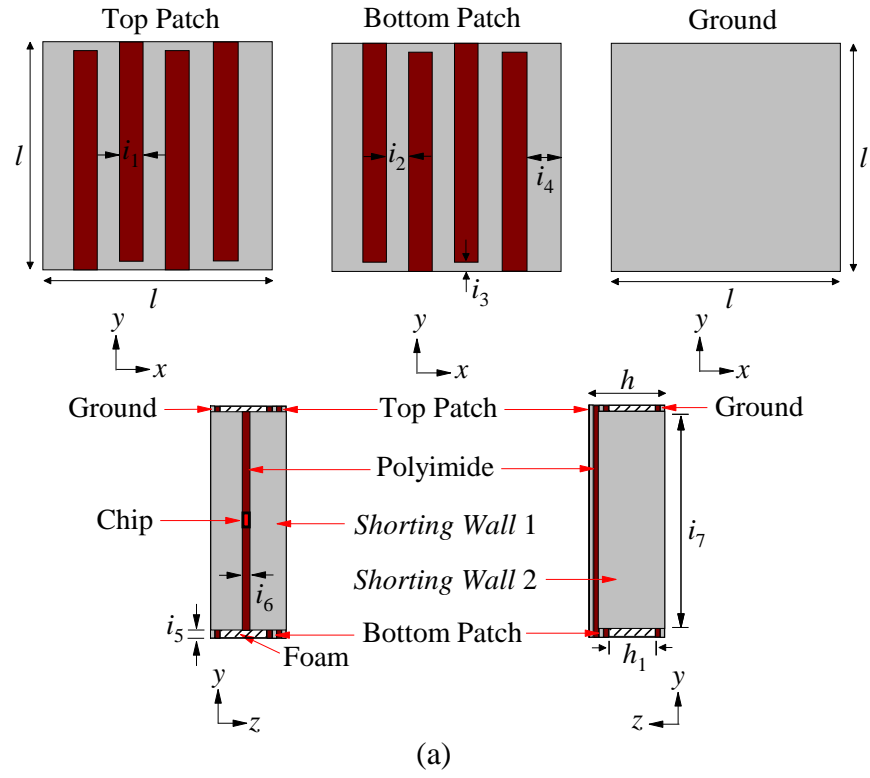
Figure 5.1. (a) Tag antenna configuration. (b) Single-sided inlay.
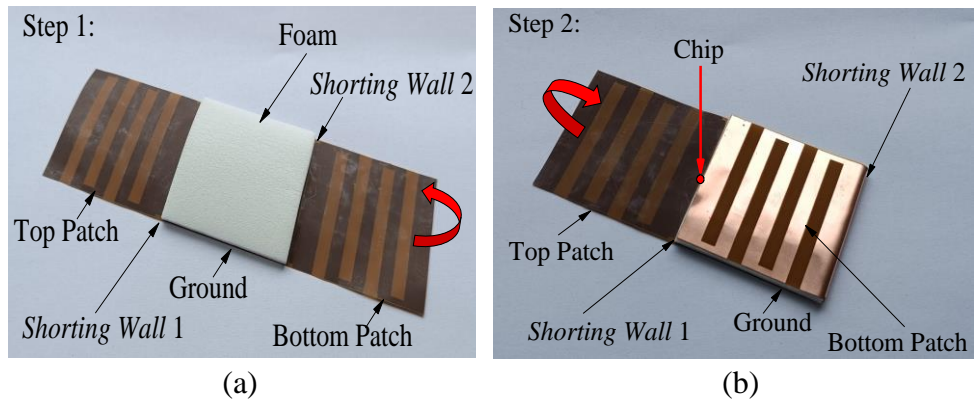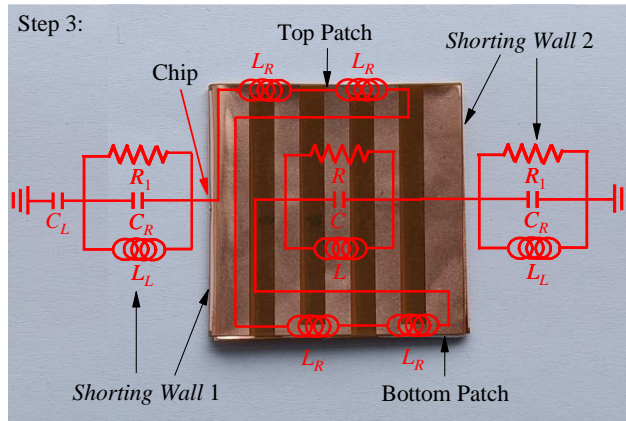
(c)

Figure 5.2. Tag antenna folding steps for fabrication. (a) Step 1: Foam with a square footprint is attached on the ground patch. (b) Step 2: The foam is covered by folding the bottom patch. (c) Step 3: The top patch is folded overlapping with the bottom patch for forming the final tag structure (parasitic elements are shown in red).

5.2.2 ZOR Equivalent Circuit and Unit Cell Simulation
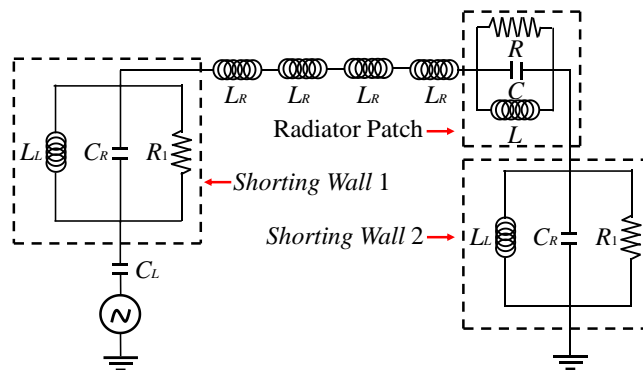
Figure 5.3. ZOR equivalent circuit.
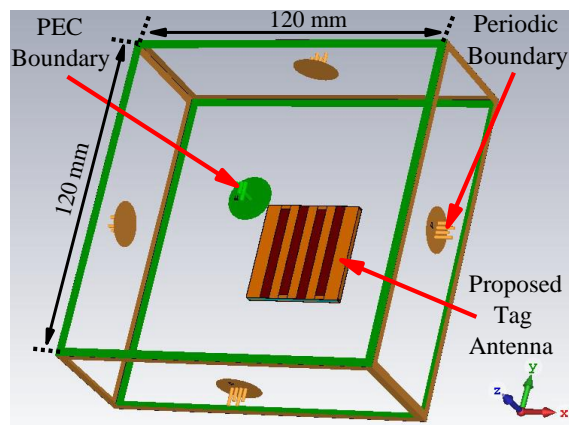
Figure 5.4. Unit cell simulation model.

An ideal equivalent circuit model, shown in Figure 5.3, is constructed based on the parasitic elements (highlighted in red) of the antenna structure in Figure 5.2(c) for analyzing the ZOR phenomenon. The serpentine patch is represented by a $R\|L\|C$ resonance tank. The long serpentine patches are inductive and provide the right-handed inductances (L_R); while the two shorting walls are to provide the left-handed inductances (L_L) and the right-handed capacitances (C_R). The left-handed capacitance is provided by the capacitive effect formed in between the chip and the ground plane. As observed from Figure 5.3, the antenna structure can provide the required parasitic reactances that are required for enabling the zeroth-order resonance. Subsequently, as shown in Figure 5.4, the antenna structure is placed inside a 120 mm × 120 mm unit cell by removing the microchip for simulating the eigenmodes. The unit cell height is approximately ten times the thickness of the substrate (Dispersion Diagram). The two boundaries that are normal to the z axis are set to $E_t = 0$, which is equivalent to the perfect electric conductor (PEC) (Tagformance, 2012); while the four boundaries that are normal to the x and y axis' are defined as periodic boundaries. The dispersion curves are plotted as a function of the tuning parameters (i_2, i_3), as shown Figures 5.5(a)-(b). Obviously, the operating frequency is not affected much by the footprint (βl), which is a crucial feature of a ZOR structure. (i_2, i_3) can be applied for tuning the ZOR frequency in the range of 790 MHz – 900 MHz effectively. Also, for the case of ($i_2 = 5$ mm, $i_3 = 2$ mm), the zeroth-order resonance frequency ($\beta l = 0$) is seen to be around 893 MHz, which is quite close to the proposed tag antenna's operating frequency (920 MHz). Electric fields are simulated for the eigenmode (without a chip) at the ZOR frequency, as shown

in Figures 5.6(a)-(b), in the *xy* and *xz* planes. The electric fields around the serpentine patches are all pointing upward in the *z*-direction, showing the zeroth-order property ($n = 0$). This is a distinct feature of the ZOR antenna (Li et al., 2020), (Park et al., 2011), (Pyo et al., 2009). Additionally, (Park et al., 2007) explains how the ZOR antenna works from a theoretical point of view. Field distributions also show that the antenna is capacitive in nature. To maintain the ZOR mode, the antenna structure must provide enough parasitic elements (L_L, L_R, C_L, C_R). The composite right/left-handed (CRLH) characteristics can be tuned to adjust the ZOR frequency.
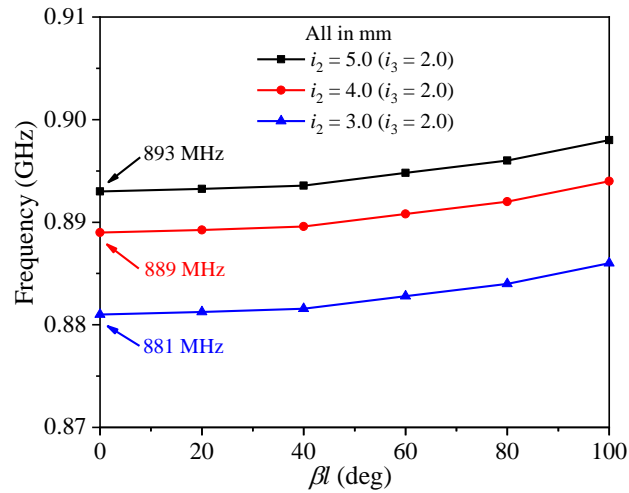
(a)
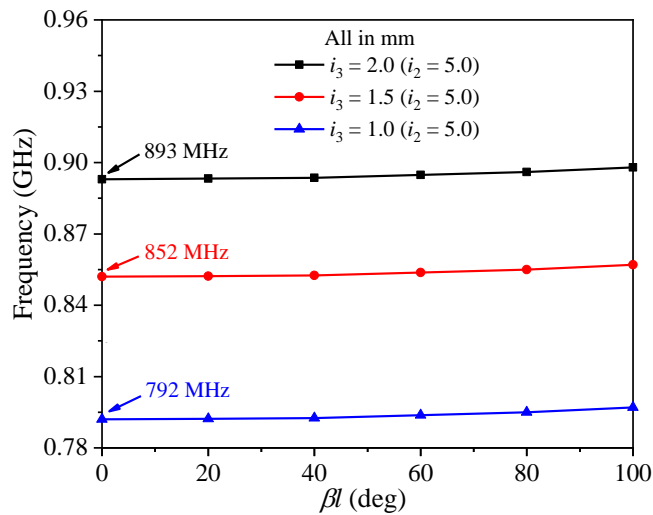
(b)

Figure 5.5. Dispersion curves as a function of (a) i_2 and (b) i_3.

95
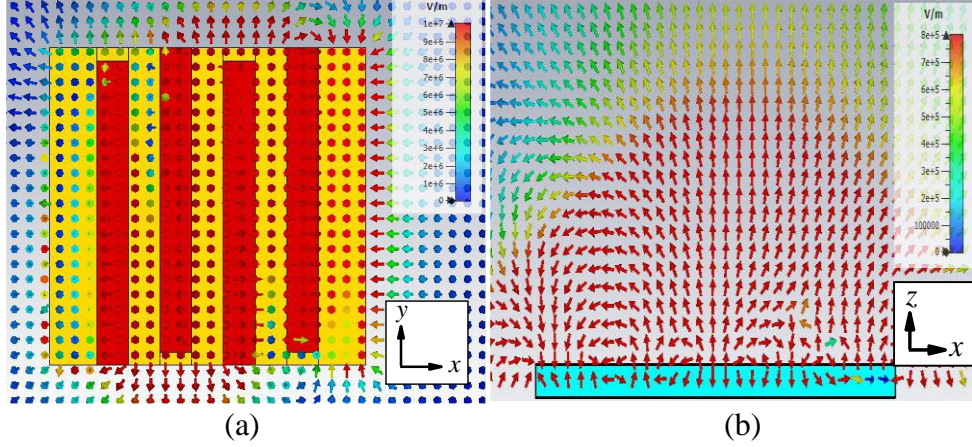
Figure 5.6. Electric field distributions in the (a) *xy*-plane and (b) *xz*-plane at the ZOR frequency analyzed using the eigenmode (without a chip).

5.2.3   Antenna Design Analysis

Next, with the inclusion of the microchip for forming the final tag, the electric fields are now simulated. Here, the microchip is replaced with a complex port set to represent the actual chip impedance ($13 - j191$ Ω). From now onwards, the tag antenna is always placed at the center of a 200 mm × 200 mm aluminum plate. The corresponding electric fields in both planes, which are simulated in Figures 5.7(a)-(b), are found to be like those in Figures 5.6(a)-(b). The surface currents on the top surface are then shown Figure 5.8. It has been observed that the currents on the four arms are forming an electric current loop. To have further insight, the electric fields are inspected from the side apertures around the four arms, and their corresponding equivalent magnetic currents are shown in Figure 5.9. With reference to the figure, the four magnetic currents can form a magnetic loop to generate omnidirectional radiation. The formula $\vec{M} = -\vec{n} \times \vec{E}_a$ (Balanis, 2005) can be used to calculate the equivalent magnetic currents on the four apertures, as shown in Figure 5.9. By applying

96

the equivalence principle, the magnetic currents on the bottom and top apertures can be expressed using $\vec{M}_1 = \vec{M}_x = -(-\vec{a}_y) \times \vec{E}_z$ and $\vec{M}_3 = -\vec{M}_x = -\vec{a}_y \times \vec{E}_z$. Those on the left and right are $\vec{M}_2 = \vec{M}_y = -\vec{a}_x \times \vec{E}_z$ and $\vec{M}_4 = -\vec{M}_y = -(-\vec{a}_x) \times \vec{E}_z$.

(a)   (b)
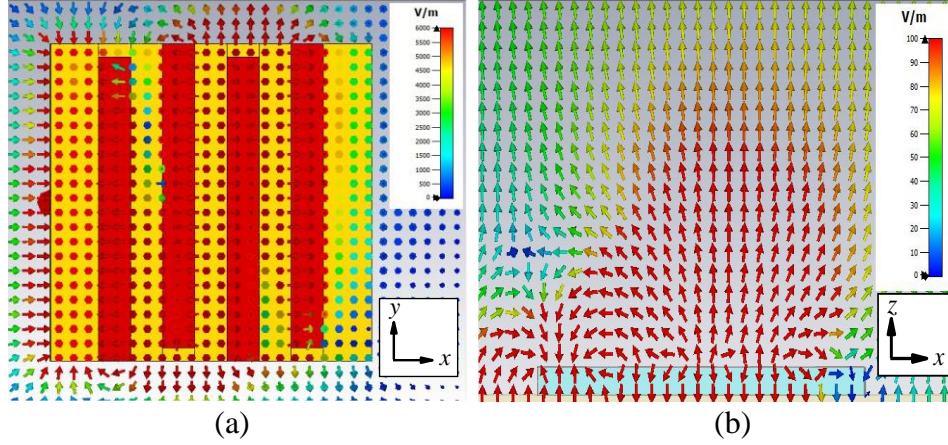
Figure 5.7. Electric field distribution in the (a) *xy*-plane and (b) *xz*-plane for the tag antenna with a microchip.
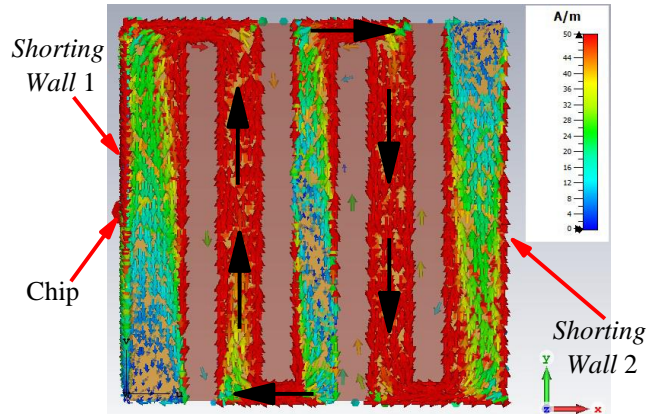
Figure 5.8. Surface currents on the four arms on the top patch for the final tag with a microchip.

This section is to study the effect of the bottom patch. To do this, first, the bottom patch and the *Shorting Wall* 2 are removed for the establishment of a single-layer tag, with the corresponding antenna impedances (Z_{ant}) and power transmission coefficients (τ) shown in Figures 10(a)-(b). With reference to Figure 10(a), without the bottom patch, the tag antenna's resonance

97

frequency has increased up to 1.02 GHz, with $Z_{ant} = 5.97 + j178.96$ Ω, which ranges far beyond the regulated UHF RFID band due to a significant reduction in reactance. The realized gain (G_r) is low (−11.68 dBi). Due to poor impedance matching, the τ value of this tag (without the bottom patch) has reduced (0.53), as depicted in Figure 10(b). Electric fields of the single-layer tag antenna are essentially the same as the final structure, except that with a significant reduction in the field strength. After the inclusion of the bottom patch, the frequency can be pushed down to 920 MHz. It shows that the existence of the bottom patch is essential for decreasing the tag resonance frequency to the UHF RFID band. The tag antenna's Z_{ant} and G_r for the final tag design are $11.24 + j190.94$ Ω and −3.42 dBi, respectively, as shown in Figure 10(a). It has achieved a good $\tau \sim 0.99$.
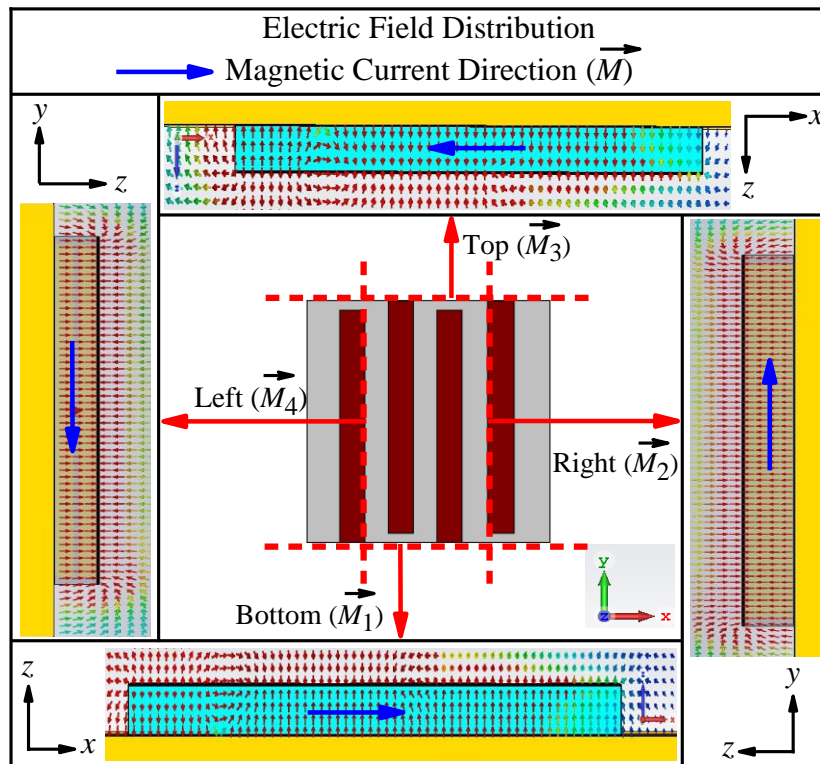
Figure 5.9. Equivalent magnetic currents on the four apertures on the side walls.
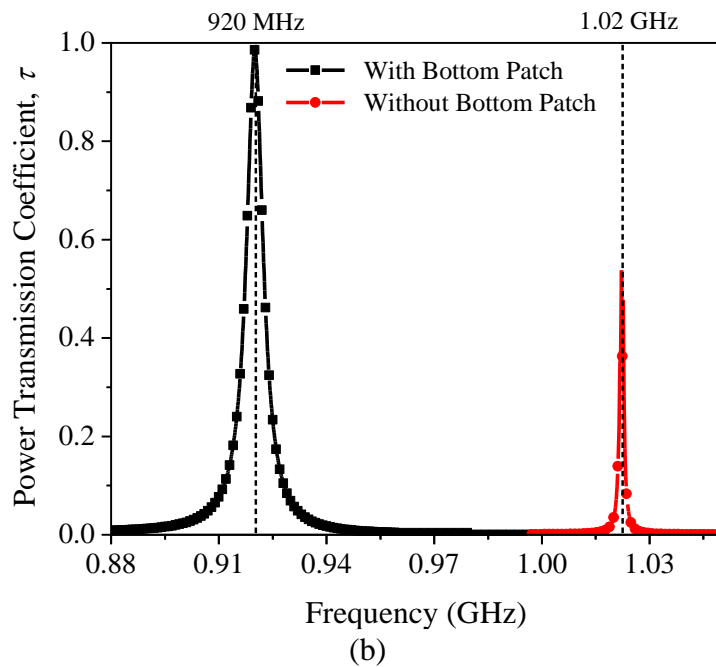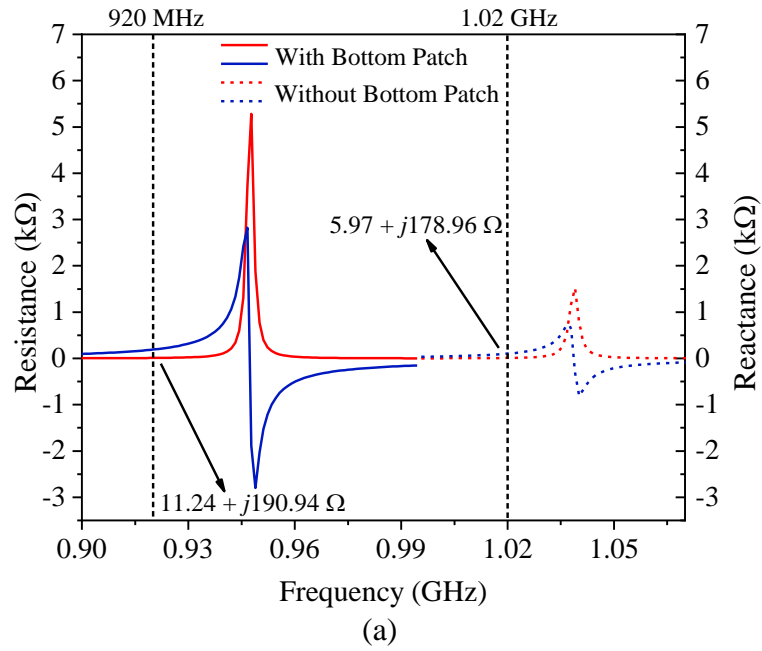
Figure 5.10. The tag structure for cases with and without the bottom patch. (a) impedance analysis, and (b) power transmission coefficient analysis.

5.3   Parametric Analysis

The effects of the key tuning parameters (i_2, i_3) on the changing trends of τ and Z_{ant} are also further explored here. Changing the patch width (i_2) of the top and bottom patches concurrently can cause the inductive parasitic (L_R) to vary. First, i_2 is decreased from 7.0 mm to 3.0 mm. As seen in Figure 5.11(a), decreasing i_2 lowers the resonance frequency but maintains the τ value almost a constant. For every 1 mm decrease in i_2, a drop of 8.3 MHz is seen in the tag resonance frequency. Despite the change, the resistance and reactance amplitudes can be kept almost unchanged, as observed in Figure 5.11(b). The effects of the patch width (i_3) are then studied. As shown in Figure 5.12(a), raising i_3 from 1.0 mm to 3.0 mm increases the tag antenna's resonance frequency but retains τ. As the patch width is reduced, the tag antenna has shown an increase in both its resistance and reactance at the tag resonance frequency, as can be seen in Figure 5.12(b).

(a)
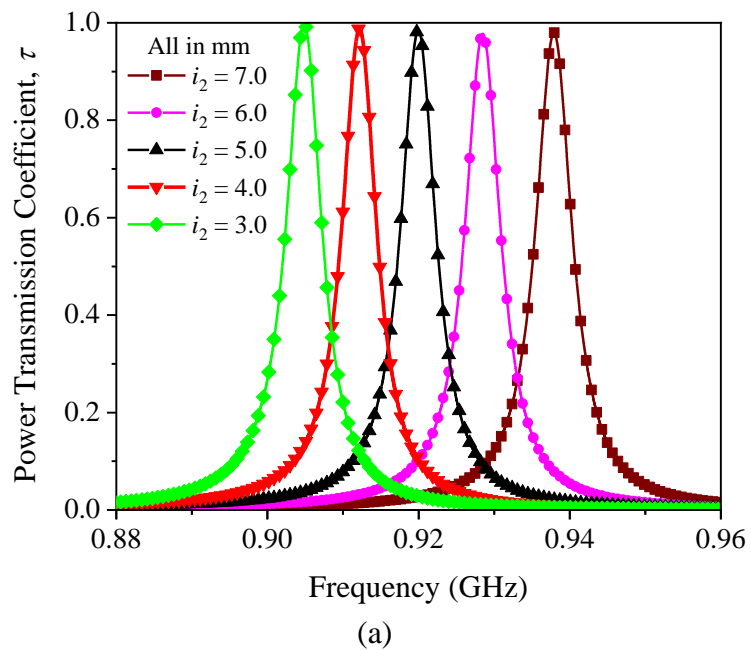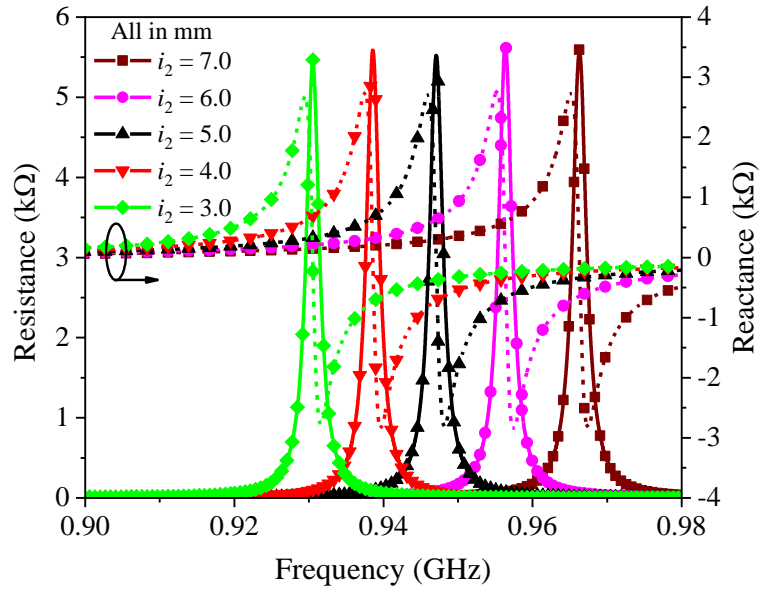
(b)

Figure 5.11. Simulated (a) τ and (b) Z_{ant} by varying i_2.
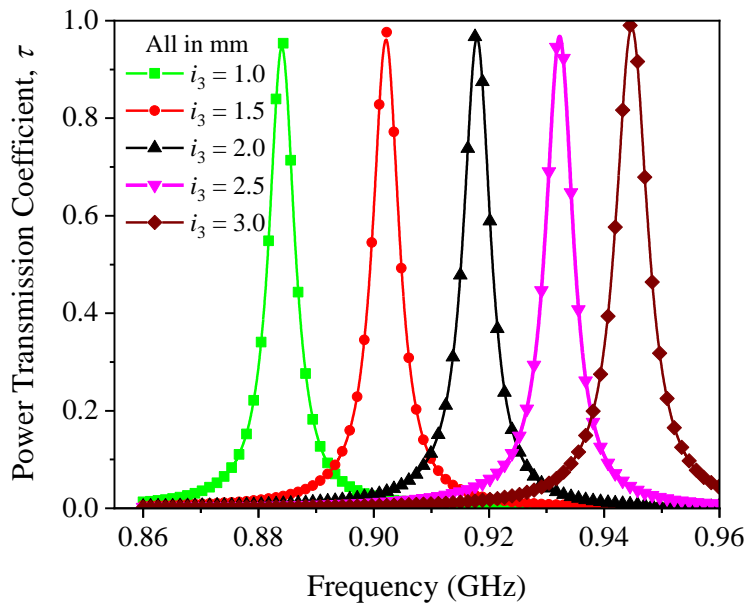
(a)
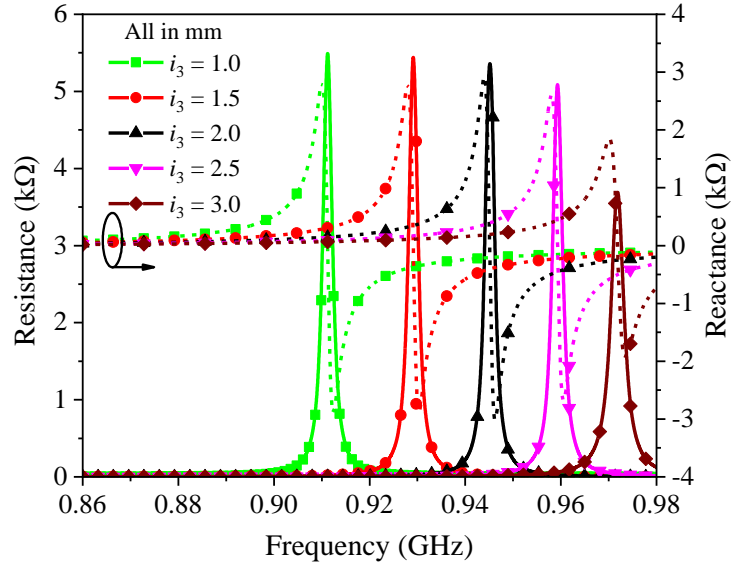
(b)

Figure 5.12. Simulated (a) τ and (b) Z_{ant} by varying i_3.

5.4 Measurement Setup

The optimized parameters in Table 5.1 are employed for prototype fabrication. Measurements were conducted inside an anechoic chamber equipped with the Voyantic Tagformance Measurement System. Figure 5.13(a) shows the placement of the prototype on an aluminum plate, while Figure 5.13(b) shows the measurement setup inside an anechoic chamber. A linearly polarized (LP) reader antenna (8 dBi Gain), shown in Figure 5.13(b), is positioned at a fixed distance from the tag. The realized gain can be found out from $G_r = P_{ic} / (L_T \times P_{tx})$, where L_T is the total cable and free space losses, P_{ic} is the read sensitivity of the microchip, and P_{tx} is the reader's threshold power level at a specific frequency. Figure 5.14 has compared the simulated and measured realized gains at $\theta = 90^o$. The maximum realized gain is measured to be –4.12 dBi (915 MHz), with good agreement observed between the simulated and measured results.

102
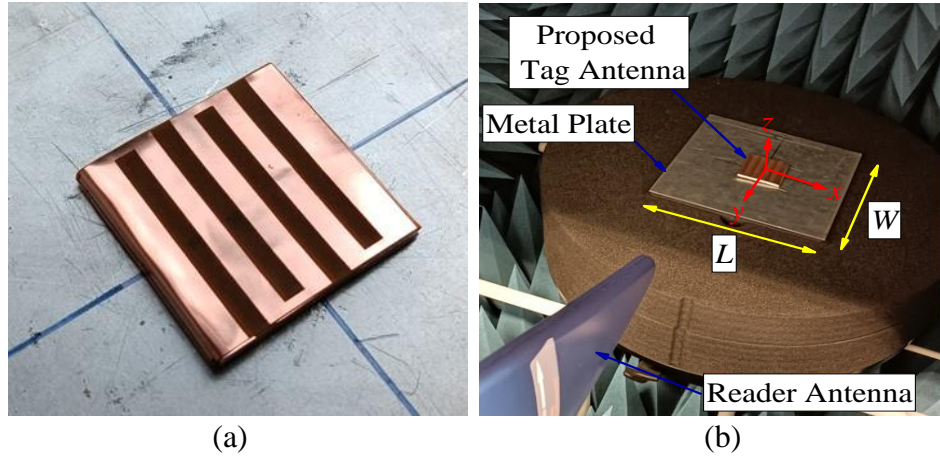
Figure 5.13. (a) Aluminum plate with the prototype attached in the middle. (b) The measurement setup in the anechoic chamber.
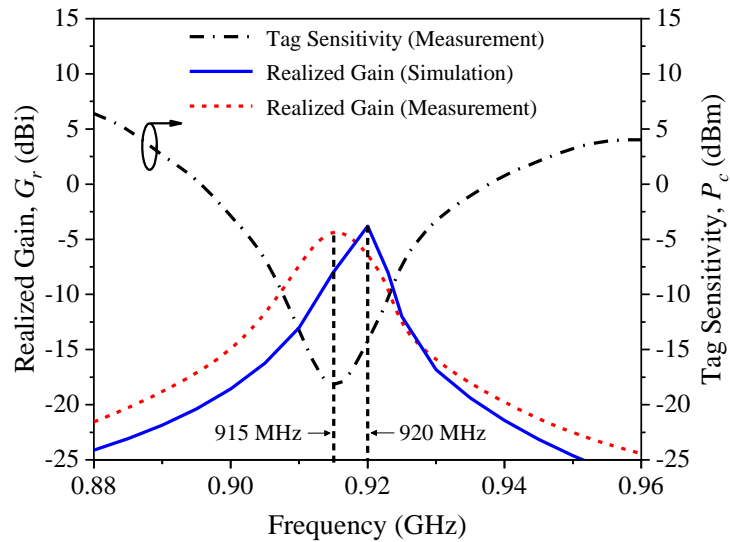
Figure 5.14. Measured tag sensitivity. Also shown are the measured and simulated realized gains.

5.5   Experimental Results and Discussion

Then, the read characteristic of the tag antenna is studied in the *xz*, *yz*, and *xy* planes, as shown in Figures 5.15(a)-(b). Here, (θ, ϕ) are defined following the standard spherical coordinate system. As can be seen in Figure 5.15(a), good omnidirectional radiation patterns have been obtained. It is observed in Figure 5.15(a) that a read distance of ~8 m has been achieved with uniform coverage

in the azimuth plane. Figure 5.15(b) shows a typical omnidirectional characteristic in the xz and yz planes, with nulls at $\theta = 0°$ and $\theta = 180°$. The maxima is located at $\theta \sim 50°$. It is important to take note that the tag is intended to be stuck on the top surface of a metallic item in a department store for providing coverage in the azimuth plane around it. As a result, the tag has to be readable from its entire azimuth plane.
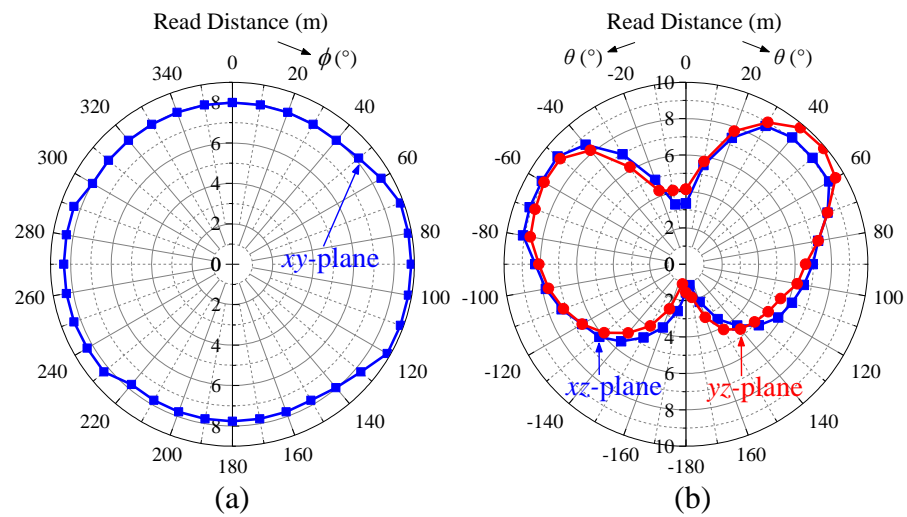
Figure 5.15. Read patterns of the proposed tag antenna in the (a) *xy* plane and (b) *xz, yz* planes at 915 MHz.

The tag antenna is now tested on different aluminum plates, all with a thickness of ~5 mm, and the respective maximum measured read ranges ($\theta \sim$ 50°) are shown in Figures 5.16(a)-(b). The prototype is always attached to the middle of the plate throughout the measurements. When W is kept at 20 cm, the read range can be maintained in the range of 10 - 12 m by progressively lowering L from 24 cm to 5 cm, as seen in Figure 5.16(a). The results are shown in Figure 5.16(b) when the plate width W is changed while the length L is maintained at 20 cm. When the plate width is reduced, the read distance can still be kept beyond 10 m, although it has dropped slightly.
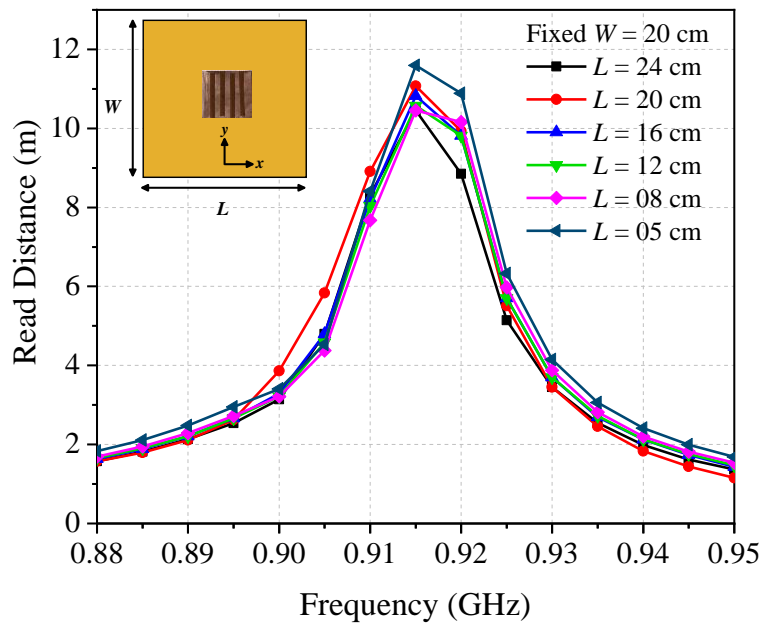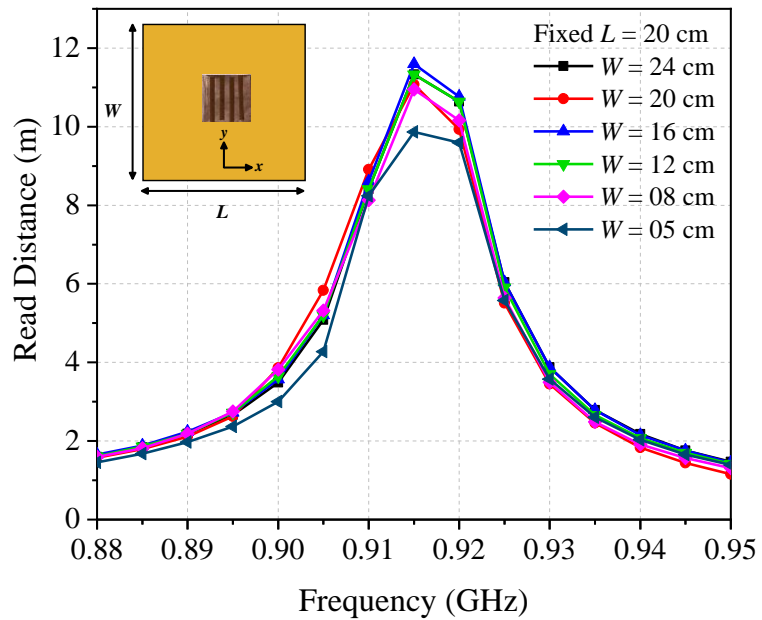
Figure 5.16. The read distances on the aluminum plate were measured by varying (a) the length of plate *L* and (b) the width of plate *W*.

The proposed tag antenna is also tested for several implementation scenarios using a few metallic household items chosen randomly from a departmental store, as shown in Figure 5.17. Referring to Figure 5.18(a), all the household items can be read beyond ~8.9 m when the tag is measured from

its *y*-axis direction. Worth mentioning is that the operating frequency of the proposed tag antenna is stable, and it is not affected much by the backing metallic items. From Figure 5.18(b), the same household items are used to test the read pattern in the *xy* plane. Good omnidirectional characteristic, with a fluctuation of less than 2 m, is observed in the azimuth cutplane. It shows that the proposed tag can be accessed in the entire azimuth plane.
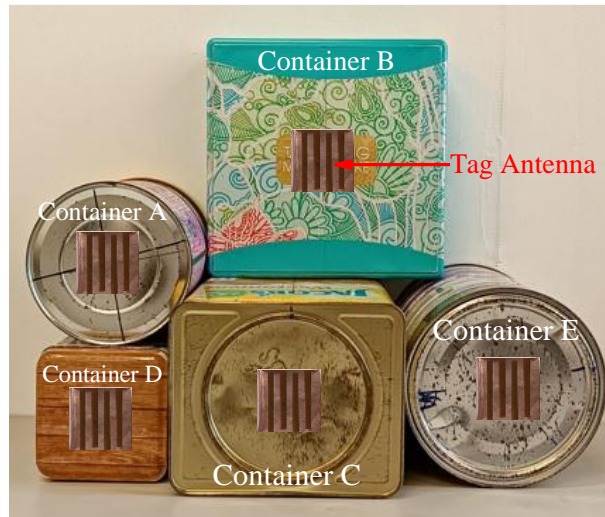
Figure 5.17. Household containers made of metal.
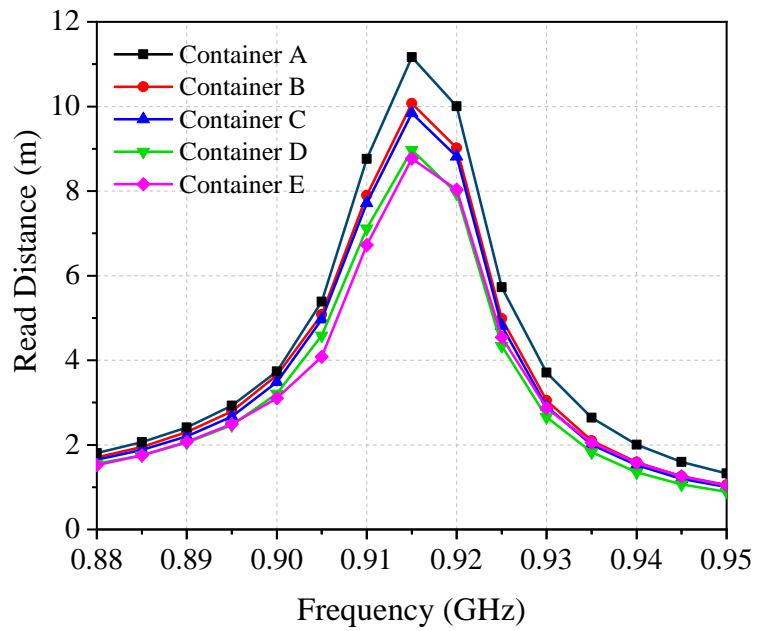
(a)
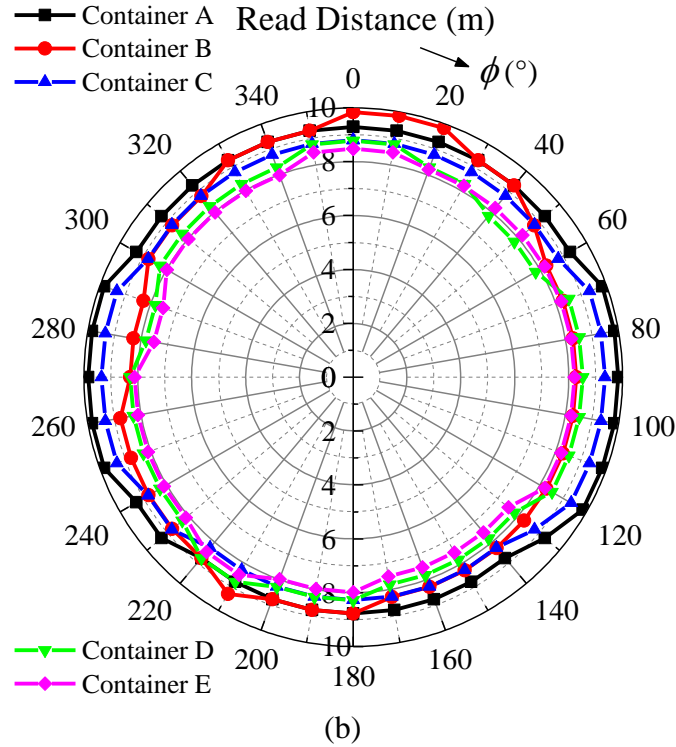
Figure 5.18. (a) Measured read ranges as a function of frequency and (b) measured read patterns in the azimuth plane for the household containers.

5.6   Summary

For the first time, the ZOR mode of a novel serpentine patch structure is excited for designing an omnidirectional anti-metal tag antenna in the UHF RFID band. The two serpentine patches are closely stacked for producing a strong capacitive reactance. It has been shown that the patches can generate sufficient parasitic reactances for enabling the ZOR mode. Also found is that the geometrical dimension of the serpentine patches can be employed for tuning the tag resonance frequency effectively. The operating principle has been verified using a unit cell, where the dispersion curves are simulated. When tested on metal, the proposed tag can produce a good omnidirectional radiation pattern, with a maximum reading distance of around 10 m at 915

MHz. It has a uniform spatial coverage (> 8 m) in the entire azimuth plane. Finally, the radiation characteristic and frequency response of the tag are found to be very stable. They are not affected much by changes in the backing metal object.

CHAPTER 6

POLARIZATION-INSENSITIVE PLANAR PATCH ANTENNA WITH LARGE EMBEDDED SERIAL CAPACITANCE

6.1   Introduction

The tag antennas in Chapters 3 and 4 can only generate directional radiation patterns. In Chapter 5, the tag antenna can generate an omnidirectional radiation pattern above the metal plate. However, all the tags are only readable in a certain direction. This may result in a considerable rise in the miss rate. In the past decade, many linearly polarized (LP) antennas have been used to design metal tags with directional radiation patterns. But the demand for planar polarization-insensitive UHF tags has been growing as radiators can provide readability in all directions. In this project, a polarization-insensitive planar patch antenna with a large embedded serial capacitance is proposed for constructing a metal mountable tag using merely a single radiator. The proposed antenna structure itself contains two flaps of patches, which are very closely overlapped, for generating a large capacitive reactance for reducing the resonance frequency of the tag. It has been found that the surface currents in the overlapped region are in the reverse direction as the large capacitance is virtually placed in series. This feature has been tactfully employed for producing a pair of orthogonal currents for designing the polarization-insensitive tag antenna. As a result, it can generate orthogonal fields uniquely,

making it readable from almost all directions at all points above the metal surface.

6.2   Antenna Configuration and Design Analysis

6.2.1   Tag Antenna Configuration

Figure 6.1(a) shows the configuration of the proposed tag antenna. The antenna inlay contains two patches ($w \times i_1$) as well as a ground, both of which are made on a thin layer of copper (thickness of 0.009 mm) located on a flexible thin polyimide substrate with a thickness of 0.05 mm, as shown in Figure 6.1(b). The inlay is simple to make using the regular PCB fabrication techniques. The tag antenna's footprint was first reproduced on a photoresist mask that had already been laminated on the inlay's copper layer. The unwanted copper was then removed by etchant after being exposed to ultraviolet light. Through two metallic stubs, which are named as *Stub* 1 and *Stub* 2, the top and bottom patches are joined to the ground, and an integrated RFID microchip is bonded across the gap at the center of *Stub* 1. A Ucode 8 microchip, with an actual read sensitivity of −20.85 dBm and an input impedance of $13 - j191$ Ω at 915 MHz, is used for the tag design. Next, the tag is formed by folding the inlay. The folding technique is now elaborated, as shown in Figures 6.2(a)-(c). First, a polyethylene foam substrate ($\varepsilon_r = 1.03$, tan $\delta \sim 0.0001$), with geometrical parameters of ($w = l = 40$ mm and $h_1 = 3.2$ mm), is placed on the ground. The flap that contains the bottom patch is then folded wrapping around the foam, as depicted in Figure 6.2(a), using adhesive. Next,

the top patch is folded overlapping with the bottom patch, as shown in Figure 6.2(b), forming the final tag structure in Figure 6.2(c). It should be mentioned that the microchip is soldered across the gap at the center of *Stub* 1. The top and bottom patches are closely stacked, and their metallic layers are partially overlapped, where the two patches are only separated by a thin layer of polyimide substrate. The overlapped patches can introduce sufficiently large capacitance that is crucial for bringing down the resonance frequency to the useful UHF RFID band. It will be later shown that the overlapped region is also important for introducing reverse surface currents that are instrumental for the generation of the polarization-insensitive radiation pattern. Here, the bottom and top patches are connected to the ground through *Stub* 1 and *Stub* 2, which are now located on the vertical sidewalls after the folding process, in the final tag structure. In this case, the ground patch acts as an isolator for reducing the effect of the backing item. The chip goes to the vertical wall as well, avoiding from being easily hit by an external object. The foam material is soft, and it can provide a certain level of flexibility. As a result, the tag can be attached to an object with a slightly uneven curvature. Additionally, the foam functions as a structural support, ensuring that the tag can hold its shape. This tag is simulated by attaching its ground at the middle of a 20 cm × 20 cm metal plate. The simulation software (CST Studio Suite) has been used for all the optimization and design processes. The proposed tag antenna's detailed geometrical parameters, which are designed to work in the USA UHF RFID passband, are given in Table 6.1.

Table 6.1. Optimized design parameters of the proposed tag antenna.

Design Parameter	Value (mm)	Design Parameter	Value (mm)
l	40	i_1	25
w	40	i_2	1.1
h	3.38	i_3	6
h_1	3.2	-	-

(a)

(b)
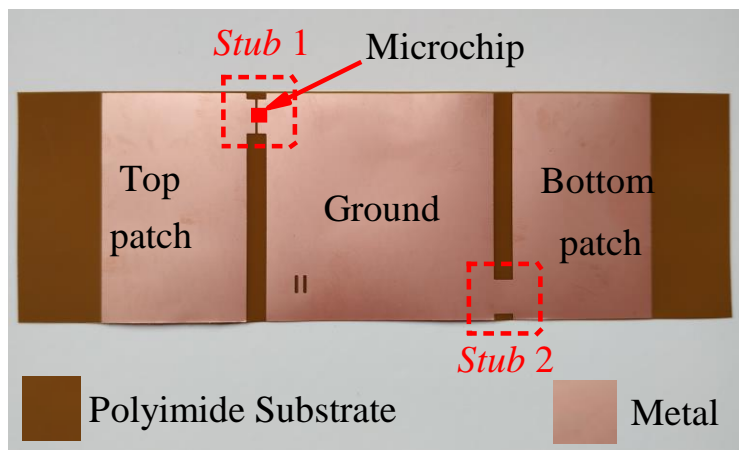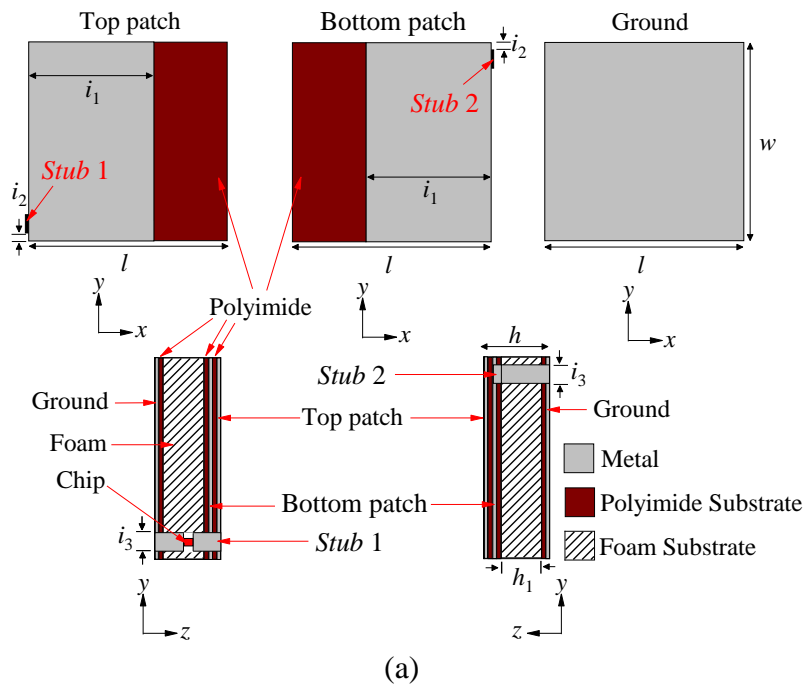
Figure 6.1. (a) Configuration of the proposed tag antenna. (b) Flexible antenna inlay.
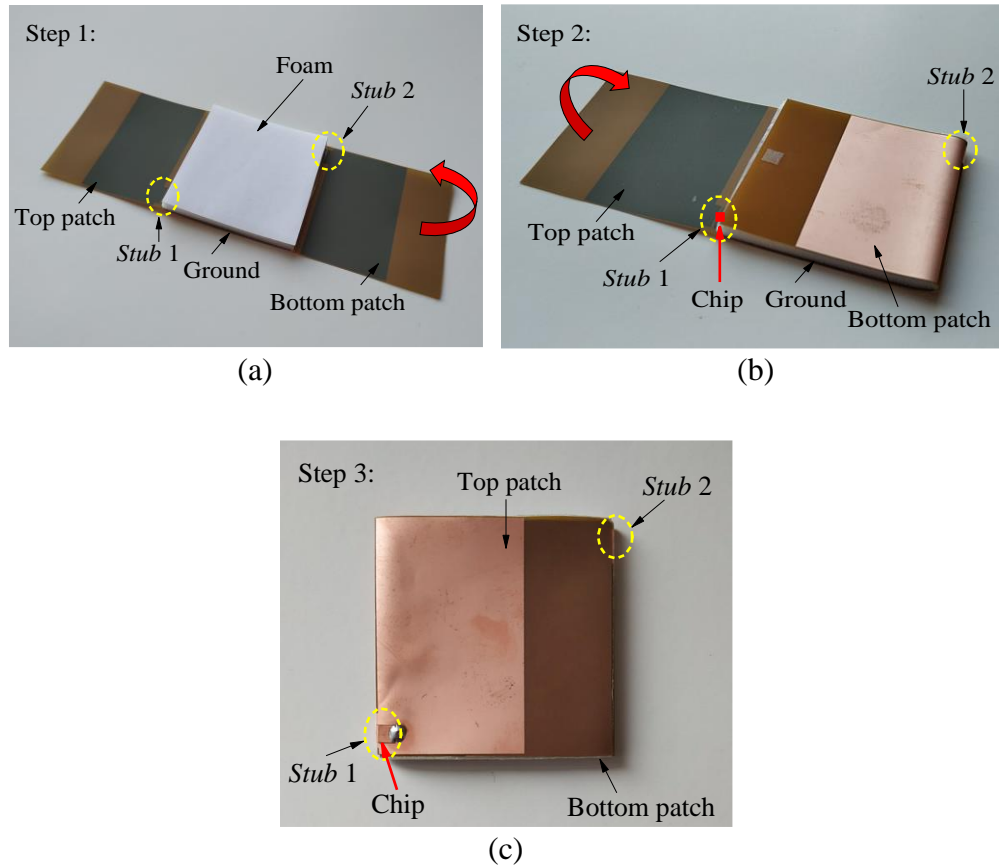
Figure 6.2. Fabrication process of the tag antenna by folding. (a) Step 1: A foam with square footprint is attached on the ground patch. (b) Step 2: The bottom patch is folded so that it can cover the foam substrate. (c) Step 3: The top patch is folded overlapping with the bottom patch for forming the final tag structure.

6.2.2 Antenna Design Analysis

To begin the simulation, the microchip is replaced by an external discrete port with a complex impedance set to represent the actual chip impedance $(13 - j191\ \Omega)$. The antenna design is initially analysed by removing the bottom patch as well as *Stub* 2 for establishing a single-layer tag. As shown in Figure 6.3(a), the tag antenna's resonance frequency has moved up to 2.89 GHz with an antenna impedance of $(41.98 + j180.86\ \Omega)$, which goes far beyond the regulated UHF RFID band due to a significant reduction in reactance. Although the realized gain is high (6.601 dBi), the power transmission

113

coefficient is low (0.67), as shown in Figure 6.3(b), due to poor impedance matching. Next, the top and bottom patches are aligned in the same layer with a gap between them. The tag antenna's resonance frequency has reduced to 1.57 GHz with an antenna impedance of (5.24 + j8.21 Ω). As a result, the realized gain is very low (−13.85 dBi), and the power transmission coefficient has also become very low (0.05) due to poor impedance matching. After including the bottom patch, the frequency can be shifted back to 920 MHz. It shows that the existence of the overlapped region, which will be further discussed in detail later, is essential for reducing the tag resonance frequency to the 860 MHz - 960 MHz frequency range. The final tag antenna's impedance and realized gain are 9.83 + j191.33 Ω and 1.07 dBi, respectively, as shown in Figure 6.3(a), which has achieved an excellent power transmission coefficient of 0.9.

The surface currents on the top and bottom patches are analysed next to demonstrate the working concept of the tag. Design simulation is begun by varying the patch length i_1, where the two shorting stubs are both shifted to the center. First, the patch length is shortened to $i_1 = 15$ mm so that there is a gap of 10 mm left in between the two patches, as shown in Figure 6.4(a). Here, the tag resonance frequency has increased to 2.0456 GHz, with a poor reflection coefficient of $|S_{11}| = –0.0259$ dB. The two patches are not well excited at this frequency and weak surface currents are observed due to weak capacitive coupling. Subsequently, the two patches are made equal in length ($i_1 = 20$ mm), as shown in Figure 6.4(b), where each has one edge aligned along the centerline, resulting in no gap.
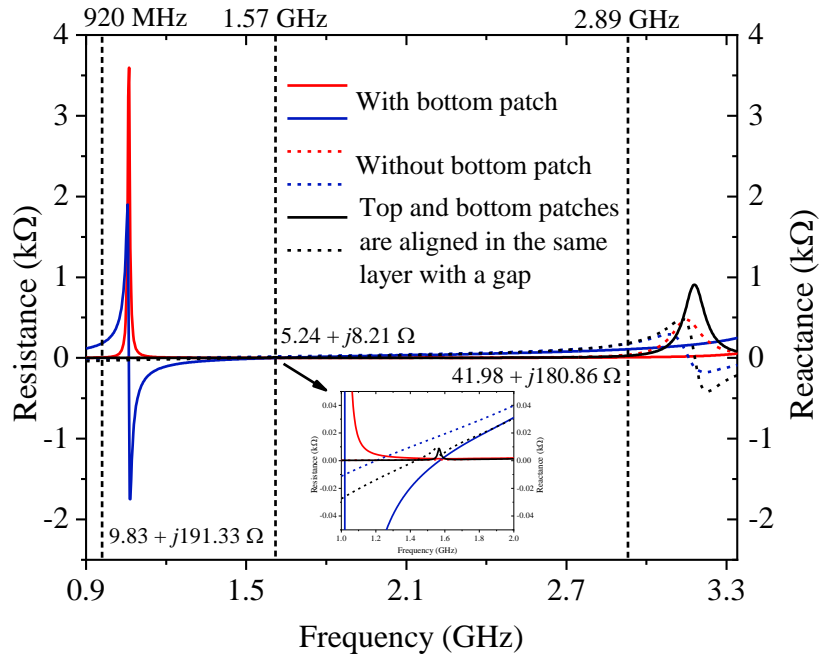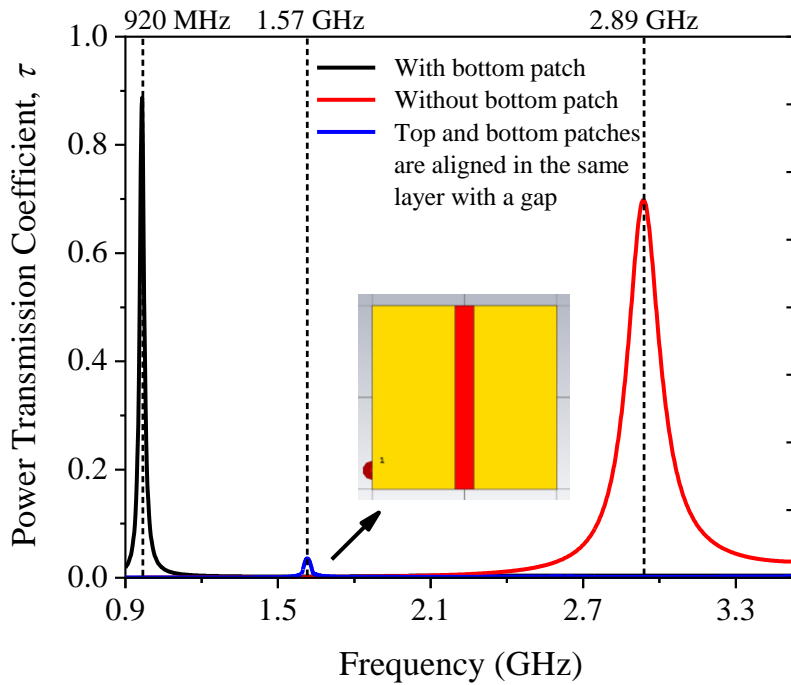
Figure 6.3. The tag configuration for the cases with and without the bottom patch and both patches are aligned in the same layer with a gap (a) impedance analysis and (b) power transmission coefficient analysis.

Due to the tight capacitive coupling between the edges, the tag resonance has gone down to 1.4207 GHz and the reflection coefficient has improved to –3.252 dB. Here, the formation of a completed circuit loop has enabled stronger currents to flow in one direction. The patch lengths are then increased to i_1 = 25 mm, resulting in an overlapped region of 10 mm, as depicted in Figure 6.4(c), again, with the two shorting stubs at the center. Strong capacitive coupling is made possible due to close proximity between the two patches in the overlapped region. As previously mentioned, the separation distance between the top and bottom patches is very thin and it is only about the thickness of a polyimide substrate. Also, the surface currents in the overlapped region are found to be in the opposite direction as those in the non-overlapped regions. Because of the strong capacitance, the tag resonance frequency has been reduced to 1.0818 GHz. Enhancement in the capacitive reactance has also improved the reflection coefficient to –18.03 dB. Finally, with reference to Figure 6.4(d), the two shorting stubs are symmetrically displaced (for the case of 10 mm overlap), with *Stub* 1 moved to the lower left and *Stub* 2 shifted to the upper right, and the corresponding currents are simulated. The displacement has caused the current path to become longer and the tag resonance frequency to shift down to 920.3 MHz (with $|S_{11}|$ = –14.21 dB). It also causes the currents in the overlapped region to become orthogonal with those in the non-overlapped regions. The pair of orthogonally oriented currents has enabled the formation of the polarization-insensitive radiation pattern. The surface currents are also captured at different snapshots for the source phases of 0º, 90º, 180º, and 270º, as illustrated in Figs. 5(a)-(d). The current distributions on the radiator patches are in-phase at the source phase of

0° and 90° as their source currents are flowing in the same direction. The current distribution at the source phase 180° becomes out-of-phase due to the change of current direction. Two flows of linearly polarized diagonal currents, which are mutually orthogonal, are observed in the overlapped region. Each of the currents can be decomposed into its subcomponents in the x- and y-directions. The two diagonal currents are instrumental for generating the E_θ and E_ϕ fields, which are orthogonal in nature, for the polarization-insensitive tag antenna. At each snapshot, the orthogonality of the currents can be maintained. This has ensured the sustainability of polarization insensitivity in the radiation pattern when time elapses.
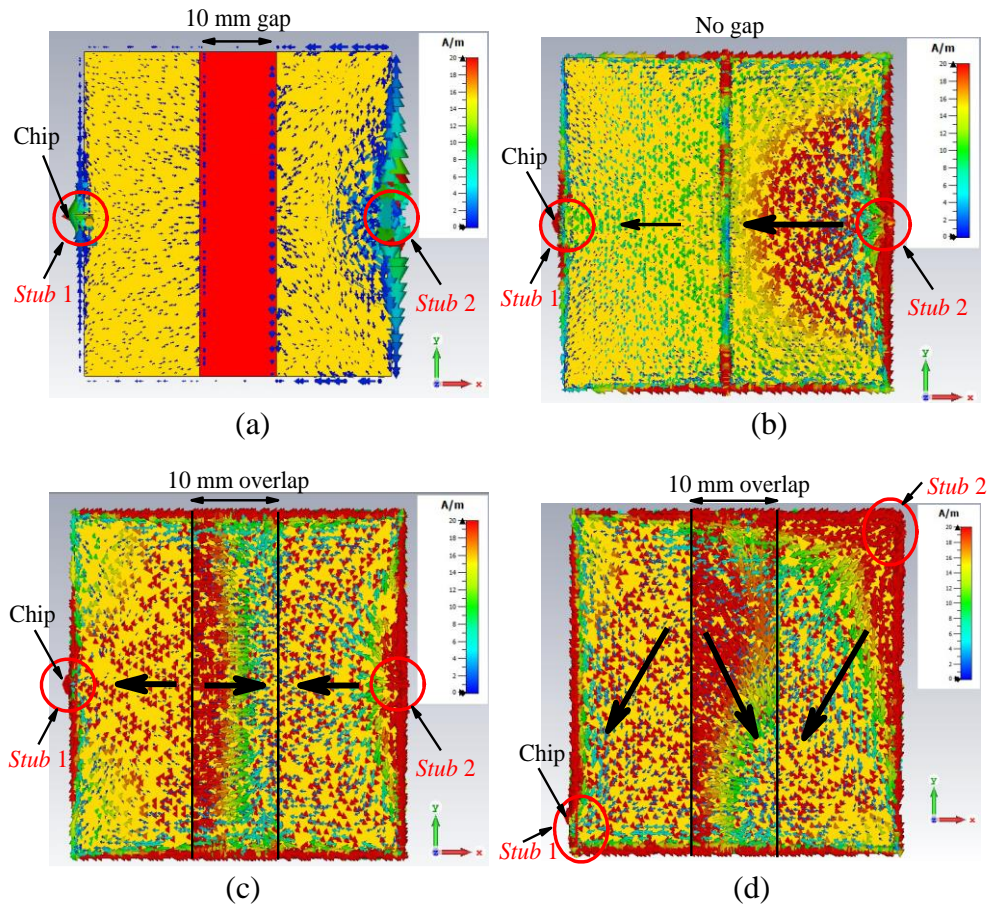
Figure 6.4. Surface currents on the top and bottom patches for the tag antenna with (a) 10 mm gap (b) no gap (c) 10 mm overlap and (d) 10 mm overlap with shorting stubs moved to the corners.

(a) 0°   (b) 90°

(c) 180°   (d) 270°
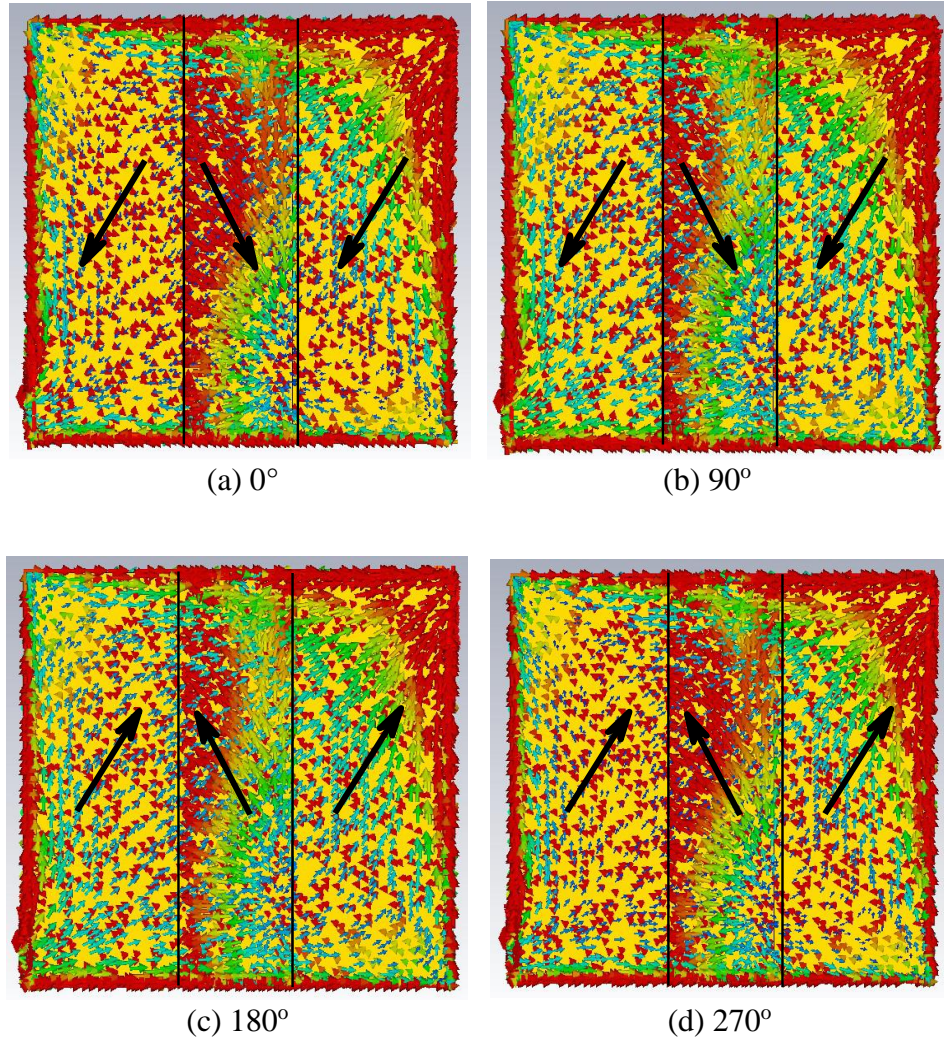
Figure 6.5. Surface currents on the top and bottom patches at the source phases of (a) 0° (b) 90° (c) 180° and (d) 270°.

6.2.3   Equivalent Circuit Model

Figure 6.6(a) illustrates the tag antenna's equivalent circuit. It is set up here for the purpose of analysing the antenna's characteristics. The top and bottom patches are equal in dimension, and both are joined to the ground by a shorting stub, where each patch can be described by the lumped components R_a, L_a, and C_a arranged in parallel. The total patch impedance is $Z_a = R_a || L_a || C_a$. The top and bottom patch inductances L_a can be obtained using $L_a = 200i_1\{\ln [2i_1/(0.5(w + w) + C_t)] + 0.50049 + [(0.5(w + w) + C_t)/3i_1]\}$ (nH) (Greenhouse,

1974). The capacitance can be calculated using the equation $C_a = \varepsilon_r\varepsilon_o A_e/h_1$ (pF) (Yang et al., 2011), here, h_1 and ε_r are the foam substrate's thickness and relative permittivity, respectively. Taking electric fields into account, the space between the patches and the ground patch is also seen as parallel capacitive plates, where $A_e = i_1(w + w)/2$ is the patch's effective area. A macro model method (D. Kim and J. Yeo, 2010) can be used to determine the resistance R_a. Shorting stubs are modeled here by a serial connection of a resistance R_s and an inductance L_s. The shorting stubs have a resistance of $R_s = 2[(\rho h)/(i_3 \times h_1)][K_c/(1 - e^{-x})]$ (Ng et al., 2018), in which the copper's resistivity is $\rho = 1.72 \times 10^{-8}$ Ωm, The current crowding factor is $K_c = 1.94$, and $x = [2(1 + h_1/i_3)]$ (δ/h_1), where $\delta = 2.18 \times 10^{-6}$ m is the copper skin depth. $L_s = 400h$ {ln $[2h(C_t + i_3)] + 0.50049 + [(C_t + i_3)/3h]$} can be used to calculate the inductance of the shorting stub. The overlapped region of the top and bottom patches has introduced an additional capacitance and it can be calculated by using $C_{ol} = \varepsilon_r\varepsilon_o A/d$, where A is the overlapped area and d is the separation distance. A large capacitance has been resulted as d is as thin as the polyimide thickness. As can be seen from the equivalent circuit in Figure 6.6(a), the two *RLC* resonators are serially connected to C_{ol}. Since C_{ol} is serially cascaded to the two C_a, forming C_a - C_{ol} - C_a virtually, as can be observed in Figure 6.6(b), the electric fields in the overlapped region must be in the opposite direction as those in the non-overlapped regions, resulting in opposite surface currents as well. All the calculated element values are shown in the figure caption. The proposed tag antenna's total input impedance (Z_{in}) can then be described using equation (6.1). The equivalent circuit model helps to determine the antenna's impedance. For tag design, it is always an objective to make $Z_{in} = Z^*_{chip}$ so that

119

conjugate matching condition can be attained in between the antenna and the chip, enabling a maximum power transfer. The equivalent circuit model's input impedance is then shown in Figure 6.7 and matches well to that obtained by the simulation software. There is a slight difference between the curves since the component values are calculated by assuming uniform current distribution on the radiating patches. Regardless of the slight difference, the equivalent circuit can still be useful for impedance analysis. Since the tag antenna's port is aligned along the sidewall of the flexible foam substrate, reaching it with a differential probe for antenna impedance measurement is quite difficult. So, this section only includes the simulated antenna impedance.
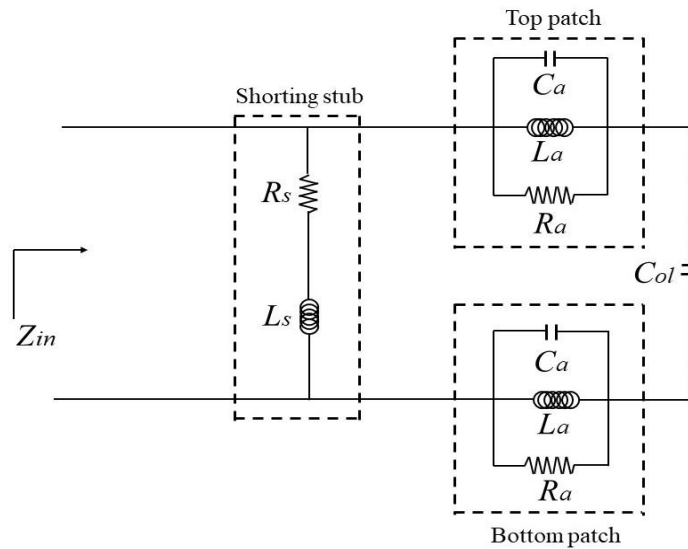
(a)
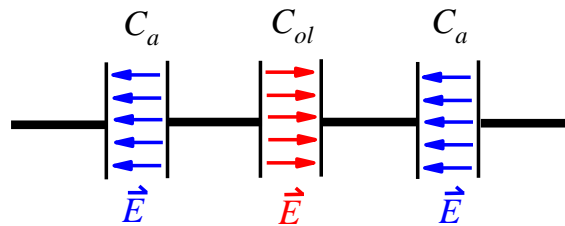
(b)

Figure 6.6. (a) Proposed tag antenna's equivalent circuit model (R_s = 5.21 mΩ, L_s = 1.58 nH, R_a = 1.84 kΩ, L_a = 8.23 nH, C_a = 1.54 pF, C_{ol} = 70.83 pF). (b) Fields in the capacitors in series.
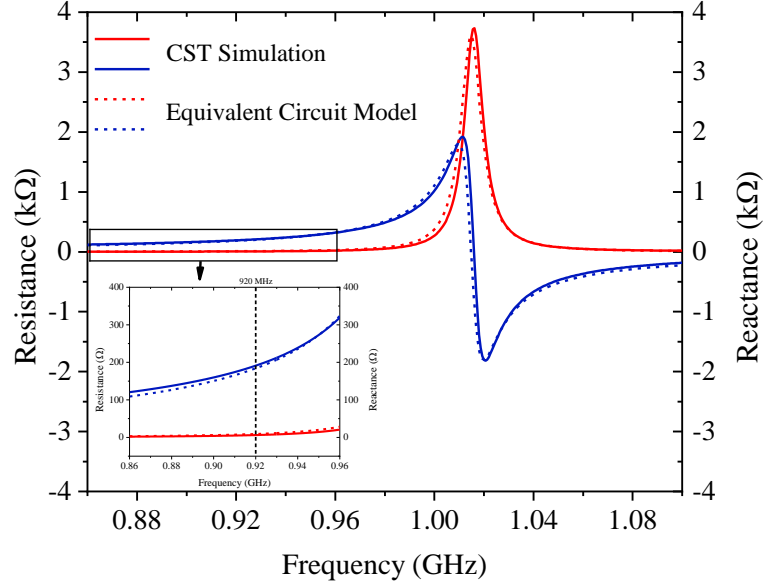
Figure 6.7. Comparing the modeled and simulated input impedances of the proposed tag antenna.

$$Z_{in} = \left(2Z_a + \frac{1}{j\omega C_{ol}}\right) \parallel Z_s \quad , \tag{6.1}$$

where

$$Z_a = \frac{j\omega R_a L_a}{R_a - \omega^2 R_a L_a C_a + j\omega L_a} \quad , \tag{6.2}$$

$$Z_s = R_s + j\omega L_s \quad . \tag{6.3}$$

6.3   Parametric Analysis

Simulations were used to investigate the impact of the key design parameters on the power transmission coefficient (τ) and input impedance. The tag is always attached to the middle of a 20 cm $\times$ 20 cm metal plate. The offset distance (i_2) of the shorting stubs is studied first. Here, i_2 is increased from 0.3 mm to 1.9 mm to perform frequency tuning. As seen in Figure 6.8(a), decreasing i_2 contributes to lowering the tag resonance frequency but keeping the τ value almost a constant. The resonance frequency of the tag is seen to be decreasing at a rate of 17.5 MHz with increasing i_2 by a stepsize of 0.4 mm.

121

As the stub's offset is reduced, the tag antenna becomes more resistive (tag resistance raises) and inductive (tag reactance raises) at the tag resonance frequency, as observed in Figure 6.8(b). Adjusting the offset location is therefore important for rough tuning the tag antenna's resonance frequency to the appropriate UHF RFID passband. The effects of the shorting stubs width (i_3) are then studied. As shown in Figure 6.9(a), raising i_3 from 4 mm to 8 mm makes the tag antenna's resonance frequency moving higher, but it retains a constant τ. When the width of both the shorting stubs is decreased from 8 mm to 4 mm, the tag's resistance and reactance stay almost unchanged, even though the corresponding resonance frequency has dropped down.

(a)
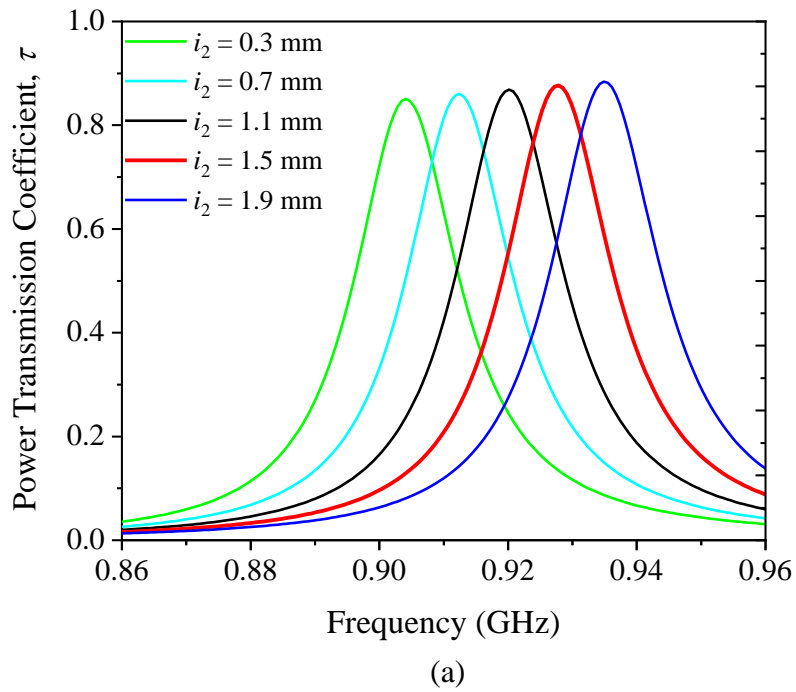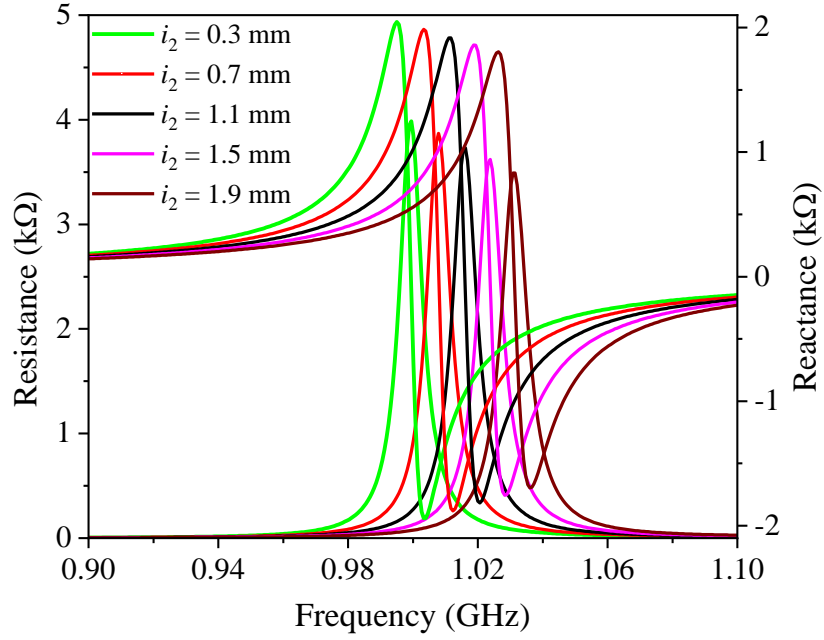
Figure 6.8. Analysing the (a) power transmission coefficient and (b) impedance by varying the offset distance (i_2) of the shorting stubs.
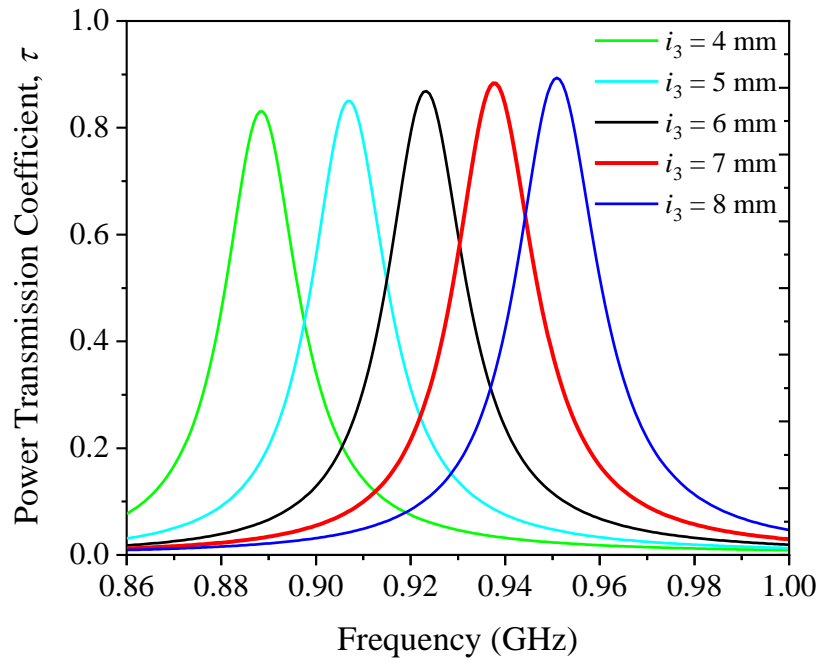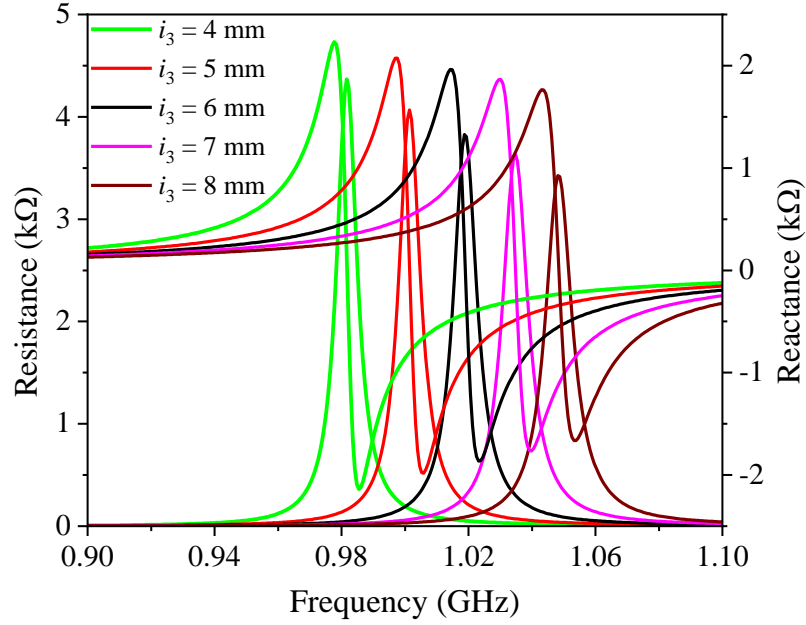
(b)

Figure 6.9. Analysing the (a) power transmission coefficient and (b) impedance by changing the width of the shorting stubs i_3.

6.4   Measurement Setup

The performance of the tag inside an anechoic cabin was tested using the Voyantic Tagformance Measurement System. With reference to Figure 6.10(a), the tag is attached to the center of a 200 mm × 200 mm aluminium plate, which is kept in place by a Styrofoam with a relative permittivity of 1, in all measurements. The tag is always placed at the center of the cabin. The fabricated prototype and the measurement setup are depicted in Figures 6.10(a) and 6.10(b), respectively. The proposed tag is tested using an LP antenna reader (8 dBi Gain). The distance between the reader antenna and the tag being measured along the z axis is kept constant at 52 cm. The realized gain is defined as $G_r = P_{ic} / (L_T \times P_{tx})$, where L_T is the total cable and free space losses, P_{ic} is the read sensitivity of the microchip (−20.85 dBm), and P_{tx} is the

reader's threshold power level at a specific frequency. Figure 6.11(a) depicts our tag antenna's simulated and measured realized gains. The maximum realized gain at 917 MHz is measured to be –1.12 dBi, with reasonable agreement observed between the simulation and measurement results. Figure 6.11(b) shows the proposed tag antenna's measured realized gains at different locations in the range $30^o \leq \theta \leq 150^o$. The maximum realized gain at $\theta = 30^o$ is measured to be 5.7 dBi.

(a)   (b)
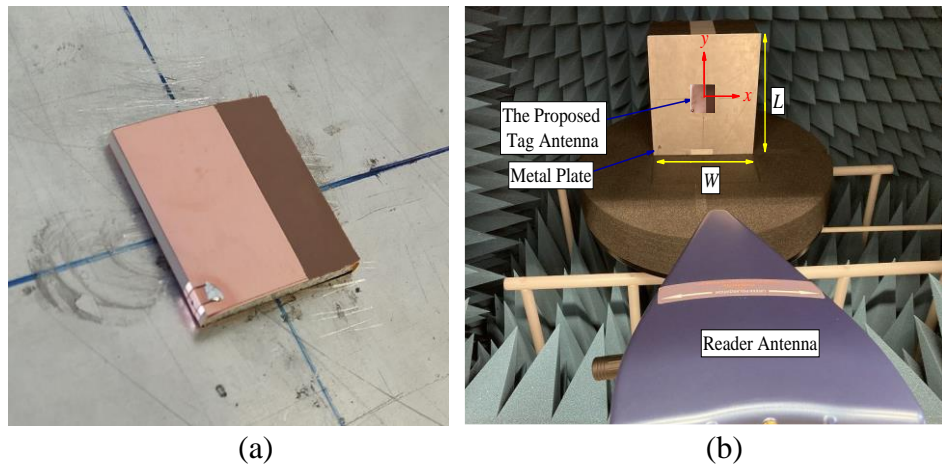
Figure 6.10. (a) Aluminium plate with the prototype attached at the middle. (b) The measurement setup in the anechoic cabin.

(a)   (b)
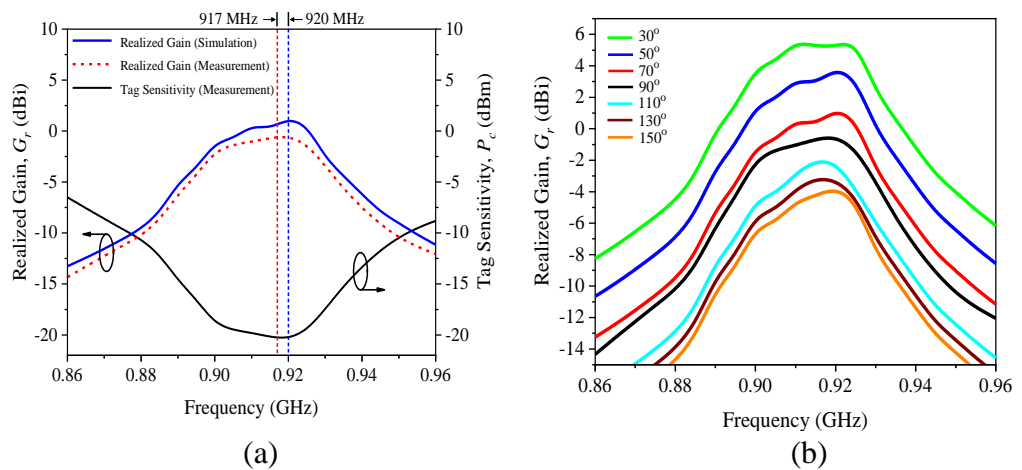
Figure 6.11. (a) Simulated and measured realized gains, as well as the measured tag sensitivity, when the tag is placed on a 20 cm × 20 cm aluminium plate and (b) Measured realized gains at different locations.

125

6.5   Experimental Results and Discussion

The simulated and measured realized gains (G_r) of the polarization-insensitive tag antenna are studied in the *xz*, *yz*, and *xy* planes, as shown in the polar plots in Figures. 6.12(a)-(c), depicting the realized gains for the fields E_θ, E_ϕ, and $E_{total} = |\vec{E}_{total}| = \sqrt{|\vec{E}_\theta|^2 + |\vec{E}_\phi|^2}$. The simulated and measured results are in good agreement. The E_ϕ component diminishes when it approaches $\theta = 90^\circ$ as tangential electric field does not exist on metal. Here, only the E_θ component, which is normal to the metal surface, can exist. For all cases, the field maximizes at around $\theta = 40^\circ$ due to the presence of the two shorting stubs in the diagonal corners, where the surface currents are the strongest. Since the tag is mounted on the metal plate, the region of interest is the upper hemispherical space ($\theta \leq 90^\circ$). As seen in Figures 6.12(a) and (b), the realized gains are reasonably good for both the E_θ and E_ϕ components in the upper hemisphere, signifying that the tag can be read in both the θ and ϕ directions above the metal plate. The G_r for E_{total} is larger than 0 dBi for ($\theta \leq 50^\circ$), and it shows polarization insensitivity feature in the *xz* and *yz* planes, with a nonuniformity factor of less than 4 dB in the entire region ($\theta \leq 90^\circ$). As can be seen from Figure 6.12(c), the field pattern is nearly uniform in the *xy* plane ($\theta = 90^\circ$), where the difference between the maximum and minimum points is less than 2 dB. In this plane, the maximum realized gain is achievable in the angular range of 195° - 260° and it is slightly skewed as stronger fields are generated in the directions of 45° and 225°, where stronger currents are induced around

the shorting stubs. To have a better view on the read performances when the tag is placed on metal, the corresponding measured and simulated read distances (R) have been added as Figure 6.13. The tag can be read reasonably well in the upper-half space ($\theta < 90^\circ$) in both the azimuthal and elevation directions. In conclusion, the suggested tag antenna can be read in all directions at all points above the metal plate.
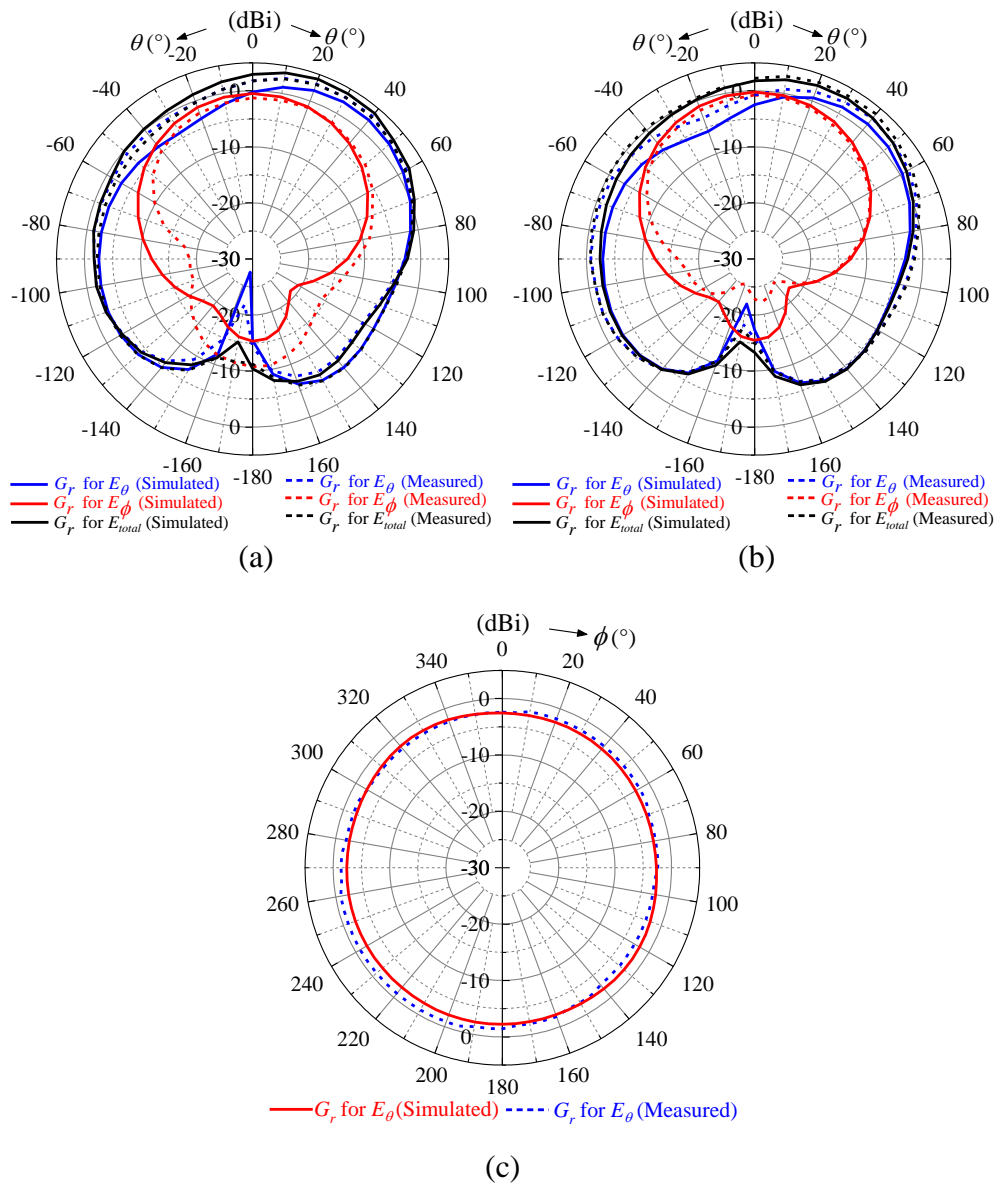
Figure 6.12. Simulated and measured realized gains in the (a) *xz* plane (b) *yz* plane and (c) *xy* plane.
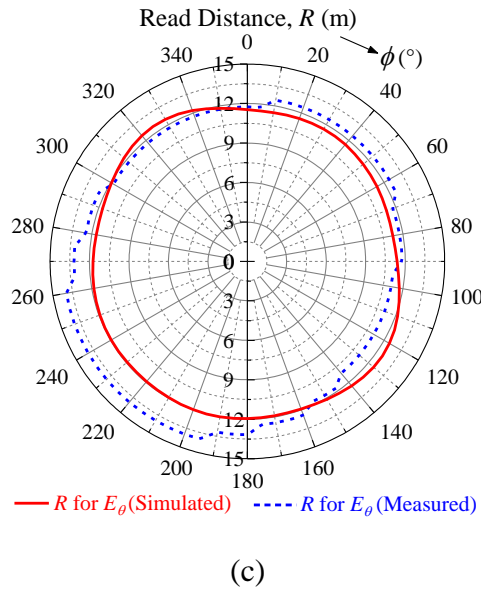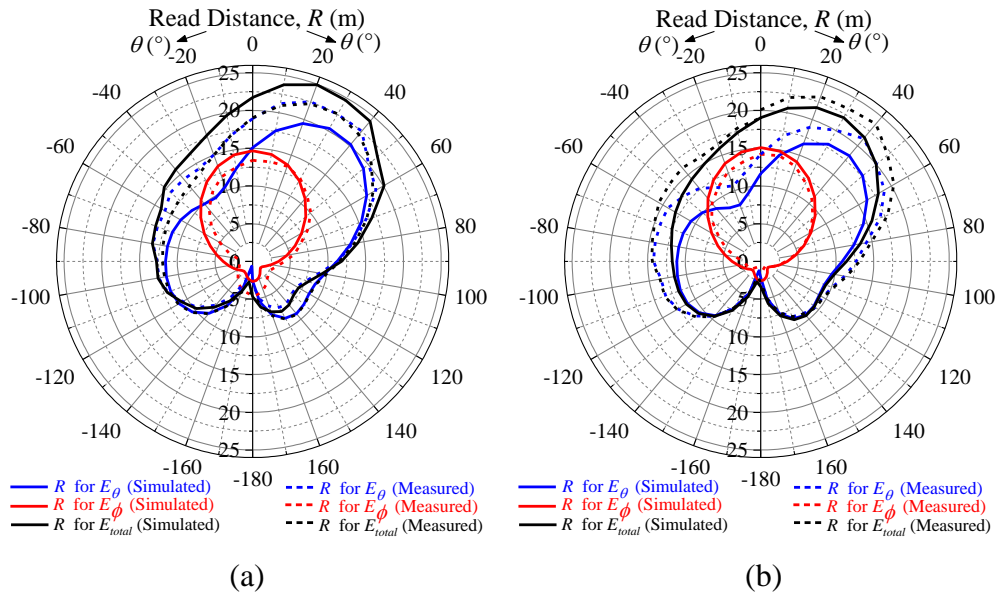
Figure 6.13. Simulated and measured read distances in the (a) *xz* plane (b) *yz* plane and (c) *xy* plane.

The tag antenna is suitable for use on metallic surfaces. It is now tested on aluminium plates that are cut into different dimensions ($W \times L$), all of which have a thickness of ~5 mm. The prototype was always attached to the middle of the plate during the tests. For comparison, maximum read distances were measured in the boresight ($\theta = 0°$) direction. When W is kept at 20 cm, the read range can be maintained ~13 m by lowering L from 20 cm to 12 cm

progressively, as shown in Figure 6.14(a). The plate width W is then varied while the plate length L remains constant at 20 cm, and the results are depicted in Figure 6.14(b). It was observed from simulations that the read ranges fluctuate within a very narrow range of 14.71-14.74 m when the plate dimension is varied. We have concluded that the discrepancy can be caused by experimental tolerances such as the placement accuracy and others. When the plate width is reduced, the read distance drops. Worth to mention here is that the tag resonance frequency is stable for all cases.
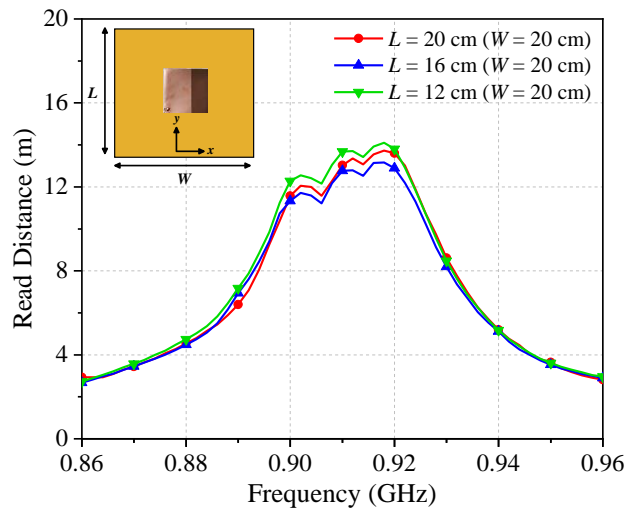
(a)
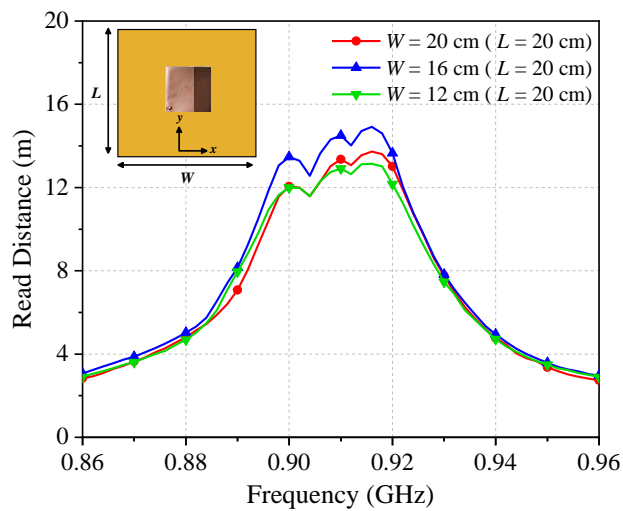
(b)

Figure 6.14. The tag antenna's measured read distances on a metal plate by varying the (a) length of plate L and (b) width of plate W.

The tag was also tested using a couple of metallic household items for verifying its practical implementation. With reference to Figure 6.15, the tag was placed on the body and the base of the household items to acquire their read ranges in the boresight ($\theta = 0°$) direction. The measurement curves are shown in Figure 6.16. When the tag is attached to the household items, a far read range of 10 m - 13 m is achievable. The read distance does decrease with decreasing the surface. Even though the metallic containers vary in material and size, the tag resonance frequency remains consistent. The tag resonance frequency can be controlled within a small range of 917 MHz - 919 MHz, while the reading performance remains stable. It has been proven that our tag antenna is less sensitive to the backing metallic object, which can become a useful feature for practical applications.
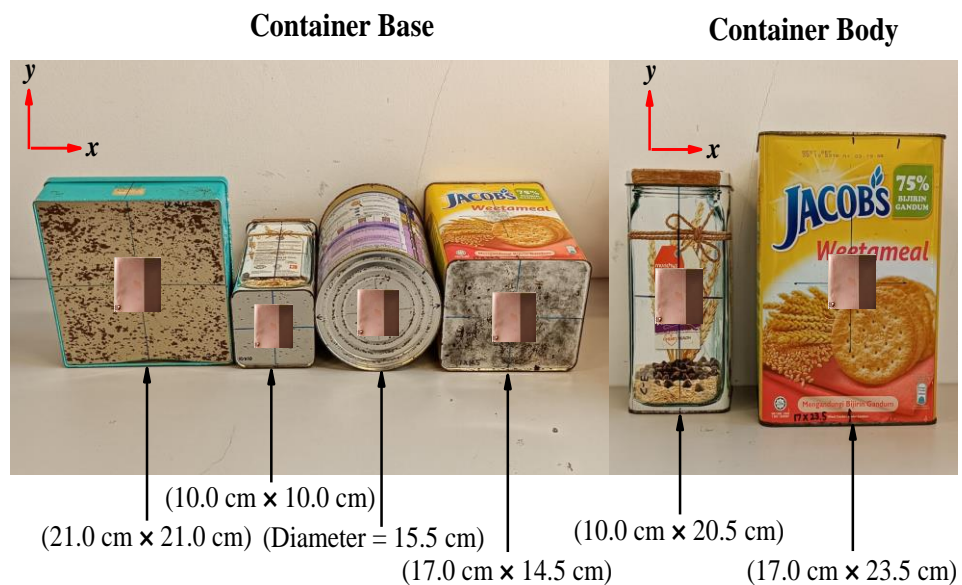
Figure 6.15. The tag is tested on different metallic household items.
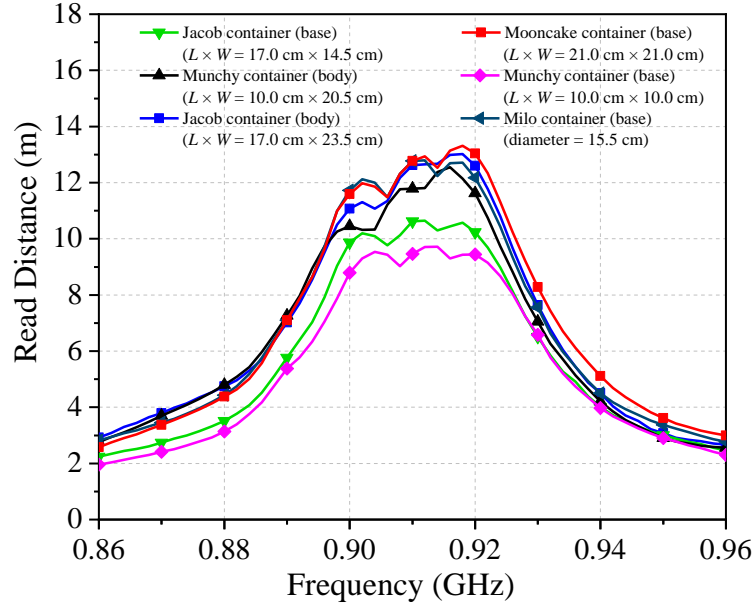
Figure 6.16.   Read distances for the different metallic household items.

Comparison is made between the proposed tag antenna with other on-/in-metal tag antennas, as tabulated in Table 6.2. Two dual-planar inverted-F antennas are placed in cross constellation for designing a polarization-diversity antenna that can be used for metal-mountable applications (Yang and Son, 2016). But the tag size is ~60% larger than ours, and it requires four lumped capacitors and 12 vias to achieve a read distance of 10.2 meters. The orientation-insensitive tag antenna in (Bong et al., 2018) consists of two orthogonally placed dipolar patches that can be detected in all directions at any points above the backing metal. However, the tag's read range is very low, and it has a poor impedance matching with a microchip. With the application of the characteristic mode, a dual-polarized UHF RFID tag antenna with polarization diversity feature has been proposed in (Althobaiti et al., 2020). However, the tag footprint is larger, while its read range is smaller than ours. Moreover, the tag is not flexible due to the use of FR4 rigid substrate. To achieve polarization diversity, the tag structure in (Ng et al., 2020) consists of

two folded crossed dipoles that are orthogonally displaced, where the read range is 50% lower than ours. It should be mentioned that all the tags require the use of more than one radiator to enable accessibility in all polarizations. In contrast, our newly proposed tag here only needs a single radiator, and it can achieve good impedance matching and far read range at the same time. Our proposed tag is also compared with other compact metal-mountable tags (Zhang and Long, 2014 and Nguyen et al., 2021), although they are not polarization insensitive. A compact linearly polarized double-layered tag antenna (Zhang and Long, 2014) is made by combining a dual-element planar inverted-F antenna (PIFA) fed by a capacitive network embedded inside the middle layer. Nevertheless, the fabrication process is extremely time-consuming due to the incorporation of four interlayer metallic vias, and the read range is much shorter as well. For metal-mountable applications, a compact C-shaped patch has been proposed in (Nguyen et al., 2021); however, the antenna structure is made on a rigid substrate, and it is not flexible. The achievable read range is also not so far. Although the metal-mountable tags in (Niew et al., 2020; Jaakkola, 2016, and Thirappa et al., 2019) are compact, their achievable read ranges are less than 7 m with single-polarization readability. The in-metal tag proposed by (Sun et al., 2016) is too large, while the read distance for that in (Michel et al., 2019) is too short. On the other hand, our newly presented tag antenna has a low profile and slight flexibility, and it can be applied on metal for achieving a far distance. Most importantly, it can be tactfully designed using a single radiator to achieve polarization insensitivity feature above the backing metal.

Table 6.2. Comparison with other metal tags (All are normalized with a reader power of 4 W EIRP).

Ref.	Tag Dimension (mm)	Application	Flexibility (Substrate)	Polarization Insensitivity	Read Distance (m)
This work	$40 \times 40 \times 3.38$ ($0.122\lambda \times 0.122\lambda \times 0.010\lambda$)	On-metal	Yes (Foam)	Yes	15
(Niew et al., 2020)	$20 \times 18 \times 1.7$ ($0.061\lambda \times 0.055\lambda \times 0.005\lambda$)	On-metal	Yes (Foam)	No	6.62
(Jaakkola, 2016)	$18 \times 4 \times 2$ ($0.052\lambda \times 0.011\lambda \times 0.005\lambda$)	On-metal	No (Ceramic Laminate)	No	3.32
(Yang and Son, 2016)	$64 \times 64 \times 2$ ($0.196\lambda \times 0.196\lambda \times 0.006\lambda$)	On-metal	No (FR4)	Yes	10.2
(Bong et al., 2018)	$30 \times 30 \times 1.6$ ($0.092\lambda \times 0.092\lambda \times 0.005\lambda$)	On-metal	Yes (Foam)	Yes	3.5
(Althobaiti et al., 2020)	$50 \times 50 \times 2$ ($0.153\lambda \times 0.153\lambda \times 0.006\lambda$)	On-metal	No (FR4)	Yes	8.5
(Ng et al., 2020)	$40 \times 40 \times 1.6$ ($0.121\lambda \times 0.121\lambda \times 0.004\lambda$)	On-metal	Yes (Foam)	Yes	7.7
(Zhang and Long, 2014)	$26 \times 14 \times 2.4$ ($0.081\lambda \times 0.043\lambda \times 0.007\lambda$)	On-metal	No (FR4)	No	5.5
(Nguyen et al., 2021)	$30 \times 30 \times 3$ ($0.092\lambda \times 0.092\lambda \times 0.009\lambda$)	On-metal	No (FR4)	No	6.4
(Sun et al., 2016)	$117 \times 80 \times 3.18$ ($0.354\lambda \times 0.242\lambda \times 0.009\lambda$)	In-metal	No (Rogers RT5880)	No	23
(Michel et al., 2019)	$23 \times 23 \times 1$ ($0.071\lambda \times 0.071\lambda \times 0.003\lambda$)	In-metal	No (Alumina)	No	0.6
(Thirappa et al., 2019)	$23 \times 7.5 \times 3.2$ ($0.070\lambda \times 0.023\lambda \times 0.010\lambda$)	On-metal	Yes (Foam)	No	5

6.6   Summary

In this project, I have proposed a novel folded patch structure, which consists of two flaps of tightly overlapped patches on a single-layer resonator, for designing a polarization-insensitive tag antenna that can be used on metal. Here, the pair of orthogonal currents are generated in a unique way with the use of only one radiator. This approach is new as it does not require the use of several radiating components for designing a polarization-insensitive tag antenna. The tag antenna design here is rather simple, and the radiator is only composed by two flaps of patches, where they are partially overlapped for generating a pair of orthogonal currents. Such feature makes the tag readable from almost all directions at all points above the metal surface. When tested on metal, the proposed tag was able to attain a maximum reading distance of ~15 m. The tag resonance frequency is also quite constant.

CHAPTER 7

CONCLUSIONS

7.1   Summary

In this research thesis, four compact single-layered planar antennas are presented for flexible UHF RFID tags for on-metal applications. These tag antennas are electrically small (the largest dimension is just 50 mm), have a low profile (less than 3.3 mm), and can be detected from a distance of at least 9 meters on metal. Furthermore, since all the tag antennas are constructed using the flexible foam and PET materials, they allow conformal attachment on slightly curved surfaces. In addition, these tag antennas are platform-insensitive because the backing metallic object do not affect their resonance frequencies.

The first two are compact UHF tag antennas, which consist of a square ring loaded with two distributed inductors, and they are proposed for on-metal applications. Miniaturization of the antenna footprint is realized by incorporating two distributed inductors. Due to the distributed inductor's high-inductive nature, the ring resonator's antenna resistance can be significantly enhanced to achieve conjugate impedance match with the microchip. These tag antennas can attain a maximum read distance of 9 m, when being placed on metal at an EIRP power of 4 W.

The second antenna, a single-layer patch antenna constructed using two complementarily placed C-shaped patches, has been proposed for designing a metal-mountable tag with a wide range of frequency tuning capabilities. The two patches are closely coupled to generate sufficient antenna reactance, which is, in turn, employed as a tuning mechanism. With only the employment of this tuning mechanism, the tag's resonance frequency can be successfully tuned over a broad range covering 920 MHz - 1.18 GHz without using any other external lumped components, shorting stubs, or vias. Furthermore, this tag antenna can attain a maximum read distance of 9 m, when being placed on metal at an EIRP power of 3.28 W.

The third antenna is a new serpentine patch ZOR antenna. It is used to design an anti-metal tag with omnidirectional radiation characteristics on metallic surfaces. The zeroth-order resonance (ZOR) structure here comprises two closely stacked serpentine patches for providing the parasitic elements required for supporting the zeroth-order resonance. Also, the geometrical parameters of the serpentine patches can be used for effectively tuning the tag resonance frequency. The proposed tag contains no complex structures like metallic vias, small notches, and narrow slots. It can be easily made through a simple etching process. Due to the successful excitation of the ZOR mode, our tag antenna can generate a reasonably good omnidirectional radiation pattern. When being tested with an EIRP of 4 W, due to good impedance matching, an excellent power transmission of ~99% is achievable. When tested on metal, the proposed tag can produce an excellent omnidirectional radiation pattern,

with a maximum reading distance of around 10 m at 915 MHz. It has a uniform spatial coverage (> 8 m) in the entire azimuth plane.

Finally, the fourth antenna, a polarization-insensitive planar patch antenna with a large embedded serial capacitance, is proposed for constructing a metal-mountable tag. The proposed antenna structure itself contains two flaps of patches, which are very closely overlapped, for generating a large capacitive reactance for reducing the resonance frequency of the tag. It has been found that the surface currents in the overlapped region are in the reverse direction as the large capacitance is virtually placed in series. This feature has been tactfully employed for producing a pair of orthogonal currents for designing the polarization-insensitive tag antenna. As a result, it can generate orthogonal fields uniquely, making it readable from almost all directions at all points above the metal surface. This tag antenna can attain a maximum read distance of 15 m when placed on metal at an EIRP power of 4 W.

Our design has utilized Ucode 8, a commercial chip from the NXP Ucode series. However, it is worth noting that we also have the flexibility to incorporate the Ucode 9 chip, as both chips share the same impedance value of $13 - j191$ Ω. Furthermore, we can also employ other commercial UHF RFID chips such as the Impinj Monza series, Alien Technology Higgs series, SensThys SensRF series, and Zebra Technologies Zebra series. However, it's important to note that we would need to make appropriate parametric adjustments to ensure compatibility with the desired impedance to achieve optimal performance.

For impedance analysis, the transmission line models, or equivalent circuit models are theoretically derived. Methods for designing directional and omnidirectional antennas are presented. The configurations of the first two tag antennas are designed to generate directional radiation patterns, with the highest radiation in the broadside direction. In contrast, the last two tag antennas are designed to radiate omnidirectionally in the azimuth plane, which may be beneficial for some on-metal applications. Taking all of this into account, all of the project's objectives have been met, and the disclosed information has clearly shown the salient features of the proposed tag antennas.

7.2   Future Research

Indeed, microstrip technology has been a driving force behind the rapid advancements of RFID. Its application for designing compact and efficient RFID elements, such as antennas and tags, has enabled a significant progress. Despite the considerable progress, the search for new and innovative structures and materials remains a focal point of interest within the research community. Continuously exploring novel elements can lead to breakthroughs in the RFID's performances, ranges, sensitivities, and overall functionalities. As the technology continues to evolve, it is anticipated that microstrip-based approaches will continue to play a vital role in shaping the future of RFID. The development of cutting-edge microstrip structures and materials will likely open up new possibilities and applications, enhancing the RFID's capabilities and expanding its uses in various industries. The research

community's commitment to exploring these possibilities indicates that RFID will remain a vibrant and exciting field in the years to come.

In future, works on enhancing the tags' sensitivities and read ranges, allowing them to be used for more efficient and accurate data collection, even in some challenging environments, are required to make the tags more versatile, enabling them to be embedded in various products and materials without compromising their performances. In the future, there will be a need on the development of eco-friendly and sustainable materials and manufacturing techniques for tag design to minimize the environmental impact.

REFERENCES

Acua, J.E., Rodriguez, J.L. and Obelleiro, F., 2001. Design of meander line inductors on printed circuit boards. *International Journal of RF and Microwave Computer-Aided Engineering*, 11(4), pp. 219-230.

Amendola, S., Milici, S. and Marrocco, G., 2015. Performance of epidermal RFID dual-loop tag and on-skin retuning. *IEEE Transactions on Antennas and Propagation*, 63(8), pp. 3672-3680.

Althobaiti, T., Sharif, A., Ouyang, J., Ramzan, N. and Abbasi, Q.H., 2020. Planar pyramid shaped UHF RFID tag antenna with polarisation diversity for IoT applications using characteristics mode analysis. *IEEE Access*, 8, pp. 103684-103696.

Babar, A.A., Bjorninen, T., Bhagavati, V.A., Sydanheimo, L., Kallio, P. and Ukkonen, L., 2012. Small and flexible metal mountable passive UHF RFID tag on high-dielectric polymer-ceramic composite substrate. *IEEE Antennas and Wireless Propagation Letters*, 11, pp. 1319-1322.

Balanis, C.A., 2005. Microstrip antennas. In: *Antenna Theory: Analysis and Design*. Hoboken, NJ: John Wiley, pp. 816-842.

Borchardt, J.J., 2020. Loop antennas for use on/off ground planes. *IEEE Access*, 8, pp. 138763-138770.

Bong, F.L., Lim, E.H. and Lo, F.L., 2017. Flexible folded-patch antenna with serrated edges for metal-mountable UHF RFID tag. *IEEE Transactions on Antennas and Propagation*, 65(2), pp. 873-877.

Bong, F.L., Lim, E.H. and Lo, F.L., 2018. Compact orientation insensitive dipolar patch for metal-mountable UHF RFID tag design. *IEEE Transactions on Antennas and Propagation*, 66(4), pp.1788–1795.

Bergman, W.J. and Schultz, F.V., 1955. The circular traveling-wave antenna. 1958 *IRE International Convention Record,* pp. 40-50.

Chiang, S.M., Lim, E.H., Chee, P.S., Lee, Y.H. and Bong, F.L., 2022. Dipolar tag antenna with a top-loading inductive channel with broad range frequency tuning capability. *IEEE Transactions on Antennas and Propagation*, 70(3), pp. 1653-1662.

Chen, H.D. and Tsao, Y.H., 2010a. Low-profile meandered patch antennas for RFID tags mountable on metallic objects. *IEEE Antennas and Wireless Propagation Letters*, 9, pp. 118-121.

Chen, H.M., Yeh, S.A., Lin, Y.F., Pan, S.C. and Chang, S.W., 2012. High chip reactance matching for ultra-high-frequency radio frequency identification tag antenna design. *IET Microwaves, Antennas & Propagation*, 6(5), pp. 577-582.

Chen, H.D., Sim, C.Y.D., Tsai, C.H. and Kuo, C., 2016. Compact circularly polarized meandered-loop antenna for UHF-band RFID tag. *IEEE Antennas and Wireless Propagation Letters*, 15, pp. 1602-1605.

Cho, C., Choo, H. and Park, I., 2008. Design of planar RFID tag antenna for metallic objects. *Electronics Letters*, 44(3), p. 175-177.

Colella, R., Catarinucci, L., Coppola, P. and Tarricone, L., 2016. Measurement platform for electromagnetic characterization and performance evaluation of UHF RFID tags. *IEEE Transactions on Instrumentation and Measurement*, 65(4), pp. 905-914.

Dispersion Diagram: CST Microwave Studio [Online]. https://dokumen.tips/reader/f/dispersion-diagram-cst-microwave-studio-irib-cstmwssmrrazavizadehieeeorg [Accessed: 1 March 2023].

Erman, F., Koziel, S., Hanafi, E., Soboh, R. and Szczepanski, S., 2022. Miniaturized metal-mountable U-shaped inductive-coupling-fed UHF RFID tag antenna with defected microstrip surface. *IEEE Access*, 10, pp. 47301-47308.

Finkenzeller, K. and Muller, D., 2012. Automatic identification systems. In: *RFID handbook: fundamentals and applications in contactless smart cards, radio frequency identification and near-field communication*, Chichester: Wiley, pp. 2-6.

Gao, B. and Yuen, M.M.F., 2011. Passive UHF RFID packaging with electromagnetic band gap (EBG) material for metallic objects tracking. *IEEE Transactions on Components, Packaging and Manufacturing Technology*, 1(8), pp. 1140-1146.

Genovesi, S. and Monorchio, A., 2010. Low-profile three-arm folded dipole antenna for UHF band RFID tags mountable on metallic objects. *IEEE Antennas and Wireless Propagation Letters*, 9, pp. 1225-1228.

Ghiotto, A., Cantalice, S.F., Vuong, T.P., Pouzin, A., Fontgalland, G. and Tedjini, S., 2008. Miniaturized patch antenna for the radio frequency identification of metallic objects. *2008 IEEE MTT-S International Microwave Symposium Digest*, 15-20 June 2008 Atlanta, GA, USA. pp. 583-586.

Greenhouse, H.M., 1974. Design of planar rectangular microelectronic inductors. *IEEE Transactions on Parts, Hybrids, and Packaging*, 10(2), pp. 101-109.

Hansen, R.C., 2006. Electrically small antennas. In: *Electrically Small, Superdirective, Superconducting Antennas*. Hoboken, NJ: Wiley, pp. 54-62.

Hassan, T.C., Yi, H., Xu, Z. and Yang, L., 2009. An empirical equation for predicting the resonance frequency of planar inverted-F antennas. *IEEE Antennas and Wireless Propagation Letters*, 8, pp. 856-860.

Hunt, V.D., Puglia, A. and Puglia, M., 2007. RFID - *a guide to radio frequency identification*. Hoboken, NJ: Wiley.

Hsieh, H.L. and Chang, K., 2005. Encyclopedia of RF and Microwave Engineering: Ring Resonators and Circuits, Hoboken, NJ, USA: Wiley.

Inserra, D. and Wen, G., 2021. Low profile metal tolerant UHF RFID tag with lumped elements for post-manufacturing frequency tuning. *IEEE Transactions on Antennas and Propagation*, 69(11), pp. 7953-7958.

Jaakkola, K., 2016. Small on-metal UHF RFID transponder with long read range. *IEEE Transactions on Antennas and Propagation*, 64(11), pp. 4859-4867.

Kim, D. and Yeo, J., 2008. Low-profile RFID tag antenna using compact AMC substrate for metallic objects. *IEEE Antennas and Wireless Propagation Letters*, 7, pp. 718-720.

Kim, D. and Yeo, J., 2010. A passive RFID tag antenna installed in a recessed cavity in a metallic platform. *IEEE Transactions on Antennas and Propagation*, 58(12), pp. 3814-3820.

Koo, T.W., Kim, D., Ryu, J.I., Seo, H.M., Yook, J.G. and Kim, J.C., 2011. Design of a label-typed UHF RFID tag antenna for metallic objects. *IEEE Antennas and Wireless Propagation Letters*, 10, pp. 1010-1014.

Lai, A., Leong, K.M.K.H. and Itoh, T., 2007. Infinite wavelength resonance antennas with monopolar radiation pattern based on periodic structures. *IEEE Transactions on Antennas and Propagation*, 55(3), pp. 868-876.

Li. Z., Zhu. Y., Yang. H., Peng. G. and Liu. X., 2020. A dual-band omnidirectional circular polarized antenna using composite right/left-handed transmission line with rectangular slits for unmanned aerial vehicle applications. *IEEE Access*, (8), pp. 100586-100595.

Lin, Y.F., Chang, M.J., Chen, H.M. and Lai, B.Y., 2016. Gain enhancement of ground radiation antenna for RFID tag mounted on metallic plane. *IEEE Transactions on Antennas and Propagation*, 64(4), pp.1193–1200

Lee, S.R., Lim, E.H. and Rahim, S.K.A., 2022. Small wideband antenna for on-metal UHF RFID tag design. *IEEE Journal of Radio Frequency Identification*, 6, pp. 121-127.

Lee, S.R., Ng, W.H., Lim, E.H., Bong, F.L. and Chung, B.K., 2020. Compact magnetic loop antenna for omnidirectional on-metal UHF tag design. *IEEE Transactions on Antennas and Propagation*, 68(2), pp. 765-772.

Lee, J.G. and Lee, J.H., 2007. Zeroth order resonance loop antenna. *IEEE Transactions on Antennas and Propagation*, 55(3), pp. 994-997.

Lee, Y.H., Lim, E.H. and Bong, F.L., 2019. Compact folded C-shaped antenna for metal-mountable UHF RFID applications. *IEEE Transactions on Antennas and Propagation*, 67(2), pp. 765-773.

Lin, K.H., Chen, S.L. and Mittra, R., 2013. A looped-bowtie RFID tag antenna design for metallic objects. *IEEE Transactions on Antennas and Propagation*, 61(2), pp. 499-505.

Liu, Q., Yu, Y.F. and He, S.L., 2013. Capacitively loaded, inductively coupled fed loop antenna with an omnidirectional radiation pattern for UHF RFID tags. *IEEE Antennas and Wireless Propagation Letters*, 12, pp. 1161-1164.

Marrocco, G., 2003. Gain-optimized self-resonance meander line antennas for RFID applications. *IEEE Antennas and Wireless Propagation Letters*, 2, pp. 302-305.

Marrocco, G., 2008. The art of UHF RFID antenna design: impedance-matching and size-reduction techniques. *IEEE Antennas and Propagation Magazine*, 50(1), pp. 66-79.

Murugesh, M., Lim, E.H., Chee, P.S., Lee, Y.H. and Bong, F.L., 2022. Compact ring antennas with high-impedance line loaded with distributed inductors for on-metal tag design. *IEEE Transactions on Antennas and Propagation*, 70(3), pp. 1740-1749.

Michel, A., Colella, R., Casula, G.A., Nepa, P., Catarinucci, L., Montisci, G., Mazzarella, G. and Manara, G., 2018. Design considerations on the placement of a wearable UHF-RFID PIFA on a compact ground plane. *IEEE Transactions on Antennas and Propagation*, 66(6), pp. 3142-3147.

Michel, A., Franchina, V., Nepa, P. and Salvatore, A., 2019. A UHF RFID tag embeddable in small metal cavities. *IEEE Transactions on Antennas and Propagation*, 67(2), pp. 1374-1379.

Mo, L.F. and Qin, C.F., 2010. Planar UHF RFID tag antenna with open stub feed for metallic objects. *IEEE Transactions on Antennas and Propagation*, 58(9), pp. 3037-3043.

Ng, W.H., Lim, E.H., Bong, F.L. and Chung, B.K., 2018. Folded patch antenna with tunable inductive slots and stubs for UHF tag design. *IEEE Transactions on Antennas and Propagation*, 66(6), pp. 2799-2806.

Ng, W.H., Lim, E.H., Bong, F.L. and Chung, B.K., 2020. Compact folded crossed-dipole for on-metal polarization diversity UHF tag. *IEEE Journal of Radio Frequency Identification*, 4(2), pp. 115-123.

Niew, Y.H., Lee, K.Y., Lim, E.H. and Chung, B.K., 2020. Miniature dipolar patch antenna with non-resonating ring for metal-insensitive UHF RFID tag design. *IEEE Transactions on Antennas and Propagation*, 68(3), pp. 2393-2398.

Nguyen, M.T., Lin, Y.F., Chang, C.H. and Chen, H.M., 2021. Compact shorted C-shaped patch antenna for ultrahigh frequency radio frequency identification tags mounted on a metallic plate," *International Journal of RF and Microwave Computer-Aided Engineering*. 31(6).

Okano, Y., 2006. A simple shape broadband planar antenna adaptable to RFID tag. *IEEE Transactions on Antennas and Propagation*, 54(6), pp. 1885-1888.

Ooi, S.Y., Chee, P.S., Lim, E.H., Lee, Y.H. and Bong, F.L., 2022. Stacked planar inverted-L antenna with enhanced capacitance for compact tag design. *IEEE Transactions on Antennas and Propagation,* 70(3), pp. 1740-1749.

Ooi, S.Y., Chee, P.S., Lim, E.H., Low, J.H. and Bong, F.L., 2023. A zeroth-order slot-loaded cap-shaped patch antenna with omnidirectional radiation characteristic for UHF RFID tag design. *IEEE Transactions on Antennas and Propagation*, 71(1), pp. 131-139.

Park, B.C. and Lee, J.H., 2011. Omnidirectional circularly polarized antenna utilizing zeroth-order resonance of epsilon negative transmission line. *IEEE Transactions on Antennas and Propagation*, 59(7), pp. 2717-2721.

Park, J.H., Ryu, Y.H., Lee, J.G. and Lee, J.H., 2007. Epsilon negative zeroth-order resonator antenna. *IEEE Transactions on Antennas and Propagation*, 55(12), pp. 3710-3712.

Pyo, S., Han, S.M., Baik, J.W. and Kim, Y.S., 2009. A slot-loaded composite right/left-handed transmission line for a zeroth-order resonance antenna with improved efficiency. *IEEE Transactions on Microwave Theory and Techniques*, 57(11), pp. 2775-2782.

Rao, K.V.S., Nikitin, P.V. and Lam, S.F., 2005a. Antenna design for UHF RFID tags: a review and a practical application. *IEEE Transactions on Antennas and Propagation*, 53(12), pp. 3870-3876.

Reed, S., Desclos, L., Terret, C. and Toutain, S., 2001. Patch antenna size reduction by means of inductive slots. *Microwave and Optical Technology Letters*, 29(2), pp. 79-81.

Ryoo, J., Choo, J. and Choo, H., 2012. Novel UHF RFID tag antenna for metallic foil packages. *IEEE Transactions on Antennas and Propagation*, 60(1), pp.377–379.

Sohrab, A.P., Huang, Y., Hussein, M.N. and Carter, P., 2017. A hybrid UHF RFID tag robust to host material. *IEEE Journal of Radio Frequency Identification*, 1(2), pp. 163-169.

Shahpari, M. and Thiel, D.V., 2018. Fundamental limitations for antenna radiation efficiency. *IEEE Transactions on Antennas and Propagation*, 66(8), pp. 3894-3901.

Shen, P., Zhang, W.R., Huang, L., Jin, D.Y. and Xie, H.Y., 2011. Improving the quality factor of an RF spiral inductor with non-uniform metal width and non-uniform coil spacing. *Journal of Semiconductors*, 32(6), pp. 1-5.

Shi, Y., Qi, K. and Liang, C.H., 2015. A miniaturized design of 2.45-GHz RFID tag antenna. *Microwave and Optical Technology Letters*, 57(8), pp. 1905-1908.

Sun, H., Tao, B. and Ramahi, O.M., 2016. Proximity coupled cavity backed patch antenna for long range UHF RFID tag. *IEEE Transactions on Antennas and Propagation*, 64(12), pp. 5446-5449.

Taylor, P.S. and Batchelor, J.C., 2019. Finger-worn UHF far-field RFID tag antenna. *IEEE Antennas and Wireless Propagation Letters*, 18(12), pp. 2513-2517.

Tan, C.L. and Ismail, W.B., 2012. Compact dual band tag antenna design for radio frequency identification (RFID) application. *Progress In Electromagnetics Research C*, 31, pp. 29-40.

Tagformance Measurement System Manual 5, 2012. Voyantic, Ltd., Espoo, Finland.

Thirappa, K., Lim, E.H., Bong, F.L. and Chung, B.K., 2019. Compact folded-patch with orthogonal tuning slots for on-metal tag design. *IEEE Transactions on Antennas and Propagation*, 67, pp. 5833-5841.

UCODE 8/8m Chip Data Sheet, Rev. 3.4, 2021. document SL3S1205_15, NXP, Inc., Eindhoven, Nederland.

Ukkonen, L., Sydanheimo, L. and Kivikoski, M., 2005. Effects of metallic plate size on the performance of microstrip patch-type tag antennas for passive RFID. *IEEE Antennas and Wireless Propagation Letters*, 4, pp. 410-413.

Yang, E.S. and Son, H.W., 2016. Dual-polarised metal-mountable UHF RFID tag antenna for polarisation diversity. *Electronics Letters*, 52(7), pp. 496-498.

145

Yang, P.H., Li, Y., Jiang, L.J., Chew, W.C. and Ye, T.T., 2011. Compact metallic RFID tag antennas with a loop-fed method. *IEEE Transactions on Antennas and Propagation*, 59(12), pp. 4454-4462.

Yoo, S. and Kahng, S., 2012. CRLH ZOR antenna of a circular microstrip patch capacitively coupled to a circular shorted ring. *Progress In Electromagnetics Research C*, 25, pp. 15-26.

Zamora, G., Zuffanelli, S., Paredes, F., Martin, F. and Bonache, J., 2013. Design and synthesis methodology for UHF-RFID tags based on the T-match network. *IEEE Transactions on Microwave Theory and Techniques*, 61(12), pp. 4090-4098.

Zhang, J. and Long, Y.L., 2013a. A dual-layer broadband compact UHF RFID tag antenna for platform tolerant application. *IEEE Transactions on Antennas and Propagation*, 61(9), pp. 4447-4455.

Zhang, J. and Long, Y.L., 2013b. A miniaturized via-patch loaded dual-layer RFID tag antenna for metallic object applications. *IEEE Antennas and Wireless Propagation Letters*, 12, pp. 1184-1187.

Zhang, C., Gong, J., Li, Y. and Wang, Y., 2018. Zeroth-order-mode circular microstrip antenna with patch-like radiation pattern. *IEEE Antennas and Wireless Propagation Letters*, 17(3), pp. 446-449.

Zhang, J. and Long, Y. L., 2014. A novel metal-mountable electrically small antenna for RFID tag applications with practical guidelines for the antenna design. *IEEE Transactions on Antennas and Propagation*, 62(11), pp. 5820-5829.

Zuffanelli, S., Zamora, G., Paredes, F., Aguila, P., Martin, F. and Bonache, J., 2017. On-metal UHF-RFID passive tags based on complementary split-ring resonators. *IET Microwaves, Antennas & Propagation*, 11(7), pp. 1040-1044.

PUBLICATIONS

Journals

1. **M. Murugesh**, E. H. Lim, P. S. Chee, Y. H. Lee, and F. L. Bong., 2022. Compact ring antennas with high-impedance line loaded with distributed inductors for on-metal tag design. *IEEE Transactions on Antennas and Propagation*, 70(3), pp. 1740-1749.

2. **M. Murugesh**, E. H. Lim, P. S. Chee, and F. L. Bong., 2022. Complementarily coupled C-shaped microstrip patches with wide-range frequency tuning capability for metal-applicable UHF RFID tag design. *IEEE Transactions on Antennas and Propagation*, 70(12), pp. 11548-11558.

3. **M. Murugesh**, E. H. Lim, P. S. Chee, and F. L. Bong., 2023. Polarization insensitive planar patch antenna with large embedded serial capacitance for on-metal tag design. *Springer Nature - Scientific Reports*, 13, 7702.

4. **M. Murugesh**, E. H. Lim, P. S. Chee, and F. L. Bong., 2023. Zeroth-order serpentine patch with omnidirectional characteristic for anti-metal tag antenna design. *IEEE Transactions on Antennas and Propagation*. (Under review)

5. **M. Murugesh**, E. H. Lim, P. S. Chee, and F. L. Bong., 2023. Compact dual inductive ring antenna with wide-angle radiation for on-metal UHF RFID applications. *IEEE Journal of Radio Frequency Identification*. (Under review)

6. J. H. Ng, **M. Murugesh**, E. H. Lim, and P. S. Chee., 2023. Simple truncated patch antenna with an inclined I-slit for orientation-insensitive tag design for anti-metal platform. *IEEE Transactions on Antennas and Propagation*. (Under review)

7. F. Erman, S. Koziel, E. H. Lim, L. Leifsson, E. Hanafi, and **M. Murugesh**., 2023. Low-profile compact folded dipole UHF RFID metal-mountable tag antenna with wide frequency tuning capability. *IEEE Transactions on Antennas and Propagation*. (Under review)

Conferences

1. **M. Murugesh**, Y. H. Lee, P. S. Chee, and E. H. Lim., 2020. Flexible folded-patch antenna with tapered edges for metal-mountable UHF RFID tag design. *2020 IEEE International RF and Microwave Conference (RFM)*, 14-16 December 2020, Kuala Lumpur, Malaysia.

2. **M. Murugesh**, E. H. Lim, and P. S. Chee., 2022. Orthogonal E-shaped patches with hemi-isotropic pattern for metal-mountable tag antenna. *IEEE International Conference on RFID Technology and Applications (IEEE RFID-TA 2022)*, 12-14 September 2022, Cagliari, Italy.